UNIVERSITAS OSLOENSIS
MDCCCXI

In Situ Operando SAXS and WAXS Characterization of the Anode Materials (*a-P/C* and $FeSb_2$) for Rechargeable Sodium Ion Batteries

Mauro Povia
Department of Physics, Senter for materialvitenskap og nanoteknologi
Forskningsparken, Gaustadalleen 21, 0349, Oslo

June 1, 2015

This thesis is dedicated
with love to Mee Rahn.

Acknowledgements

I wish to express my sincere thanks to prof. Sabrina Sartori, for her supervision and help during the realization of this work. I take this opportunity to express gratitude my sincere appreciation to prof. Anette Eleonora Gunnæs for the continuous encouragement and good advices. I want to express my thanks to the collaborators: Jonas Sottmann, dr. Giuseppe Portale, dr. David Zitoun and prof. Serena Margadonna. I want to thank all of the friends and group members for their help and support. I also thank my parents for the incessant encouragement, support and attention. I am also grateful to my wife who has supported me and also gave me the bravery to start this master two years ago. I thank also the trees cut down to produce the papers for this thesis.

Contents

Appendix:

List of Figures

List of Tables

Abstract

Recently sodium ion batteries have attracted great attention especially for large scale energy storage application. Nanoclusters of amorphous red phosphorus in carbon matrix *a-P/C* and orthorhombic $FeSb_2$ are promising materials for high energy conservation at room temperature due to their high theoretical specific capacity of $2500\frac{mAh}{g}$ and $540\frac{mAh}{g}$, respectively, and also due to their easy and cheap fabrication process.

A new *in-house* built cell was tested for *in situ operando* small angle X-ray scattering (SAXS) and wide angle X-ray scattering (WAXS) characterization. This newly designed cell allows, for the first time, the simultaneous acquisition of the electrochemical and X-ray structural characterization during the charge/discharge cycles. The electrochemical performance of the *in-house* built cell has compared to that of standard coin cells. The results show that the *in-house* built cell reaches the 90% of the performance of the coin cell. Furthermore, we have enabled to coordinate results of SAXS, WAXS and electrical measurements in order to trace phase transition and showed their simultaneous variation depending on time. During the characterization of the *a-P/C* and $FeSb_2$ anodes performed at the European Synchrotron Radiation Facility (ESRF), the reversible specific capacities of $1763\frac{mAh}{g}$ and $350\frac{mAh}{g}$ were achieved, respectively. Furthermore, we followed the evolution of the phase transition along the full charge/discharge cycle. In fact, according to the WAXS measurements we were able to detect the exact moment of the phase transitions from amorphous *a-P/C* to crystalline Na_3P and its reversibility. By using the the Sherrer formula we estimated an average crystalline size distribution of $25 \pm 0.1nm$ at the end of the sodiation process. The WAXS measurements gave the opportunity to follow the formation of irreversible part of the reaction process and how the active material changes its state of aggregation. For a technical problem we could not followed the structure evolution of the $FeSb_2$ during the cycle.

The *in-house* built cell would be a promising tool for further research on different amorphous and crystalline materials for both cathode and anode applications.

Chapter 1

Introduction

1.1 Rechargeable Ion Batteries

Sodium Ion Batteries (NIBs) have recently attracted increasing attention as a promising solution for energy storage. In principle they work as the more well known Lithium Ion Batteries (LIBs). Because lithium and sodium are members of the first group of the periodic table of the element, the outer electron configuration as well as their chemical behaviour are similar each other. However there are some differences, as reported in Table 1. For instance the mobility of the sodium is lower than that of lithium because sodium has a larger ionic radius and higher atomic weight than lithium.

Up to 1990 NIBs and LIBs had been studied in parallel [1]. However, in 1990 the Sony Company started selling the LIBs, based on $LiCoO_2$ as cathode and graphite as anode [2]. Such LIBs achieved so large commercial success, causing the decrease of the scientific research on NIBs.

Although the physical differences make lithium a better choice for the ion rechargeable batteries, the abundance and the availability of sodium on the Earth and in the sea water makes it much attractive [1]. In the future we will need more bat-

	Sodium	Lithium
Electron Configuration	$[Ne]s^1$	$[He]s^1$
Cation Radius	97pm	68pm
Atomic weight	$22.989 g/mol$	$6.941 g/mol$
$E_0 vs.$ SHE	-2.7V	-3.04V
Abundance	23.6x$10^3 mg/kg$	$20 mg/kg$
Price	$0.33 US\$/kg$	$6.52 US\$/kg$
Availability	Everywhere and Sea Water	A Few Location

Table 1.1: Comparison between Na and Li [1]

teries. Therefore, the opportunity, to have cheap and abundant materials for their fabrication, is causing the growing interest.

1.2 Overview of the Project: Stationary Batteries

The project is devoted to the development of *stationary batteries*, for example big rechargeable batteries connected to the grid in order to integrate the energy produced by the so called *Renewable Energy* sources (e.g. sun, wind and water). The adjective renewable is related to the fast regenerating rate of those sources in opposite to the fossil fuel which are exhaustible. However, renewable energy sources have the disadvantage to be weather and seasonal dependent, not stable even during the same day. For example photovoltaic modules are completely useless during the night and wind turbines are useless as well when there is no wind or when there is too much (when they have to be stopped to avoid mechanical damage). The nuclear power plants and fossil fuel power plants can be easily controlled and they provide a stable flux of energy for the civil and industrial activities. However, the traditional electric grid can only provide energy to the user and does not have the capability to store it.

One possible solution to deal with the fluctuation inherent to the renewable source is the concept of *Smart Grid* [3]. It consists of an electric grid connected with energy storage systems able to provide energy according to the real need hour by hour and to store the excess of the produced energy. For example a wind farm connected to batteries is shown in Figure 1.1. The excess energy can be stored in a big module of rechargeable ion batteries. The building process of these big batteries requires a huge quantity of active materials. If those batteries are made of sodium materials, the price of the modules would be largely decreased.

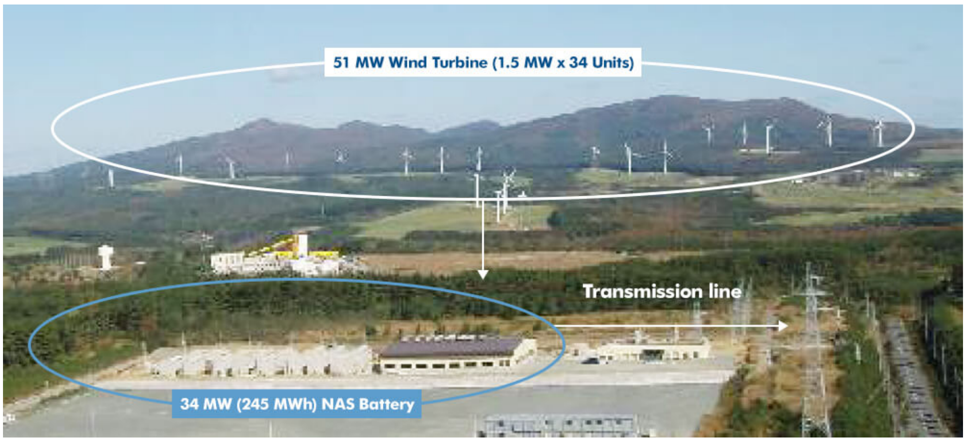

Figure 1.1: Wind farm and *NAS* batteries installed in Rokkasho (Japan) [4]

In Japan the excess of energy is stored by the *NAS* battery (Sodium-Sulphur) by NGK Company [4]. This kind of battery has the disadvantage to be operated at 300°C because both sodium and sulphur have to be in liquid state. A better knowledge about the reaction mechanism is demanded in order to achieve better performance with room temperature NIBs. Those information can be obtained by *in situ operando* measurements techniques.

1.3 Why Are *In Situ Operando* Measurements Necessary?

In situ operando measurements give the opportunity to analyse in real time every single change in the structure of the materials, during the full charge/discharged cycle of the cell. This approach is called *in situ* measurement because it allows to perform simultaneously the electrochemical characterization with other characterization techniques when the different components of the cell are still inside. The *in situ* characterization approach is different from the so called *ex situ* approach.

After a number of batteries and coin cells are used to perform charge/discharge cycle, they are broken in different point of the cycle for the characterization of the active components with scanning electron microscopy (SEM), transmission electron microscopy (TEM) and X-ray diffraction (XRD). The *ex situ* approach is based on the assumption that the characterization of the collected materials, from different coin cells, can allow to reconstruct the working mechanism of the cell. The *in situ* analysis is experimentally more complicated because it requires a specific cell, while the *ex situ* analysis requires simple standard coin cells. However, only the *in situ* analysis can provide the real picture of the reaction mechanism. Furthermore, the *ex situ* analyses have several disadvantages:

1. Several coins cell are necessary;
2. It is necessary to assume that all the coin cells are equally well made;
3. The sample preparation for the conventional characterization techniques can induce alteration in samples *e.g.*:
    (a) The sample has to be diluted or polished
    (b) When the sample is transferred to a SEM or TEM it can react with air
    (c) The sample might be electron sensitive

An example of a cell for *in situ operando* measurements was reported by G. Gershinsky *et al.* [5]. Their aim was to characterize the anode of $FeSb_2$ in a LIB with magnetic measurements. In Figure 1.2, A1 is the SQUID sample holder and A2 are the electric connection to the cell (A3). The Figure 1.2 B is a schematic representation of the cell made of a diamagnetic material not to disturb the magnetic measurement. The cell has an empty cylinder shape closed by a cap. The two electrodes are in the place of the blue and red stripes. The $FeSb_2$ anode is deposited on a copper collector, the counter electrode is made of metallic lithium. The Figure 1.2 C is the graph reporting the variation of the potential and the variation of magnetic moment *vs.* time, measured at $300K$ and a constant magnetic field of $2T$. In the paper published by C. Villevieille *et al.* [6] in 2009 the

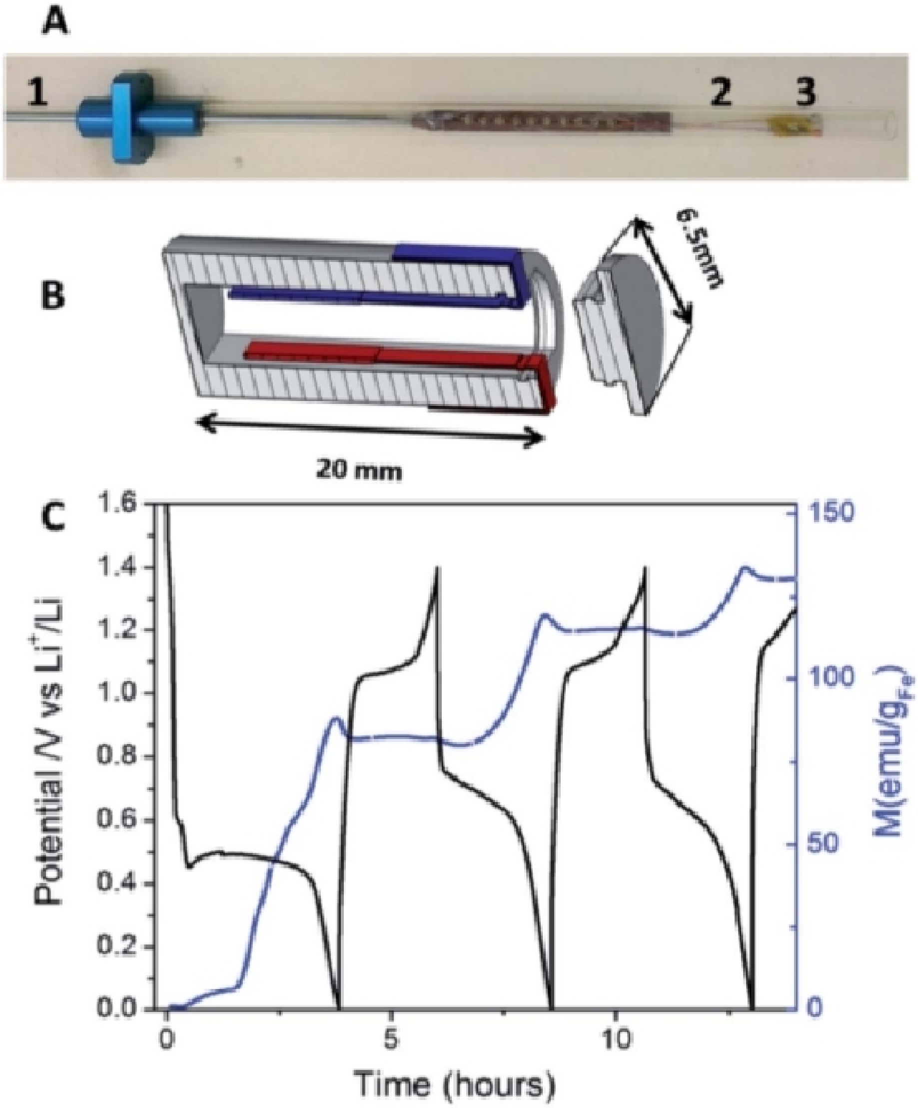

Figure 1.2: Photograph of the inset for SQUID measurement A1, the electrochemical connection A2 and *in situ* cell A3; schematic of the *in situ* cell B; electrode potential *vs.* lithium during galvanostatic cycling (blak) and corresponding magnetic moment at $300K$ (blue) C [5]

mechanism proposed for the reaction of $FeSb_2$ in a LIB was in two steps with a complete reversible reaction

$$FeSb_2 + 4Li \leftrightarrow Li_4FeSb_2 \tag{1.1}$$

$$Li_4FeSb_2 + 2Li \leftrightarrow 2Li_3Sb + Fe \tag{1.2}$$

However, the *operando* measurements performed by G. Gershinsky *et al.* showed a different result. In fact, during the lithiation there was a sharp increase of magnetic moment, whose local maximum is located after the end of the lithiation process. During the de-lithiation process, the magnetic momentum remained constant, but after three charge discharge/cycles there was a damping in the variation. This behaviour can be explained only by considering the presence of an irreversible process. In the same paper, further magnetic characterization showed the formation of a super-paramagnetic nano-particle [5]. Thanks to the *in situ operando* measurement it was possible to discover the real reaction mechanism

$$FeSb_2 + 6Li \rightarrow 2Li_3Sb + Fe \tag{1.3}$$

$$Fe + 2Li_3Sb \leftrightarrow 6Li + Sb + Fe \tag{1.4}$$

It was discovered that iron was not used any more in the conversion reaction, but it remained as useless heavy part in the batteries. Iron was used in the synthesis of the alloy only to obtain a brittle material, that can be reduced in size by ball milling. However, ball milling cannot be used to reduce the pure antimony to nanometer size because it is too ductile. If a cheap synthesis of pure antimony nano-particles is discovered, it will be possible to use it directly in battery with a theoretical capacity of $660\frac{mAh}{g}$.

1.4 Aim of the Thesis

Recently amorphous materials have attracted the interest of the scientific community for their promising performance as battery materials [7][8][9][10][11][12]. In the last decades several *in situ opernado* cells for XRD measurements were developed to analyse batteries [13][14]. However, XRD can provide information only about the crystalline materials. The aim of this thesis is to demonstrate the efficiency of a new *in-house* built cell that works in transmission mode for the acquisition of the SAXS and WAXS.

Nanoclusters of amorphous red phosphorus in carbon matrix ($a\text{-}P/C$) [12][15][16] and orthorhombic $FeSb_2$ [5] [6][17] are promising anode materials. They were selected to test the *in-house* cell because both could be good candidates for a large scale storage system due to their high specific capacity. Furthermore, the research on anode materials is urgent because in the past more materials for cathode application were successfully produced. This topic will be explained better in the section 2.1.5.

1.5 *In-House* Built Cell and the Characterization Techniques

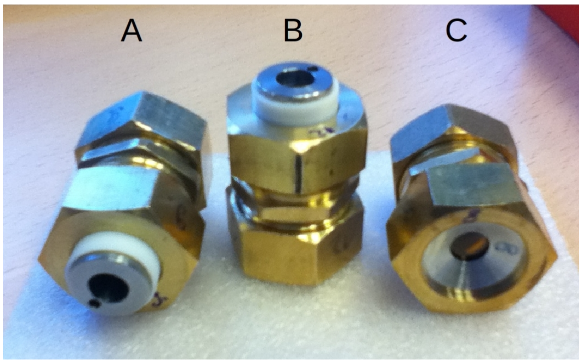

Figure 1.3: Three *in-house* built cells: A) front, B) standing and C) back views

Figure 1.3 is the picture of three *in-house* built cells from different point of view. A detailed description of the cell is reported in Chapter 3. This cell allows the simultaneous acquisition of the galvanometric measurements, SAXS and WAXS.

The galvanometric cycling is a classic measurement for batteries characterization. It is used to measure the reversible capacity and to study the variation of the difference of potential during the charge and the discharge cycle.

WAXS is the powder XRD and it is one of the most used analytical technique for the analysis of crystalline materials. The diffraction pattern provides information about the chemical composition and crystal structure in the range size from $1\AA$ to $10\AA$.

SAXS is an analytical non-destructive technique used for the analysis of nanostructures either in liquids or in solids. During the measurement a coherent X-ray beam is sent through the sample and interacts with the electrons of the atoms. The interaction causes the scattering, which is measured by a detector. The profile of the scattered beam can be correlated, using mathematical model, to the size, shape, porosity ordered distribution and an internal structure of the nano-particles in the range size from $10\mathring{A}$ to $1000\mathring{A}$ of both amorphous and crystalline materials.

1.6 *In Situ Non Operando* SAXS and WAXS Measurement Previously Reported

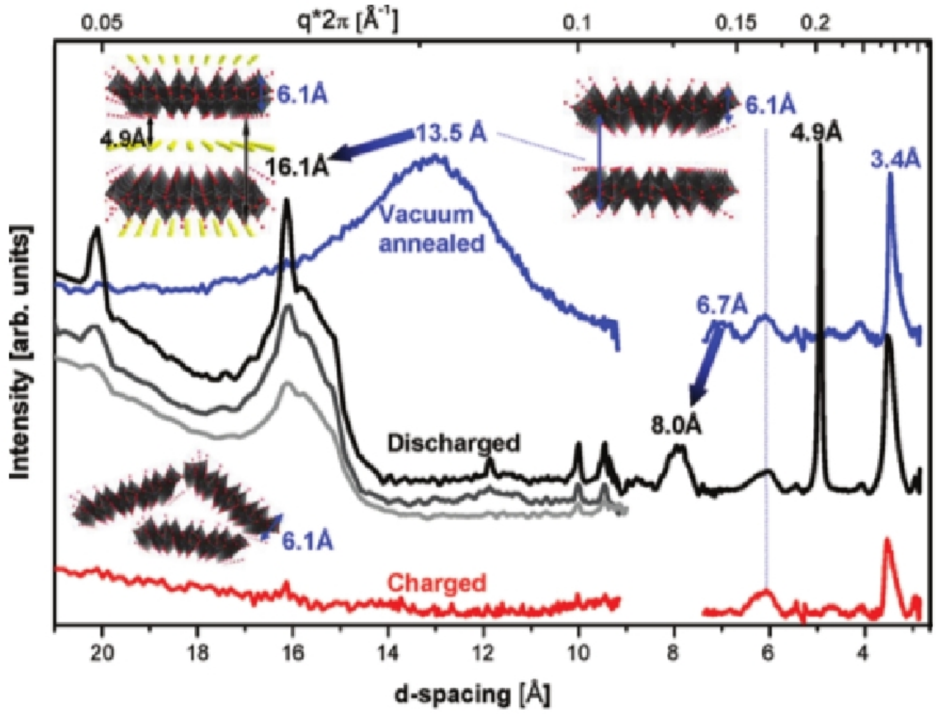

Figure 1.4: SAXS and WAXS spectra for bilayered V_2O_5: electrochemically deposited vacuum annealed sample (blue); after discharging with the current of $630\mu A$ (black), $120\mu A$ (gray), $20\mu A$ (light gray); and after cycling at $120\mu A$ in charge state (red). Model structures and critical interlayer spacing depicting transformation occurring upon Na^+ intercalation and de-intercalation are also shown [18].

An example of *in situ non operando* analysis is presented in Figure 1.4 [18]. In this case the SAXS and WAXS measurements were performed for the characterization of a cathode made of bi-layered vanadium oxide. The blue line is the result of the sample deposited electrochemically and annealed in vacuum. Meanwhile the black, the grey and the light grey lines are the results of measurements on the cathode charged at $630 \mu A$, $120 \mu A$ and $20 \mu A$, respectively. The red line is the result obtained at $120 \mu A$ discharging the cathode. The experiment consisted of an *in situ* SAXS and WAX characterization of the material in *non-operando* condition. This means that the X-ray structural analysis was performed after the galvanometric measurement. The SAXS and WAXS profiles were measured at the Advanced Photon Source (APS) synchrotron at Argonne Nationa Lab. After the discharge the diffraction peaks shifted to larger interplanar distance. In particular the peaks (001) and (002) shifted from $13.5 \mathring{A}$ to $16.1 \mathring{A}$ and from $6.7 \mathring{A}$ to $8.0 \mathring{A}$, respectively. Furthermore, the authors could observe that the layers of vanadium oxide became more ordered upon the sodium intercalation. In conclusion, they built a cell with a capacity of $250 \frac{mAh}{g}$ and were able to perform a *in situ non-operando* characterization. Their work is similar to the ours, presented in this thesis. However, their cell could not combine simultaneously the electrochemical and the X-ray characterization, while the cell used for this thesis can do.

1.7 Our Progresses

The test carried out with our new *in-house* built cell has shown the validity of the device. For the first time the galvanometric and the X-ray structural analysis were measured simultaneously. This work is a progress comparing to the one published by S. Tepavcevic, because WAXS and SAXS are performed in *operando* condition. The *in-house* built cell is a promising tool to be able to follow the structural change of the battery materials in real time.

Chapter 2

Theory of Batteries and Characterization Techniques

2.1 Batteries

The non-rechargeable batteries were the first batteries developed. They are defined as *primary* batteries and they can storage energy by a *irreversible* chemical reaction, which means that when the chemical reaction is finished the batteries can not provide energy any longer. The rechargeable batteries are also called *secondary* batteries, and they can provide energy by a reversible chemical reaction. When this chemical reaction is finished, it is possible to recharge the battery applying an electric current in the opposite polarization than the one provided by the battery itself. The applied current provides the energy to the system to return to the charge condition, so the batteries can be used again.

The first battery was built by Alessandro Volta and it is shown in Figure 2.1. The device consists of different metal disk pairs aligned in a column (in Italian language *pila* means put object on the top of each other). Each pair is separated from the next one by a cloth or cardboard disk soaked in an acid water solution of sulphuric acid called *brine*. Volta obtained the best performance using a series of alternating copper-zinc (Cu-Zn) disks pair. The contact between the copper and zinc builds

Figure 2.1: *Pila di Volta* in exposition at Tempio Voltiano, Como (Italy)

a chemical potential. The copper remains stable while the metal zinc releases two electrons and then two Zn^{2+} cations move from the metal to the solution. The chemical interaction between the water and sulphuric acid generates the H_3O^+ ions, when this cation interacts with the electron the H_3O^+ ion is transformed into water and a gaseous molecular of hydrogen H_2. The *pila di Volta* provides $0.7V$ that is related to the two semi couples of Zn/Zn^{2+} and H_2/H_3O^+. This battery could work only for a few hours because the solution starts to decompose forming H_2 gas. A more efficient primary cell was built by John Frederic Daniell who developed so called *Daniel Cell* in 1836. This cell and the others, developed following the same reaction scheme, were used to provide energy to the telegraph network, and all of them become useless when the chemical reaction is completed. In 1859 Gaston Plante invented the first rechargeable battery based on lead-acid. In this battery the two electrodes are a lead plate and a lead oxide separated by sulphuric acid. In the 19th century also other kinds of recharged batteries were developed

1. Leclanche cell (1866)

2. Zinc-Carbon cell (1876)

3. Nickel-Cadmium cell (1899)

The most used rechargeable batteries were the NiCd, lead-acid (used mainly for the car), NiMH (nickel metal hydrade), NiZn and AgZn, until the introduction of the LIBs in the market in 1990 [19].

2.1.1 Primary Batteries and Basic Concept of Thermodynamic and Electrochemistry

The *pila di Volta* is described as an *electrochemical cell* or *Galvanic cell*, because it uses the spontaneous Galvani reaction. This device can store chemical energy and provides electricity by a *spontaneous redox reaction* [20]. A reaction is thermodynamically spontaneous if the free Gibbs energy $\Delta_r G$ is negative. The standard Gibbs free energy $\Delta_r G^{\ominus}$,(IUPAC defined the standard condition as temperature=$273.15K$ and pressure=$100.00kPa$) [20]

$$\Delta_r G^{\ominus} = -RTlnK \tag{2.1}$$

where the R is the perfect gas constant, T is the absolute temperature measured in Kelvin degree, and K is the equilibrium constant of the reaction. The $\Delta_r G^{\ominus}$ is negative when $K > 1$. The general thermodynamic expression for the Gibbs free energy (2.1) has a more useful identity for the electrochemistry application

$$\Delta_r G^{\ominus} = -nFU^{\ominus} \tag{2.2}$$

where n is the number of electron per mole exchanged during the reaction, F is the Faraday constant and $U^{\ominus}$ is the standard potential of the electrode. During the reaction, a material that releases many electrons develops a low potential, while a material that releases a few electrons develops a high potential. In Figure

2.2 the materials under investigation for NIBs application are placed according to their capacity and potential. The candidate materials for anode application have their redox potential values, against Na^+/Na electrode, in the potential range of $0 - 2V$, while the other materials can be used as cathode. While designing a battery, it is necessary to choose either to have many electrons, so more current and low difference of potential, or to have a few electrons and high difference of potential. A reaction is defined as redox when it involves the exchange of the electrons from one chemical specie to another. The word redox is the combination of two words *REDuction* and *OXidation* because two processes happen at the same time (there could not be an oxidation if something is not reducing). The reduction is the electron gain process and the oxidation is the electron loss process[21]. In the device providing energy, for convention, the electrode at lower potential is defined as *Anode* where the oxidation takes place. The counter electrode, at higher potential, is the *Cathode* where the reduction happens [20].

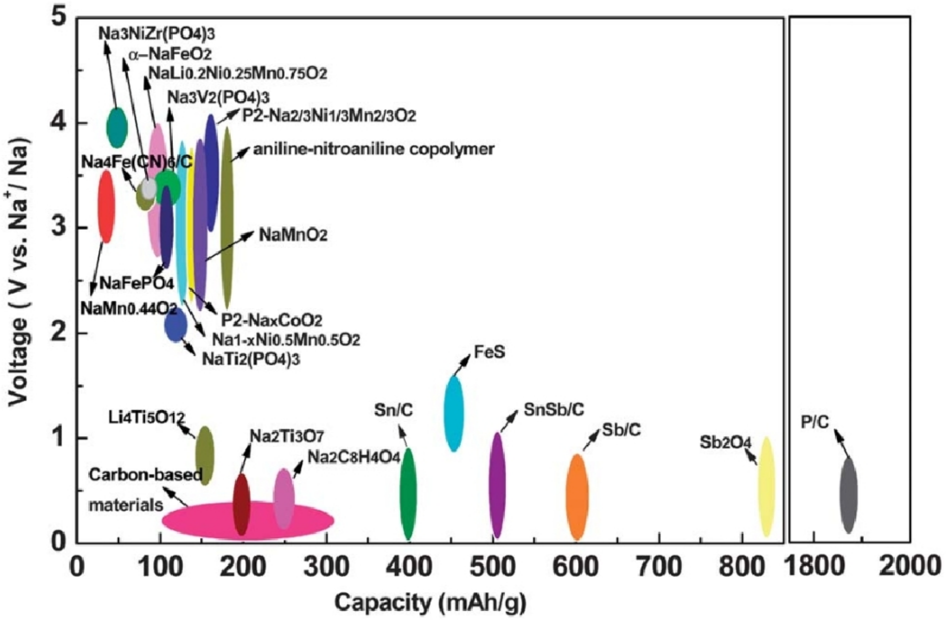

Figure 2.2: The relationship between capacity and voltage for present electrode materials in NIBs [1]

The spontaneous reaction that happens when a piece of metallic zinc is immersed in a water solution containing a salt of copper can be described as:

$$Zn_{(s)} + Cu^{2+}_{(aq)} \rightarrow Cu_{(s)} + Zn^{2+}_{(aq)} \tag{2.3}$$

The zinc starts immediately dissolving and becomes the cation for the salt, while the copper starts crystallizing as metal. During the process the zinc releases two electrons per atom, changing the oxidation state from 0 to 2+, while the copper reduces from 2+ to 0, becoming metal. The process involves the exchange of electrons between zinc and copper [22].

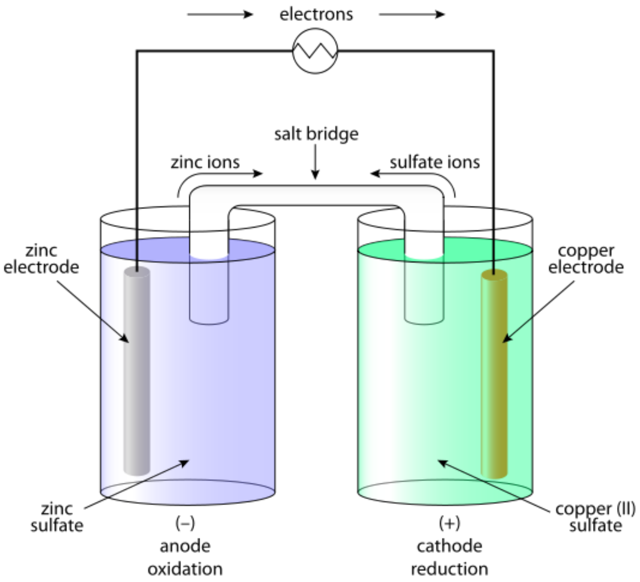

Figure 2.3: Scheme of Daniell cell $Zn_{(s)}|ZnSO_{4(aq)}||CuSO_{4(aq)}|Cu_{(s)}$

Figure 2.3 is schematic representation of the Daniell cell that uses the reaction 2.3 to provide electricity. The two electrodes of zinc metal and copper metal are separated and immersed in water solution containing zinc sulphate ($ZnSO_4$) and copper sulphate ($CuSO_4$), respectively. The two solutions are bridged by a salt bridge and the two electrodes are connected by a conductive wire. When the wire connection is closed electrons start flowing from the zinc to the copper, and the atoms of zinc are oxidized according to the oxidation reaction

$$Zn_{(s)} \rightarrow Zn^{2+}_{(aq)} + 2e^{-} \tag{2.4}$$

while the zinc electrode progressively dissolves in the solution. When the electrons arrive on the copper electrode, they reduce the cation of the salt in the solution according to the reduction reaction

$$Cu^{2+}_{(aq)} + 2e^{-} \rightarrow Cu_{(s)} \tag{2.5}$$

The copper of the solution starts depositing on the electrode. In order to maintain the electro-neutrality of the two solutions the cations and the anions of the salt bridge are dissolved respectively in the copper and in zinc solutions. Therefore, according to the definition above, the zinc electrode is acting as anode and copper one as cathode. The battery is a device that allows the spontaneous redox reaction but at the same time pushes the electrons in an external circuit to make electrical work [22].

Every redox reaction can be written as two semi reactions. In fact the eq.(2.3) can be obtained as sum of (2.4) and (2.5). The oxidized and reduced species in half-reactions constitute a *redox couple*. The eq. (2.3) is spontaneous (in the sense that K>1) in the direction corresponding to a negative value of the resulting $\Delta_r G^{\ominus}$. Since the two half-reactions must always happen in pairs in any actual reaction, only the difference in their standard Gibbs free energy has a physical meaning [21]. Therefore, for convention one half reaction has $\Delta_r G^{\ominus} = 0$ at every temperature. The *Standard Hydrogen Electrode* (SHE) has been chosen for this convention. The SHE consists of a platinum electrode (covered by porous platinum to improve the surface of contact), immersed in a water solution of hydrochloric acid with concentration of $1M$. The platinum is used as electron collector, because it is chemically inert. Hydrogen gas is injected in the solution at a pressure of $1atm$. The real electrode is the hydrogen that collects electrons from the platinum in order to make the following reaction

$$2H^{+}_{(aq)} + 2e^{-} \rightarrow H_{2(g)} \tag{2.6}$$

Therefore a galvanic cell built with a zinc electrode and a SHE works according to the following reaction:

$$Zn^{2+}_{(aq)} + H_{2(g)} \rightarrow Zn_{(s)} + 2H^{+}_{(aq)} \tag{2.7}$$

That is the sum of the reaction (2.4) and (2.6) and its standard Gibbs energy is $\Delta_r G^{\ominus} = +147kJmol^{-1}$. Therefore, by using the eq. (2.2) the standard potential is $U^{\ominus} = 0.7V$.

The standard potential is a function of the temperature and the reaction quotient Q. For a general reaction Q is define as follow

$$aOx_A + bRed_B \rightarrow a'Red_A + b'Ox_B \tag{2.8}$$

$$Q = \frac{[Red_A]^{a'}[Ox_B]^{b'}}{[Ox_A]^{a}[Red_B]^{b}} \tag{2.9}$$

The Gibbs free energy out of standard condition is

$$\Delta_r G = \Delta_r G^{\ominus} + RTlnQ \tag{2.10}$$

The combination of the eq.(2.2) with the eq.(2.10) is the Nerst equation

$$U = U^{\ominus} - \frac{RT}{nF} lnQ \tag{2.11}$$

That can estimate the open circuit cell voltage in full charge state and represents also the limit voltage for the electrode. When the reaction has reached the equilibrium, the reaction quotient is equal to the reaction constant ($Q = K$).

The maximum voltage for the full cell in the charged state in open circuit is [20]

$$U^{\ominus}_{cell} = U^{\ominus}_{cathode} - U^{\ominus}_{anode} \tag{2.12}$$

However, this is only a theoretical estimation, while the charge transfer and the kinetic of the reaction are the limiting factors. Furthermore, the charge of the metal immersed in the liquid electrolyte attracts ions of the opposite charge diluted in the electrolyte and the polar molecules in the solvent will align according to the electric field. This phenomenon produces the formation of an *electrical double layer*, a kind of barrier that the oxidized and reduced species have to overcome. This layer limits the kinetic of the reaction [23].

2.1.2 Secondary Batteries

In a secondary battery the redox reaction is *reversible*. If an electric current is applied at a potential $U > U_{cell}$, the electrons flow to the anode through the external circuit and the cations diffuse from the cathode to the electrolyte. In this recharging mode the oxidation happens at the cathode and the reduction at the anode. The cations diffuse between the electrodes toward the *electrolyte*, which can be solid or liquid [20]. The use of the batteries determines the shape and size so sometimes secondary batteries are classified according to their use [20]:

1. Portable batteries: small size batteries for portable devices, a broad category of items from toys to laptop;

2. Transport batteries: the batteries used for transport vehicles;
3. Stationary batteries: batteries located permanently in one place. They are connected to the grid or used as back up for emergency. For instance, back up of expensive instruments, emergency lights or batteries connected to hospital, govern or military building is also included in this category.

2.1.3 The Specific Capacity of the Batteries

The weight and size of the batteries are related to their use. The higher the quantity of active materials inside the batteries can store the more energy, which implies a correlation between the weight of the batteries and the charge stored.

The quantity Q_c of electricity involved in the electrochemical reaction is

$$Q_c = \frac{mnF}{M} \tag{2.13}$$

where m and M are the mass and the molar mass, respectively, of the electroactive material in the cell and n is the number of the electron exchanged per mole during the reaction [20].

The eq. (2.13) is the theoretical molar capacity of the quantity m of material. If the equation is divided by m, it becomes the *specific capacity* of the material

$$\frac{Q_c}{m} = C = \frac{nF}{M} \tag{2.14}$$

expressed as $\frac{mAh}{g}$ [20]. The specific capacity of a battery C_B is calculated according to the following equation

$$\frac{1}{C_B} = \frac{1}{C_C} + \frac{1}{C_A} + \frac{1}{C_L} \tag{2.15}$$

where C_C and C_B are the specific capacities of the cathode and of the anode, respectively, C_L is the *Capacity Lost*, relate to the weight of the *non-electroactive* *material* (for example the external box, the metallic part and so on). The value of specific capacity when the system is reported back in the initial state is defined *reversible capacity.* During the first discharge of the batteries a small quantity of the liquid electrolyte is decomposed forming a carbonate layer on the electrode, that is called *Solid Electrolyte Interface* (SEI). This layer is a kind of protection for the electrode against the degradation. The cations diffuse from the liquid electrolyte toward the electrode through the SEI. Also this layer can accumulate cations inside itself. For this reason during the first discharge a higher capacity value than the theoretical limit is often measured. Therefore, the reversible capacity measured at the end of the cycle is a more accurate value of the real capacity of the battery [24].

The Coulomb efficiency η_C is

$$\eta_C = \frac{Q_d}{Q_{ch}} \tag{2.16}$$

where the Q_d and $Q_c h$ are the quantity electricity during the discharge and the charge processes, respectively. η_C is the estimation of the efficiency of the process and it is never 100% due to the secondary reactions [25].

2.1.4 Reaction Mechanisms

In a secondary battery, the reversible reaction implies that one part of the component remains stable and not destroyed by the reaction. There are three mechanisms useful for the reversible reaction:

1. Conversion reaction;
2. Intercalation reaction;
3. Replacement reaction.

Conversion Reaction

The conversion reaction is based on the spontaneous phase changing of the active material when it is in contact with the cation. This kind of reaction has several advantages:

- high specific capacity
- the material becoming nano-structured during the fist electrochemical cycle
- the redox potential controlled by the electro negativity of the anion.

Chemical compound like phosphide, nitrides and metal-oxide can be used as anode and fluoride compound can be used as cathode. Several metal oxide like Cu_2O, CoO, Fe_2O_3 were studied for LIBs application and they work according the following reaction [24][26]

$$MO + 2Li + 2e^- \leftrightarrow Li_2O + M^0 \tag{2.17}$$

Several reactions are reported for NIBs based on antimony, phosphorus, tin alone or in composite material with carbon: *a-P/C*, *Sb/C*, *SnSb/C* and *Sn/C*. If we consider the reaction of a-P/C with sodium [1]

$$P + 3Na^+ + 3e^- \leftrightarrow Na_3P \tag{2.18}$$

the carbon, working as a matrix, is a kind of framework that reduces the mechanical stress, due to the volume variation during the charge-discharge cycle. And thus due the volume of the phosphorus nano-cluster increases up to 308% [15] forming Na_3P. Carbon is also the electron conductive material that provides the flux of the electrons necessary for the reaction. If the mechanical stress breaks the phosphorus clusters and part of the material is not any longer in contact with the carbon frame and the reaction cannot happen and that amount of material remains as useless weight in the battery.

The orthorhombic $FeSb_2$ is an interesting anode material due to its theoretical capacity of $540\frac{mAh}{g}$ and its simple synthesis procedure. $FeSb_2$ is a brittle material, so it can be reduced in nano-particle size by a technique called ball milling, as described in the experimental section (Chapter 3)[6]. Phosphorus and antimony are both member of fifth group of the periodic table of the element. When they react with sodium they form the alkaline non-metal compound A_3B with hexagonal space group $P\frac{6_3}{m}mc$. Each atom of phosphorus and antimony coordinates three atoms of sodium [27]. Tables 2.1 and 2.2 summarise the structure and property of the a-P/C, $FeSb_2$, Na_3P and Na_3Sb. The specific capacity of the $FeSb_2$ is lower than that of a-P/C because antimony is almost four times heavier than phosphorus. Furthermore, iron remains in the electrode but does not contribute any longer to the chemical reaction.

	Na_3P	Na_3Sb
Space group	$P\frac{6_3}{m}mc$	$P\frac{6_3}{m}mc$
a	$4.9512\mathring{A}$	$5.3550\mathring{A}$
c	$8.7874\mathring{A}$	$9.4960\mathring{A}$
Atomic coordinate Na1	000 000 250	000 000 250
Atomic coordinate Na2	333 667 583	333 667 583
Atomic coordinate P/Sb	333 667 250	333 667 250
$P_{molarmass}$	$30.973\frac{g}{mol}$	-
$Sb_{molarmass}$	-	$121.760\frac{g}{mol}$

Table 2.1: Structural comparison of Na_3P and Na_3Sb [27][28]

	a-P/C	$FeSb_2$
Specific Capacity	$2500\frac{mAh}{g}$	$540\frac{mAh}{g}$
Space group	Amorphous	$Pnn2$
a	-	$5.8328\mathring{A}$
b	-	$6.5376\mathring{A}$
c	-	$3.1973\mathring{A}$
Molar Mass	$30.973\frac{g}{mol}$	$299.365\frac{g}{mol}$

Table 2.2: Structural comparison of a-P/C and $FeSb_2$ [29]

Intercalation Reaction

The candidate material for an intercalation reaction has to possess three important characteristics:

1. Layers or channel crystal structures

2. One or more elements that can change oxidation state

3. The capacity to resist to the mechanical stress due to the variation of volume

Also in the intercalation reaction there is a phase change, like for the conversion reaction. However, the crystal structure has to have channels or layers where the cation can be intercalated or be drawn. During the intercalation (reduction process) the volume increases but the rest of the structure remains almost constant except for the fact that at least one element has to change the oxidation state in order to keep the electro-neutrality of the crystal. The oxidation process happens when the cation is removed from the structure, at the same time the volume of the crystal decreases.

The intercalation reaction is at the base of the working mechanism of the well known LIB developed by Sony company and Figure 2.4 is a schematic representation. It consists of $LiCoO_2$ as cathode and graphite as anode [2]. Both materials are layer-structured. In graphite the hybridization state of the orbital $2sp^2$ of the carbon allows the formation of the six carbon ring that reminds an honeycomb structure. All the carbon-carbon bonding lye in a flat plane and each plane is connected to the other by weak *Van der Waals* bonding. The distance between each layer is $3.35\AA$ but, when the lithium intercalates among them, the distance increases up to $3.71\AA$ [30]. $LiCoO_2$ is an hexagonal $R\overline{3}m$ crystal and it has the rock-salt structure with alternate plane of lithium and cobalt. In the plane (111) the oxygen atoms form a close-cubic lattice. Each cobalt atom is surrounded by six oxygen atoms forming an octahedral polyhedron ordered in a layered structure [31]. The lithium atoms can be easily intercalated or drawn from this layer structure determining the formation of $LiCoO_2$ (discharge state) or of $Li_{1-x}CoO_2$ (charge state) [2]. The reaction mechanisms at the electrodes are:

$$C + xe^- + xLi^+ \leftrightarrow Li_xC \tag{2.19}$$

$$LiCoO_2 - xe^- - xLi^+ \leftrightarrow Li_{1-x}CoO_2 \tag{2.20}$$

The material called NASICON is an example of intercalation reaction for NIBs technology. It has the general chemical formula of $Na_xM_2(PO_4)_3$, where M can be vanadium, iron, titanium, niobium. Originally it was proposed as solid electrolyte rather than used as cathode. Its main characteristic is related to capacity of the transition metal to have different oxidation states *e.g.* V^{4+}/V^{3+} V^{3+}/V^{2+}, Fe^{3+}/Fe^{2+}, Ti^{4+}/Ti^{3+} Ti^{3+}/Ti^{2+}, Nb^{5+}/Nb^{4+} Nb^{4+}/Nb^{3+} which allow the exchange of two Na^+ per unit formula [1].

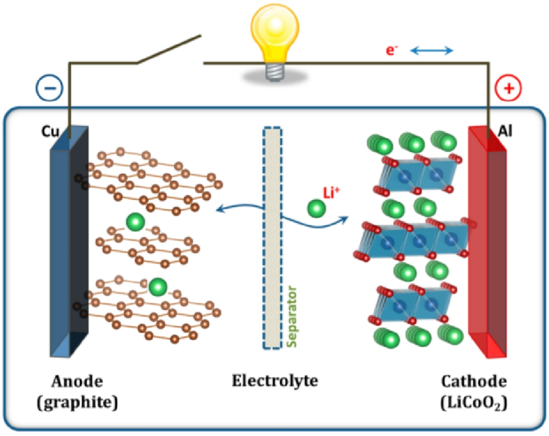

Figure 2.4: Scheme of the $|graphite|electrolyte|LiCoO_2$ battery [2]

Displacement Reaction

The displacement reaction happens when an intermetallic compound AB reacts with a cation Na^+ or Li^+ and the cation can displace partially or completely one of the two metals and produces a reduced phase *e.g.* Li_xB. This kind of reaction happens only if the lithiated or sodiated compound has a crystal structure similar to the original compound AB. These were studied for the LIBs technology since 1980s [32]. Several studies are reported about Cu_6Sn_5, $MnSb$ and $InSb$. For example lithium replaces part of the copper in the reaction with Cu_6Sn_5

$$10Li + Cu_6Sn_5 \leftrightarrow 5Li_2CuSn + Cu \tag{2.21}$$

The same reaction mechanism is reported for metal/non-metal compounds such as $FeCl$ and $NiCl$ [32] or metal-oxide like $NaTiO$ [33] and SnO [34].

$$2Na + MCl \leftrightarrow 2NaCl + M \tag{2.22}$$

2.1.5 Performances of Different Anode Materials

In the last decades LIBs were the main system studied for rechargeable batteries. The research concentrates in improving the performance of the cathode and the electrolyte, while graphite was the most used anode. This is clear in Figure 2.5 where the number of the cathode materials $(2 - 5V)$ is higher than the number of anode materials $(0-2V)$. Graphite cannot be used as anode for NIBs because the intercalation of sodium into the graphite layers is thermodynamically unstable. However, the theoretical specific capacity of the graphite to host a cation is only $372\frac{mAh}{g}$.

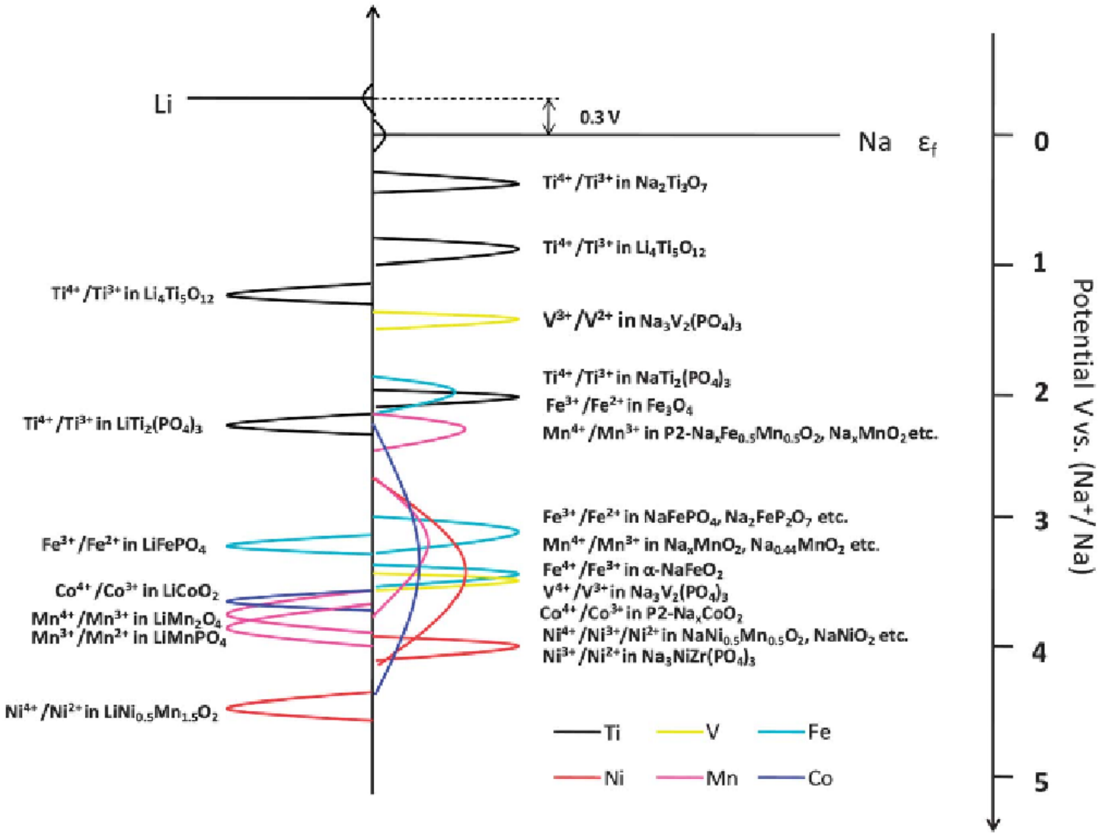

Figure 2.5: List of materials according to their redox potential [1]

Metallic sodium cannot be used as anode in commercial batteries because, like lithium, it is very reactive. Furthermore, the extremely high reactivity of the sodium in contact with liquid electrolyte provides the formation of an unstable solid electrolyte interface [1]. Several options are under investigation in order to find the appropriate candidate as anode material for commercial NIBs. Also other materials based on carbon are considered as new material. Polymers, carbon nanospheres, carbon nanotubes, carbon nanowires, porous carbon, and carbon obtained by glucose precursor are among the materials with a reversible capacity of $300\frac{mAh}{g}$ [1]. The oxide materials with layer or channel structures for intercalation reaction or oxides for conversion reactions can react with sodium in a similar manner as lithium, but with worse performance. For example $NiCo_2O_4$ can be used as anode and react with Na^+ and Li^+ toward a conversion reaction whose theoretical capacity is $890\frac{mAh}{g}$. Porous $NiCo_2O_4$ nano-flask and nano-belt exhibit a specific capacity of 1033 and $1056\frac{mAh}{g}$, respectively, because of the high surface area which provides a large contact area with the electrolyte [35]. However, when the same anode material is used in combination with sodium it has only the reversible capacity of $200\frac{mAh}{g}$ [1]. The Fe_3O_4 has a theoretical capacity of $926\frac{mAh}{g}$ and the compound Fe_3O_4/C reaches $1000\frac{mAh}{g}$ in the case of LIBs. The combination with carbon provides a slightly better specific capacity and good cyclability compared to the simple Fe_3O_4. However, when Fe_3O_4 is used as anode for a NIB its capacity exhibits only $248\frac{mAh}{g}$ [36].

a-P/C has a theoretical specific capacity of $2500\frac{mAh}{g}$, and can be considered as one of the best candidate for the high energy storage application. The *a-P/C* in combination with lithium has been reported to have a reversible capacity of $2413\frac{mAh}{g}$ [12]. The system with lithium is more efficient than the analogue with sodium. However, in this case the reversible capacity of the sodium system reaches the 80% of the reversible capacity of the lithium system. This is a huge improvement compared with the Fe_3O_4 anode, where the capacity of the sodium system is only the 26% of the lithium one. In Table 2.3 the reported values of the best measured specific capacities of different anode materials for NIBs are listed. The best performance of $FeSb_2$ ($350\frac{mAh}{g}$) [17] is close to the theoretical value of the graphite ($372\frac{mAh}{g}$). However the highest measured capacity is reported by *a-P/C* ($1960\frac{mAh}{g}$).

2.2 Galvanometric Measurement

The galvanometric measurement is an electrochemical analysis for the determination of the reaction kinetics and mechanism, performed with an apparatus called *galvanostat*. The galvanostat is a set in order to apply a constant current I or $-I$ and at the same time it measures the variation of the potential U of the cell. The current I is chosen according to theoretical capacity of the material C and the weight m of the active material in the electrode in order to perform a full discharge

Anode	Capacity $[\frac{mAh}{g}]$
Graphite (LIBs)	372
Carbon-Based Materials [1]	300
Metal Oxide [1]	200
Metal Sulphide [1]	450
NASICON [1]	140
Conversion Reaction [1]	300-600
$a\text{-}P/C$ [16]	1960
$FeSb_2$ [17]	350

Table 2.3: Theoretical capacity of graphite in LIBs and the best measured specific capacities for different NIBs anode materials

or a full charge in t hours

$$I = \frac{Cm}{t} \tag{2.23}$$

Usually, in the scientific literature, the information about the value of the applied current and the amount of active material in the electrode is not reported. Instead the notation $\frac{C}{t}$ is used to give information about the system. The cells, built with a metallic electrode made of sodium or lithium, are called *half cells* and they are used for experimental characterization to shed light on the behaviour of the counter electrode.

In this thesis the half cells are built using $a\text{-}P/C$ or $FeSb_2$ as anode and metallic sodium as cathode. When $-I$ is applied, the sodium reacts with the red phosphorus inducing a variation of its oxidation state from 0 to 3$-$ meanwhile antimony remains in oxidation state 3$-$, but it is separated from the iron. Since the reactions end with the formation of Na_3P and Na_3Sb, this process is called *sodiation* and it corresponds to a reduction reaction. According to the definition given in section 2.1.1 it is the charging process.

The opposite reaction, when the polarization of the current change involves the oxidation at the electrode under analysis, is a process called *de-sodiation*, because the sodium is removed from the active material. The reaction condition opposes the half cell when studying cathode materials. For the cathode material when I and $-I$ are applied, the half cell is charged and discharged. From now on the chemical process will be described as sodiation and de-sodiation of the anode, because the idea to charge the half cell applying $-I$ and to discharge it applying

I is counter-intuitive. A generic profile of galvanometric measurement is shown in Figure 2.6. The specific capacity (blue line), the potential (black curve) and the applied current (red line) are represented depending on time. At the beginning the galvanostat applies a negative current -I inducing the sodiation and the potential changes from the initial state U_1 to $U < 10mV$. When the potential of the cell is below $10mV$, the control set up change the polarization of the current. Thus, +I is applied and it induces the desodiation, up to U_2.

The potential gradually changes because the electron flux induces the chemical reaction. Therefore, the reactants are exhausting and the ratio of the product/reactant changes at the electrode surface. The deviation of the electrode potential from its equilibrium value is called *overpotential* [23].

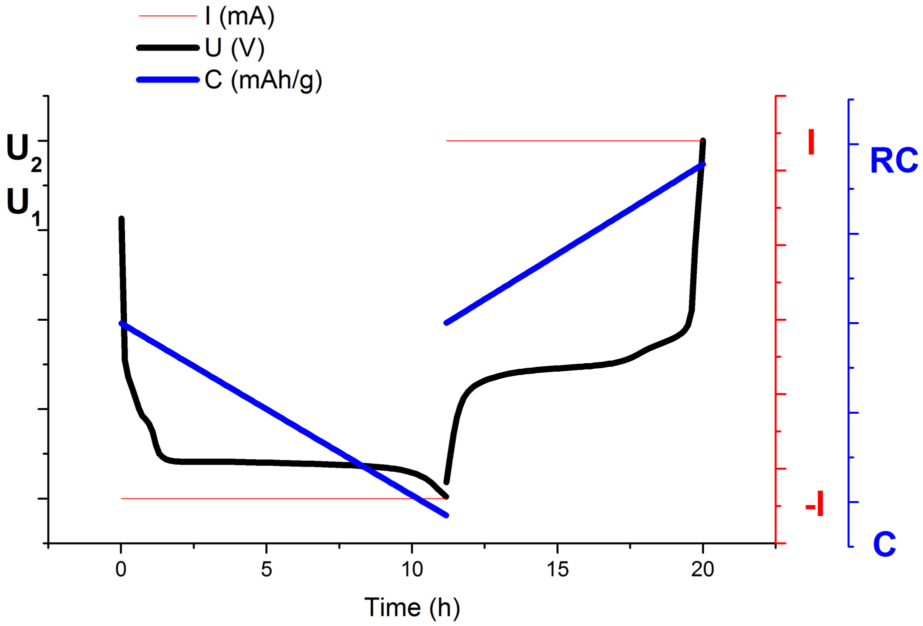

Figure 2.6: Generic profile of a galvanometric measurement: (black) the potential U, (blue) specific capacity (C= capacity and RC=reversible capacity) and the (red) the intensity of applied current

The measured data can be plotted in a graph potential *vs.* specific capacity, as reported in Figure 2.7. This kind of representation of the experimental data allows to correlate directly potential and capacity. The variation of the slope is related to the variation of concentration of one single phase domain, while a plateau corresponds to a two phases domain.

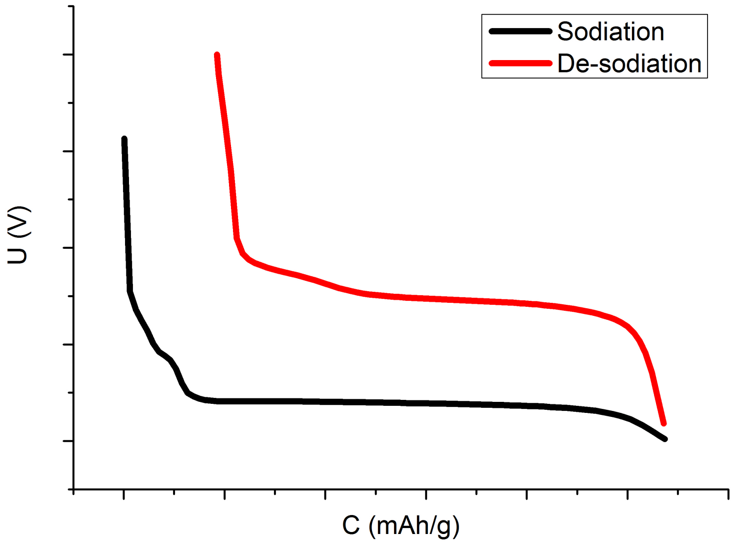

Figure 2.7: Potential *vs.* specific capacity of the profile reported in the Figure 2.6

2.3 The X-ray Source: Synchrotron

The synchrotron radiation source is a circular particle accelerator where electrons or positrons are accelerated by magnetic field close to the speed of light. The vacuum technology is necessary to avoid gas-electron collision that can decelerate the charge particles. According to the classic theory of electromagnetism a charge particle emits radiation when it is accelerated and the energy of the radiation depends on the speed of the particle and other geometrical parameters of the synchrotron. The energy emitted per unit of time is

$$P = \frac{2e^2cE^4}{3R_o^2(m_ec^2)^4} \tag{2.24}$$

where e is the charge of the particle, c is the speed of the light, E is the energy of the particle, m_e is the electron mass at rest, and R_o is the bending radius of the orbit [37]. The synchrotron facilities are the X-ray source with the *highest brilliance* compared to the conventional laboratory source like *X-ray tube* and *Rotating Anode*. The brilliance is an important characteristic of the radiation source which is defined as the number of photons emitted per second per unit of solid angle per area. The high brilliance of the synchrotron guaranties the quantity of photons necessary for the experiment [37]. The *in situ operando* measurements were performed at the ESRF in Grenoble (France), whose scheme is represented in Figure 2.8. This synchrotron uses electrons as charge particle that are produced by an electron gun and it consists of:

1. the *Linac*;
2. a *Booster*;
3. a *Storage ring*;
4. several *Beam lines*

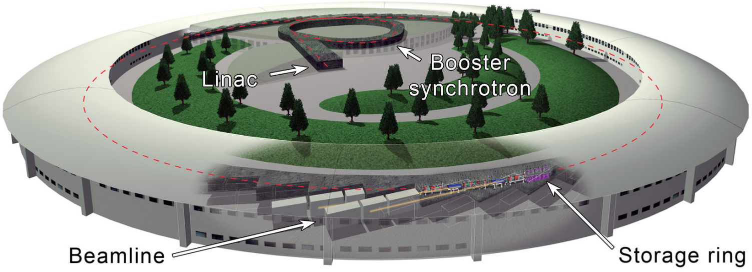

Figure 2.8: Schematic representation of the ESRF [38]

The Linac is a linear accelerator that accelerates the electrons up to $0.2 GeV$ before to be injected in the booster. The booster is like a small synchrotron whose circumference is $300m$ long, and here the electrons are accelerated up to $6GeV$ [38]. Then the electrons pass to the storage ring where they can circle for several hours because there is a pressure of $10^{-9} mbar$ and the RF-cavities magnets resupply the energy that electrons have lost emitting X-ray photons. The beam lines are the place where the X-ray beams are directed and used for the experiments [38]. The storage ring (Figure 2.9) has a circumference of $844m$ and the circular path is impressed to the electrons by bending magnets (Figure 2.10), which were at the base of the first generation of synchrotron. The ESRF is a second generation of synchrotron so there are also the *undulator* (Figure 2.11) and the focusing magnet. Figure 2.9 shows the disposition of the magnet in the storage ring which is a polyhedron composed of 32 curved and 32 straight segments placed in alternating

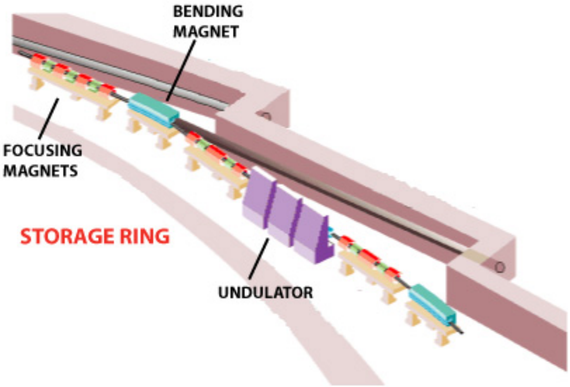

Figure 2.9: Scheme of the storage ring of the ESRF [38]

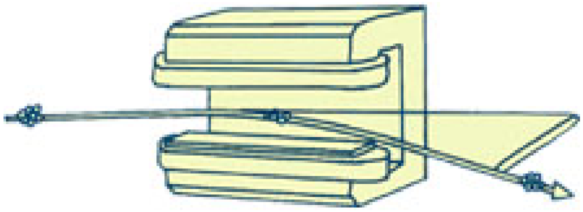

Figure 2.10: Scheme of the bending magnet [38]

order. The bending magnets are located in the curved segments [38]. When the electrons are bended they emit a continuous radiation spectrum from microwaves to X-rays. The focusing and undulator magnets are placed in the straight segment. The former focuses the electrons close to their ideal orbital path and the latter, also named *insertion device*, is used to produce X-rays. The insertion device is an array of small magnets that produce a magnetic field to be able to force the electrons in an undulating path, like a sea wave. When the X-ray photons are generated the electrons are bended every time and they interact among them to create an X-ray beam more focused and brilliant than the one obtained by one single bending magnet. Furthermore, in this case the radiation spectrum is not continuous but the photons are concentrated at a certain wavelength, called *harmonics*, and such wavelength can be selected by changing the distance among the small magnets [38].

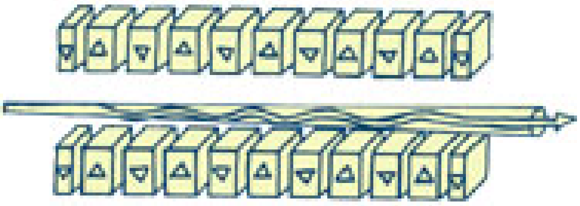

Figure 2.11: Scheme of the undulator or insertion device [38]

2.4 X-ray-Matter Interaction

The X-ray interacts with the matter by scattering and absorption and those processes are at the base of different analytical techniques. For a better comprehension of the WAXS and SAXS it is important to explain them as first step. There are two scattering mechanisms: the *inelastic Compton scattering* and the *elastic Thomson scattering* [39], meanwhile the *X-ray absorption* is a limiting factor for the WAXS and SAXS [40].

2.4.1 Compton Scattering

A. H. Compton described an inelastic photon-electron collision. According to the classic theory of electro-magnetism the radiation should not change the energy. However, when a photon collides with a free electron it is scattered and it gives a part of its energy to the electron. The wavelength variation between the incident and scattered photons is

$$\Delta\lambda = 0.024(1 - cos\theta) \tag{2.25}$$

where θ is the scattering angle and $0.024\mathring{A}$ is the Compton electron wavelength which is the result of the product of the Plank constant h, the electron mass m_e and the light speed c: $\frac{h}{m_e c} = 0.024\mathring{A}$. This kind of scattering is incoherent due to the wavelength variation and does not provide any interference phenomena. Therefore, it is impossible to extract structure information and it is a part of the featureless background radiation [39].

2.4.2 Thomson Scattering

The elastic Thomson scattering (Figure 2.12) is the physical phenomenon at the base of the interference pattern that carries structure information about the particle. When an X-ray photon collides with a free electron (red dot) without energy transfer, the electron start oscillating at the same frequency as the incoming radiation. According to the classical theory of electromagnetism an accelerated charge particle becomes a source of electromagnetic field [39]. In this case the electron emits radiation with the same frequency and intensity I_{eTh}

$$I_{eTh} = I_0 \frac{e^4}{m_e^2 r^2 c^4} sin^2 \varphi \tag{2.26}$$

where e is the electron charge, r is the distance from the emitting point, Q is the point where the scattered radiation is measured, and φ is the angle between Q and the incident radiation direction. The *coherent waves* are produced when all the waves, emitted by neighbouring atoms, oscillate synchronously. According to the eq. (2.26) only the radiation scattered by electrons contributes to the measured intensity, because neutrons do not have charge and protons are 1837 times heavier than electrons. Therefore, the intensity of the scattered radiation from protons is six order of magnitude lower than the one scattered by electrons [39].

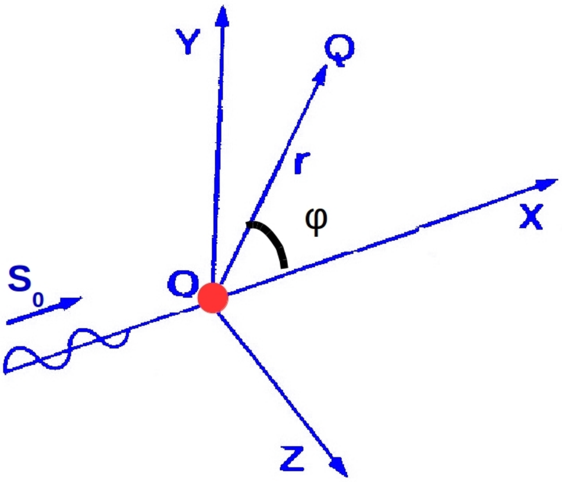

Figure 2.12: Thomson scattering scheme. The red dot is an electron, Q is the point where the scattered radiation is measured and φ is the angle between the vector $\mathbf{s}_0$ and Q [39].

2.4.3 X-ray Absorption

The scattered X-ray photons are a part of the beam that passes through the sample. However, it is important to specify that the X-ray absorption is the third interaction phenomenon with the matter. A part of the radiation is absorbed by the sample and converted in heat or X-ray fluorescence. The X-ray fluorescence happens when an X-ray photon of the incident beam interacts with a core electron of an atom [40]. Then the electron uses the energy to go out of the atom and a hole remains in its place. The atom reorganizes the electron configuration to replace the missing electron: one electron moves from the external shell to the inner core emitting a fluorescence X-ray photon whose wavelength is typical of chemical element. There are also analytical techniques based on the absorption like the *X-ray Absorption Near-Edge Structure* (XENES), the *Near-edge X-ray Absorption Fine Structure* (NEXAFS) and the *X-ray Fluorescence Spectroscopy* (XRF) but they are not topic of this thesis. The absorption is a limiting factor because it reduces the number of photons that could be used for the SAXS and WAXS analysis [40]. Furthermore the X-ray fluorescence provides an isotropic radiation that contributes to the background of the measured signal. It is important to reduce the absorption in order to have a good quality of SAXS and WAXS data. Therefore the wavelength for the experiment has to be chosen carefully by considering the chemical elements inside the sample. It defines a condition, called *absorption edges*, where the electrons have the highest probability to be expelled and the absorption is more efficient [40].

2.5 Wide Angle X-ray Scattering

The history of modern crystallography started with the discovery of the X-ray by W. C. Röntgen and the pioneer work of M. von Laue on the use of the natural crystals as diffraction lattice for the X-ray. Because the materials inside the *in-house* built cell are powders the theory of the WAXS corresponds to that of the conventional *Powder X-ray Diffraction* (XRD)

2.5.1 Element of Crystallography

In the solid crystalline state the atoms or molecules or group of molecules are placed in a periodic geometry, the basic component that is repeated in all the direction is contained in the *elementary cell* (Figure 2.13). A parallelepiped is defined by the three vectors of **a**, **b**, **c** and the three angles of α, β, γ , also called *cell parameters*. The three capital letters A, B, and C in Figure 2.13 indicate the three faces of the primitive cell. The face A is defined by the vector **b** and **c**, while the face B is defined by the vector **c** and **a** and the last face C is defined by the vector **a** and **b**. Each elementary cell is represented by a point and all points form the *direct lattice* [41].

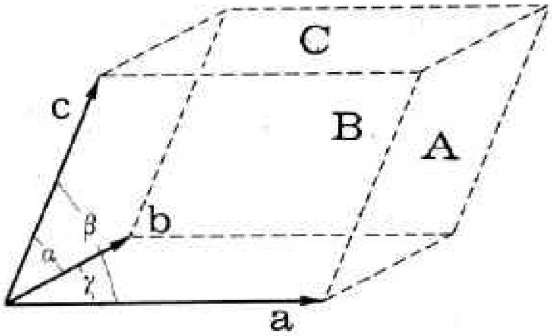

Figure 2.13: Primitive Cell with the lattice parameter and the face A, B and C [41]

The position of each point inside the direct lattice can be identified by the vector

$$\mathbf{r}_{uvw} = u\mathbf{a} + v\mathbf{b} + w\mathbf{c} \tag{2.27}$$

$[uvw]$ are integers. There are only seven combination of the lattice parameters determining the *seven crystalline systems* reported in Table 2.4

The function $L(\mathbf{r})$ based on the property of the *Dirac delta function* (Appendix

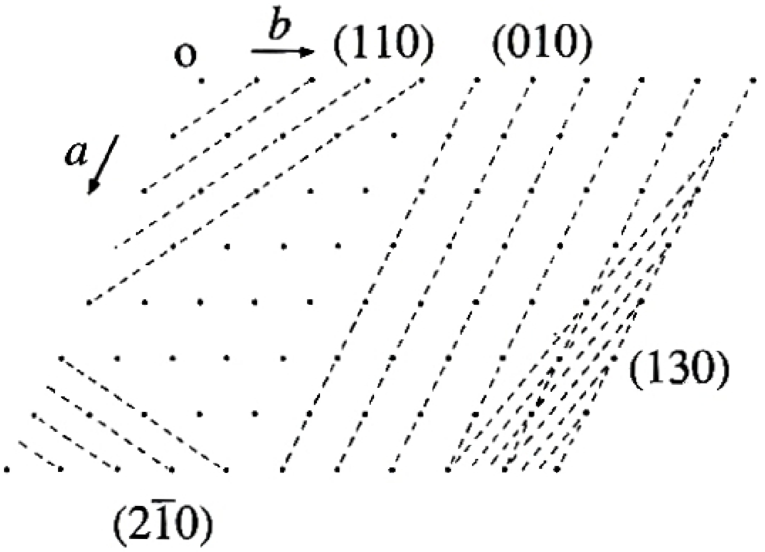

Figure 2.14: 2D-direct lattice with Miller index [41]

Triclinic	$a \neq b \neq c$	$\alpha \neq \beta \neq \gamma$
Monoclinic	$a \neq b \neq c$	$\alpha = \gamma = 90° \beta \neq 90°$
Orthorhombic	$a \neq b \neq c$	$\alpha = \beta = \gamma = 90°$
Tetragonal	$a = b \neq c$	$\alpha = \beta = \gamma = 90°$
Trigonal	$a = b \neq c$	$\alpha = \beta = 90° \gamma = 120°$
Hexagonal	$a = b \neq c$	$\alpha = \beta = 90° \gamma = 120°$
Cubic	$a = b = c$	$\alpha = \beta = \gamma = 90°$

Table 2.4: Crystal Systems

A.2) describes mathematically an infinite direct lattice

$$L(\mathbf{r}_{uvw}) = \sum_{u,v,w=-\infty}^{+\infty} \delta(\mathbf{r} - \mathbf{r}_{uvw}) \tag{2.28}$$

the function is different from zero only when $\mathbf{r} = \mathbf{r}_{uvw}$. The eq. (2.28) is important to define other two basic concepts of the crystallography: the *reciprocal lattice* and the *electron density function* $\rho(\mathbf{r})$ of the crystal [39]. The reciprocal lattice is the *Fourier transform* (Appendix A.3) of the function $L(\mathbf{r})$

$$T[L(\mathbf{r})] = \int_S \sum_{u,v,w=-\infty}^{+\infty} \delta(\mathbf{r} - \mathbf{r}_{uvw}) exp(2\pi i \mathbf{r}^* \mathbf{r}) \mathrm{d}\mathbf{r} = \frac{1}{V} \sum_{h,k,l=-\infty}^{+\infty} \delta(\mathbf{r}^* - \mathbf{r}^*_{hkl}) \tag{2.29}$$

The result is a discontinues lattice of points like the direct lattice, defined in the integration space S. V is the volume of the elementary cell and (hkl) are the well-known Miller Index used to indicate the crystallographic planes (Figure 2.14). The Miller index means that the plane of the family (hkl) divided $\mathbf{a}$, $\mathbf{b}$ and $\mathbf{c}$ in h, k and l parts, respectively. Since each node of the reciprocal lattice corresponds to a family of planes they are named with the same index [39]. The position of the points in the reciprocal lattice is identified by the vector

$$\mathbf{r}^*_{hkl} = h\mathbf{a}^* + k\mathbf{b}^* + l\mathbf{c}^* \tag{2.30}$$

The three vector $\mathbf{a}^*$, $\mathbf{b}^*$, $\mathbf{c}^*$ are the lattice parameters of the reciprocal lattice [39]. In addition the module of the vector is the inverse of the inter-planar distance

$$r^*_{hkl} = \frac{1}{d_{hkl}} \tag{2.31}$$

The electron density function of a perfect infinite crystal $\rho(\mathbf{r})$ is the *convolution* (Appendix A.4) of the direct lattice function $L(\mathbf{r})$ and the function $\rho_M(\mathbf{r})$

$$\rho_M(\mathbf{r}) = \sum_{j=1}^{N} \rho_j(\mathbf{r} - \mathbf{r}_j) \tag{2.32}$$

The eq. (2.325) is the mathematical description of the elementary cell content $\rho_j(\mathbf{r} - \mathbf{r}_j)$ is a Dirac delta function and when $\mathbf{r} = \mathbf{r}_j$ the function is equal to the electron density of the j-th atom in the elementary cell, in the other point of the space is zero. The convolution between the eq. (2.28) and (2.32) has the final expression [39]

$$\rho(\mathbf{r}) = \rho_M(\mathbf{r}) * L(\mathbf{r}) = \sum_{uvw} \rho_M(\mathbf{r} - \mathbf{r}_{uvw}) \tag{2.33}$$

2.5.2 Multi-Scattering Points

In the section 2.4.2 it was described the elastic Thomson scattering by one electron. However, the X-ray diffraction pattern is the result of the interaction among the waves scattered by several scattering points. The Figure 2.15 is the representation of the scattering from two scattering points of O and O'. The versor $\mathbf{s}_0$ indicates

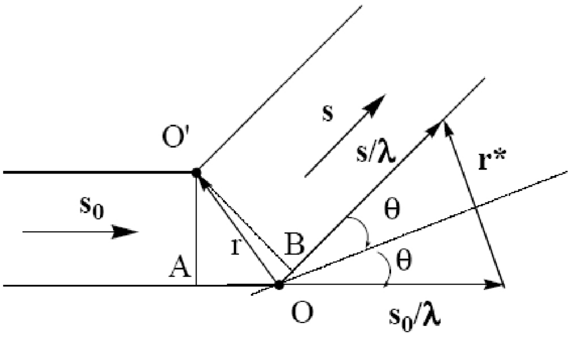

Figure 2.15: O and O' are the two scattering points, $\mathbf{s}_0$ is the incident beam and $\mathbf{s}$ is the scattered vector. λ is the radiation wavelength [39].

the direction of the incident monochromatic X-ray beam of wavelength λ. The versor $\mathbf{s}$ indicates the scattering direction [39]. The phase difference between the waves scattered by the the points O and O' is

$$\delta = \frac{2\pi}{\lambda}(\mathbf{s} - \mathbf{s}_0) = 2\pi\mathbf{r}^*\mathbf{r} \tag{2.34}$$

According to the representation in Figure 2.15, the vector is

$$\mathbf{r}^* = \frac{(\mathbf{s} - \mathbf{s}_0)}{\lambda} \tag{2.35}$$

Since $\mathbf{s}$ and $\mathbf{s}_0$ are unit vectors, the module of $\mathbf{r}^*$ is

$$r^* = \frac{2\sin\theta}{\lambda} \tag{2.36}$$

For each chemical element there is a characteristic value of *scattering factor* f_j which is calculated using the intensity of the scattered wave by the chemical element I_e and the intensity of the scattered wave by a free electron I_{eTh} eq.(2.26)

$$f^2 = \frac{I_e}{I_{eTh}} \tag{2.37}$$

The scattering factors of the elements place in O and O' are f_O and $f_{O'}$. If the phase of the wave scattered by O is zero, [39] the scattered wave formula will be

$$f_{tot} = f_O + f_{O'}exp(2\pi i\mathbf{r}^*\mathbf{r}) \tag{2.38}$$

In general when there are N scattering points the scattered wave is

$$F(\mathbf{r}^*) = \sum_{j=1}^{N} f_j exp(2\pi i\mathbf{r}^*\mathbf{r}) \tag{2.39}$$

where the index j represents the scattering point. However, the scattering points of a crystal are distributed in an ordered geometry so their numbers can be represented by the product of density $\rho(\mathbf{r})$ times the volume d$\mathbf{r}$. Furthermore, for an infinite crystal the summation can be substitute with the integral so the eq.(2.39) becomes the eq. (2.40) whose expression is similar to the Fourier transform of the density [39]

$$F_\infty(\mathbf{r}^*) = \int_S \rho(\mathbf{r})exp(2\pi i\mathbf{r}^*\mathbf{r})\mathrm{d}\mathbf{r} = T[\rho(\mathbf{r})] \tag{2.40}$$

$F_\infty(\mathbf{r}^*)$ is the *structure factor*, the amplitude of the scatted wave which brings information about the electron density function. It is a complex number whose trigonometric form is $F_\infty(\mathbf{r}^*) = |F_\infty(\mathbf{r}^*)|exp(i\varphi_{hkl})$. Unfortunately the detectors in laboratory can measure the intensity of the scattered wave that is proportional $|F(\mathbf{r}^*)|^2$. Therefore, all the information about the phase are lost and the electron density function cannot be calculated directly by a simple anti-Fourier transform of the structure factor. Different mathematical approaches are necessary, but those methods are not reported in the thesis because they are not a part of the topic [39].

2.5.3 Laue and Bragg Diffraction

According to the mathematical property of the convolution and the Fourier transform of the eq. (2.40) is

$$F(\mathbf{r}^*) = F_M(\mathbf{r}^*)\frac{\sum\limits_{h,k,l=-\infty}^{+\infty} \delta(\mathbf{r}^* - \mathbf{r}^*_{hkl})}{V} \tag{2.41}$$

where F_M is the structure factor of the elementary cell meanwhile the rest of the equation is the final result of the eq. (2.29). The presence of the Dirac delta function implies the discontinuity of the diffraction. The intensity is different from zero only when $\mathbf{r}^* = \mathbf{r}^*_{hkl}$, that happens only when the *Laue conditions* are simultaneously respected [39]. This condition consist of a system of equations obtained by the dot product of the eq. (2.38) and the vector $\mathbf{a}$, $\mathbf{b}$ and $\mathbf{c}$,

$$\begin{cases} \mathbf{a}(\mathbf{s}-\mathbf{s}_0) = h\lambda \\ \mathbf{b}(\mathbf{s}-\mathbf{s}_0) = k\lambda \\ \mathbf{c}(\mathbf{s}-\mathbf{s}_0) = l\lambda \end{cases} \tag{2.42}$$

The infinite perfect crystal is a mathematical model that simplifies the calculation. A real crystal has limited size and has defects, the surface of the crystal is also considered as defect, because the repetition geometry is interrupted, causing a reorganization of the atom and the bonding very different from the internal bulk structure. The electron density function of real crystal $\rho_{cr}(\mathbf{r})$ is defined using the *form function* $\Phi(\mathbf{r})$ [39],

$$\Phi(\mathbf{r}) = \begin{cases} 1, & \text{if } \mathbf{r} \text{ is inside the volume} \\ 0, & \text{if } \mathbf{r} \text{ is outside the volume} \end{cases} \tag{2.43}$$

$$\rho_{cr}(\mathbf{r}) = \rho(\mathbf{r})\Phi(\mathbf{r}) \tag{2.44}$$

Thus the structure factor of a real crystal is

$$F_{cr}(\mathbf{r}^*) = \frac{F_{hkl}}{V} \sum_{h,k,l} D(\mathbf{r}^* - \mathbf{r}^*_{hkl}) \tag{2.45}$$

$D(\mathbf{r}^* - \mathbf{r}^*_{hkl})$ is the Fourier transform of the form function of the crystal centered on each point of the reciprocal lattice.

Laue made a rigorous mathematical description of the diffraction and besides Bragg proposed a diffraction model, which is a geometrical simplification. The Bragg's model is physically wrong because it describes the diffraction as discrete reflections. According to Bragg description, if the incident X-ray beam forms an angle θ_B with the crystallographic plane (hkl) it is reflected. The mathematical expression is the *Bragg law*

$$2d_{hkl} \sin\theta_B = n\lambda \tag{2.46}$$

However the Bragg law cannot predict the intensity of the reflected beam.

2.5.4 The Ewald's Sphere

The correlation between the reciprocal lattice and the diffraction pattern is clear using the geometric model of the *Ewald's sphere* (Figure 2.16). A single crystal at the center of the sphere is irradiated by a monochromatic X-ray beam, whose wave length is λ. The radius of the sphere is $1/\lambda$, and the origin of the reciprocal lattice, the node (000), as shown in Figure 2.16 is located on the surface along the direction of the incidence beam [39]. If the a crystal is rotated, consequently, also the reciprocal lattice rotates. If, during the rotation, a node (hkl) of the reciprocal lattice intercepts the Ewald's sphere, the beam is scattered, because in that moment the family of crystallographic planes (hkl) forms the Bragg angle with the direction of the incident beam. The node (000) of the reciprocal lattice is the only one that rotates on itself without moving from its position. In the origin of the reciprocal lattice is centred the *limit sphere* whose radius is $\frac{2}{\lambda}$. The nodes of the reciprocal lattice located outside the limit sphere can not touch the Ewald's sphere during the rotation so they will be never in the Bragg condition. The radius of the limit sphere becomes a discriminating limit because it excludes all the nodes of the reciprocal lattice whose $|\mathbf{r}^*_{hkl}| > \frac{2}{\lambda}$. Those nodes correspond to crystallographic plane whose $d_{hkl} < \frac{\lambda}{2}$. In order to include more node it is necessary to chose a short wave length [39].

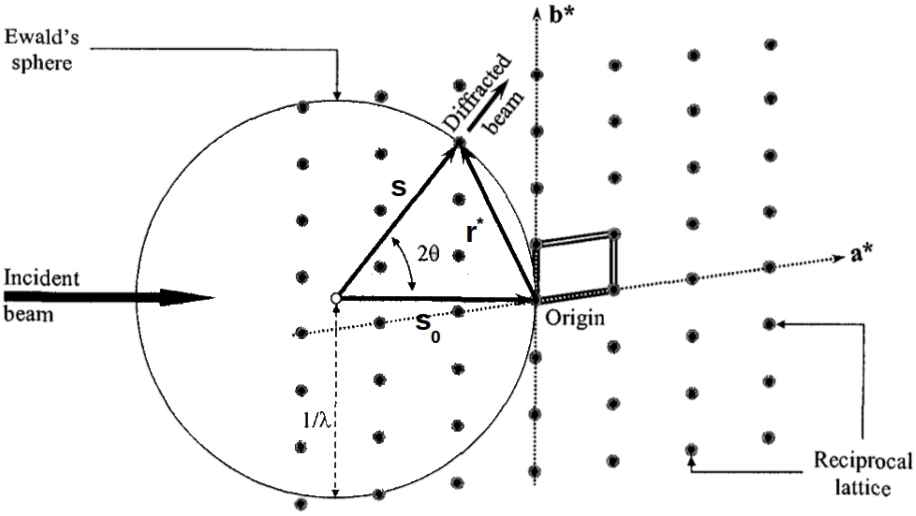

Figure 2.16: Ewald's sphere scheme. The single crystal is in the center of the sphere. The black dots represent the nodes of the reciprocal lattice [42].

2.5.5 Powder Diffraction

Some materials are naturally composed of multi-crystalline domains in the range size of a few micrometers. With the modern technology it is possible to create materials in the range of nanometer. Such materials looks like a powder, in a small volume there is a huge quantity of small crystals. When they are irradiated, they scatter the beam simultaneously. In most cases the small crystals have random orientation and it is not necessary to rotate the sample as the reciprocal lattices associated to each crystals then are random distributed as well. As consequence, the node symmetrically equal lay on the Ewald's sphere, forming a circle perpendicular to the direction of the incident beam, when they are in Bragg reflection condition [42].

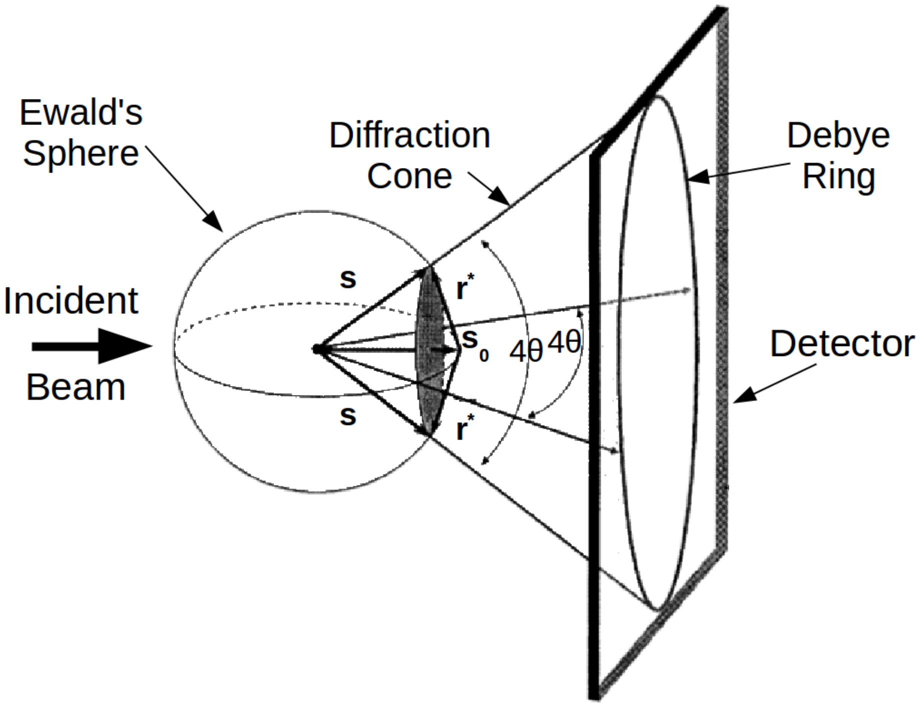

Figure 2.17: Representation of the Ewald's sphere for the powder diffraction with the projection of the Debye ring on the detector [42]

Figure 2.17 shows the schematic representation of the Ewald's sphere in the case of the powder diffraction. The scattering vectors form a cone with the circle, whose angle is 4θ. The detector measures the projection of the cone which is called *Debye* *ring.* In addition, Figure 2.18 shows all the rings of the diffraction pattern.

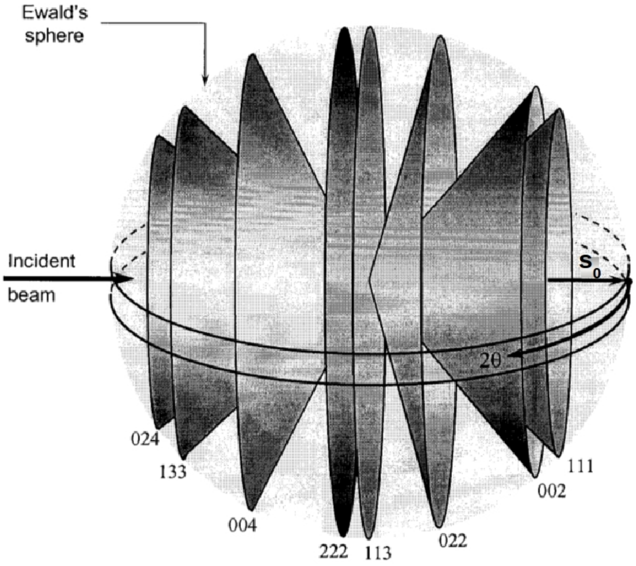

Figure 2.18: Representation of scattering vectors forming cones with relative Miller index. The sample is a copper powder [42].

The signal is integrated along the ring giving the value of the intensity which is plotted as function of the 2θ angle like in Figure 2.19. In this kind of representation the position of the peak is wave length dependent, according to the Bragg's law (eq. (2.49)). The peak positions could be also represented as function of the d-value, in this case the position depends only from the geometry of the crystal and not from the wave length used for the measurement.

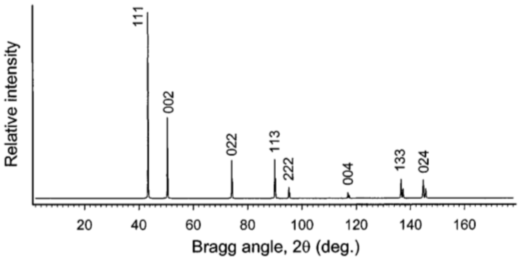

Figure 2.19: Diffraction pattern of a copper powder measured with $Cu_{K\alpha} = 1.54\mathring{A}$ [42]

2.5.6 The Peak Broadness

The peak shape of the diffraction pattern can be fitted with a *Pseudo-Voigt distribution function*, which is a linear combination of two distribution function: the *Gaussian* and the *Lorentzian* [42]

$$I(x) = \eta \frac{C_G^{1/2}}{\pi^{1/2} H} exp(-C_G x^2) + (1-\eta) \frac{C_L^{1/2}}{\pi H} (1 + C_L x^2)^{-1} \tag{2.47}$$

where:

- H is the full widths at half maximum (FWHM) calculated by the Cagliotti formula: $H = (U \tan^2\theta + V \tan\theta + W)^{1/2}$, U, V, W are free variables;
- η is the mixing parameter for the linear combination of the Gauss and Lorentz Function
- $C_G = 4ln2$, and $\frac{C_G^{1/2}}{\sqrt{\pi}H}$ is the normalized factor for the Gaussian distribution;
- $C_L = 4$ and $\frac{C_L^{1/2}}{\pi H}$ is the normalized factor for the Lorentzian distribution [42]

The real shape of peak cannot be approximated only by a Gaussian or only by a Lorentzian distribution because as illustrated in Figure 2.20

the Gaussian distribution has rounded maximum and no tails at the base while the Lorentz distribution has long tails on both sides and it is sharp close to the maximum. When a datum is fitted and a FWHM is calculated it is possible to correlate it to the size of the crystal. In fact the shape of the peak is due to the contribution of the crystal size and shape and other parameter sand the *Peak Shape Function* (PSF) is their mathematical convolution

$$PSF(\theta) = \Omega(\theta) * \Delta(\theta) * \Psi(\theta) + b(\theta) \tag{2.48}$$

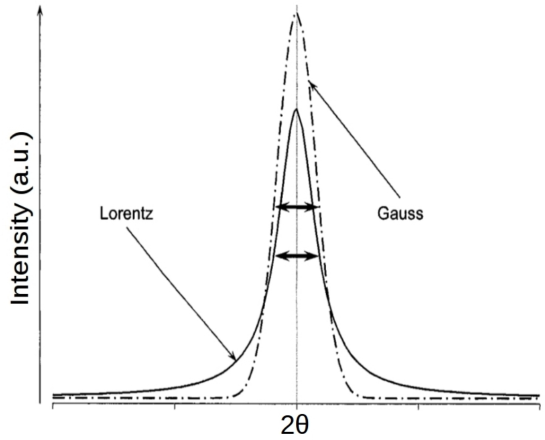

Figure 2.20: Gaussian and Lorentzian peak profiles [42]

where $\Omega(\theta)$ is the is the instrumental broadening that depends on the geometrical parameter of the setup, $\Delta(\theta)$ is the wave length dispersion and it depends of characteristic of the X-ray source, $\Psi(\theta)$ is the sample function, $b(\theta)$ is the background function, influenced by X-ray fluorescence emitted by the sample or X-ray scattering of the air [42].

The contribution of the instrument and the X-ray source to the peak broadening is calculated fitting the diffraction profile of a standard sample. Therefore, the average size distribution of the crystals τ is calculated by the so called *Sherrer formula* [43]

$$\tau = \frac{0.9\lambda}{\sqrt{(H_m^2 - H_s^2)}\cos\theta_B} \tag{2.49}$$

where H_s and H_m are the FWHM of the diffracted peak of the standard and of the sample, respectively [43].

2.5.7 Phase Identification

The powder diffraction pattern is the *finger print* of the crystal. The position of the peaks depends on the geometry and the intensity regarding the chemical elements, therefore each crystallographic phase has an unique diffraction pattern.

Since the beginning of the X-ray crystallography, it was clear the potentiality of this analytical technique for the crystalline phase identification. For instance graphite and diamond are two allotropic crystal structures of carbon. Although they have the same chemical composition the atom are arranged in different geometry: the graphite is an hexagonal crystal while the diamond is cubic.

The diffraction patterns of the pure crystal phase are piled in databases and measured diffraction patterns are identified by the database through a match with the peak positions and peak relative intensities. The first database was printed on paper in 1938 by J. D. Hanawalt. Nowadays the database pile a number of crystals diffraction information and are available on-line or on CD-room, available for free or on sale. The most used one is the commercial *PDF2* by JCDPS. The *American Mineralogist Crystal Structure Database*, a freed database available on line, was used for the identification of the crystal phases used during the experimental work of this thesis [44].

2.6 Small Angle X-ray Scattering

During the SAXS measurement the sample is irradiate with a coherent X-ray beam. The technique operate in transmission mode. A vacuum tube with windows made of X-ray transparent materiel is located between the sample and the detector. The transmitted beam passes through the vacuum tube to avoid further scattering contribution due to the atmospheric gases [40]. The intensity is measured and plotted in the intensity *vs.* the scattering vector module q which is correlated to the particle distance and to the wavelength of the radiation

$$q = 2r^* = \frac{2\pi}{d} = \frac{4\pi \sin\theta}{\lambda} \tag{2.50}$$

At the small angle for SAXS the precise information about the relative positions of the atoms is lost because the resolution is not enough, vice versa for WAXS. In this system using a vector with its direction is not required but only the modules is important [45]. Only the coherent scattered beam is useful for the analysis of the sample, meanwhile the incoherent scattered beam is contributes to the noise of the signal. Furthermore, the atoms of the sample produce a constant scattering at small angle that contributes to the background of the signal. The sample can contain different material domains, different states (solid, liquid and gas) and different concentrations, the sensibility to estimate the concentrations of a compound is from $0.1wt\%$ to $99.9wt\%$. SAXS can be applied for the analysis of different typology of samples such as [40]:

- biological and food
- chemical and pharmaceutical
- nano-material
- polymer and compose materials
- mineral
- crystalline and amorphous materials

The signal is an average measure of all the element inside the irradiated volume. However when the detector record the signal, it loses the information about the phase of the wave, like it happens for the WAXS, a mathematical modelling approach is employed to determine the particle size, shape and structure of the sample. The average signal arises from the electron dense part of the sample and it is also influenced by the electron density difference between the particles and matrix contrast. In fact, materials made of high-atomic-number elements dispersed in matrix composed of low-atomic number are better detected. For this reason the matrix should not be made of heavy element. The following equation is the mathematical definition of the *scattering length*

$$f_{object}(\mathbf{q}) = \int exp(i\mathbf{q}\mathbf{r})\rho_{object}(\mathbf{r})\mathrm{d}\mathbf{r} \tag{2.51}$$

which is calculated as the Fourier transform of the electron density of the scattering object $\rho_{object}(\mathbf{r})$. The scattering length is the analogue of the scattering factor (eq. (2.37)) for the WAXS, and the measured intensity of the signal is the product of

$f(\mathbf{q})$ times its complex conjugate $f^*(\mathbf{q})$ [45]

$$I(\mathbf{q}) = f(\mathbf{q})f^*(\mathbf{q}) = \int\int exp[-i\mathbf{q}(\mathbf{r}_1 - \mathbf{r}_2)]\rho(\mathbf{r}_2)\rho(\mathbf{r}_1)\mathrm{d}\mathbf{r}_1\mathrm{d}\mathbf{r}_2 \tag{2.52}$$

The equation of the intensity is very complicated, but with the condition in the list the equation can be simplified:

1. the system is isotropic
2. the sample is diluted
3. in the system there is no long-range order

(1)As consequence of the first condition the vector $\mathbf{r}_{ij} = \mathbf{r}_i - \mathbf{r}_j$ has a constant module but a random direction. (2) In the Figure 2.21 there is a representation of three particles in a matrix separated by the distance r_{ij}. If $r_{ij} >> \lambda$, the system is diluted, so there is no interaction between the scattered beams [45].

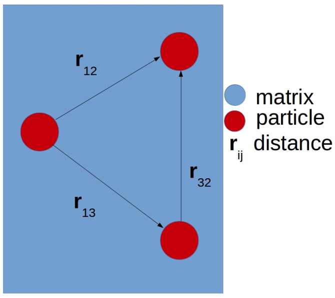

Figure 2.21: Particle in the matrix with the distance of $\mathbf{r}_{ij}$

(3) The system is not discrete when the scattering objects are particles and not isolated atoms, and those particles are distributed without any specific distribution. It could be happen that at short range there is a low order distribution due to the interaction among one particle and its close neighbour, but after there is no order [45]. So the previous equation becomes

$$I(q) = 4\pi \int r^2 \frac{\sin(qr)}{qr} \overline{\rho}^2(r)\mathrm{d}r \tag{2.53}$$

Where all the variables are the module of the vectors and $\overline{\rho}^2(r)$ is the autocorrelation of the electron density. If the scattering objects are spheres of radius R whose electron density is constant, the function of $\overline{\rho}^2(r)$ can be put out of the integral and the integration of the other functions become the *Rayleigh function* [45]

$$P(q) = P_{sphere}(q, R) = [\frac{3(\sin qR - qR\cos qR)}{(qR)^3}]^2 \tag{2.54}$$

The profile of the function of $P(q)$ is reported in Figure 2.22 for different R value, it has well defined zeros at $qR = 4.493$, $= 7.725$ and so on, that can be used to calculate R. The function of $P(q)$ is the *form factor*.

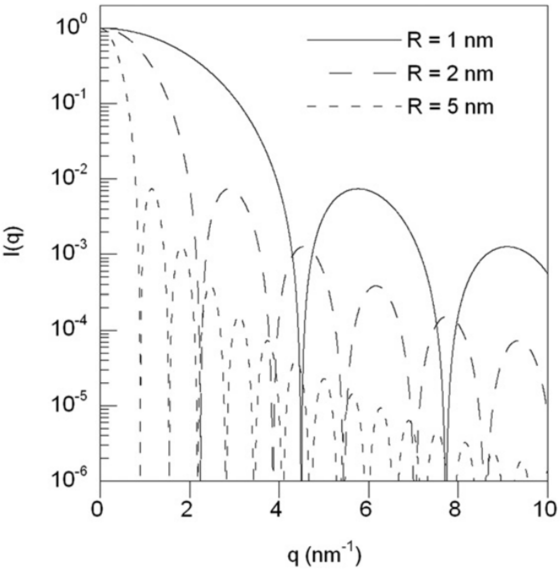

Figure 2.22: Rayleigh function as form factor for different R-value [45]

2.6.1 The Form Factor

The SAXS analysis is modelling dependent and several factors are involved for solving the computational part of the problem. When the system is so diluted to avoid the interaction between the particles, as in the case of the eq. (2.54), the detector measures an interference pattern that oscillates in a characteristic fashion particle shape dependent [45]. The *form factor* is the part of the model related to the particle shape. The analytical formula for the solution of the integral was solved for particle sphere, disk and cylinder shape as reported in Figure 2.23.

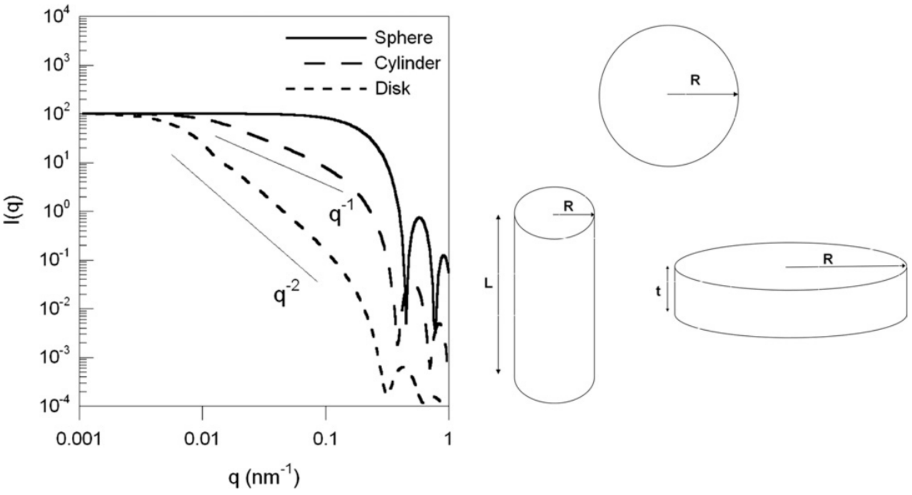

Figure 2.23: Simulated form factors for different particles shape: (continuous line) sphere with $R = 10nm$; (dash curve with long line segment) cylinder with $R = 10nm$ and $L = 300nm$; (dash curve with short line segment) disk with $t = 20nm$ and $R = 300nm$. Representation of geometrical shapes is reported on the left for clarity [45]

However, in same case it is not possible to find an analytical solution of the integral eq.(2.52). Therefore the equation of the intensity is rewritten including the the experimental parameters [45]

$$I(q) = \frac{N}{V}\frac{d\sigma}{d\Omega} = NV^2\Delta\rho^2 P(q)S(q) \tag{2.55}$$

where

- $d\sigma$ is the fraction of transmitted beam calculated as ratio between the number of scattered over the number of incident photons.

- $d\Omega$ is the solid angle of the detector

- V is the irradiated volume

- N is the number of particle inside the volume V

- $\Delta\rho$ is the difference of electron density between the the particle and the matrix

- $S(q)$ is the *structure factor*

The difference in electron density is also a measure of the contrast between the matrix and the particles. According to this equation the scattering intensity is directly proportional to the square of it [45]. If the matrix and particles have the same electron densities the intensity will be very low and maybe the particles could not detected.

2.6.2 The Structure Factor

In the case of the powder diffraction each crystal scatters the beam independently, instead in the small angle the scattered beam of each particle can be influenced by the other scattered beam. After the form factor the *structure factor* $S(q)$ is the next parameter that has to be considered in the model. In dilute system $S(q) = 1$, but when the particle are densely compacted all the scattered beams start interacting and an additional interference contribution is developed. A system is not diluted when the distance r_{ij} (Figure 2.21) among the particle is the same order of magnitude of the X-ray wave length. By increasing the concentration of the particle in the matrix, the intensity of the signal will change at low q-value. If there is attractive interaction between the particles the signal tends to become more intense. Otherwise if there is repulsive interaction among the particle, the signal will lose intensity. Analytical expression for the function $S(q)$ are very difficult to calculate. In some case the particles form an ordered assembly, similar to a crystalline lattice, which provides a diffraction peak according to the Bragg law (eq. (2.46)) at low q-value. Furthermore, the symmetry of the assemblies can be identified by using the ratio of the peaks position it is possible to identify the symmetry of the assembly. In the Table 2.5 there is a list of the symmetry and the corresponding peak position ratios are summarized [40].

The particle-particle repulsion brings the system to a short range order: close to the particle there is a certain probability to find the closest neighbour at a specific distance but at large distance there is a random distribution of the particle

Symmetry	Peak Ratio
Lamellar	$1, 2, 3, 4, 5$
Cubic	$1, \sqrt{2}, \sqrt{3}, 2, \sqrt{5}$
Hexagonal	$1, \sqrt{3}, 2, \sqrt{7}, 3$

Table 2.5: Symmetry and peak ratio of ordered assembly [40]

position [45]. In the Figure 2.24 the signals on the detector can look like a ring, semi-ring and dots according to the level of order. The ring is shown on random distributed particles, typical a powder or dispersion. The semi-ring indicates a certain level of orientation typical of the fibre. The dots are the analogue of a single crystal diffraction, which appears in the case of a high level of order. The detector measures also the photon scattered by the matrix but they contribute to the background [40].

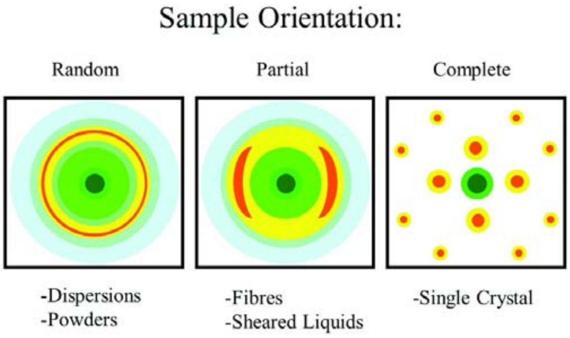

Figure 2.24: The 2D-scattering patterns of randomly oriented (isotropic), partially oriented and perfectly oriented (single crystal) samples [40]

2.6.3 Polydispersivity

The sample could be composed of particles with different shape and size and also the matrix could consist of different materials. For a complicated sample it is noteworthy to explain polydispersivity [40]. The scattering curves become a sum of all the different contributes which does not exhibit any particular shapes in the case of mono-disperse and uniform samples, as previously explained [40]. The mathematical expression of the intensity becomes

$$\Delta I(q) = I_0 \sum_{i=1}^{N} (\Delta\rho)_i^2 V_i^2 P_i(q) \tag{2.56}$$

2.6.4 Profile of the Curve

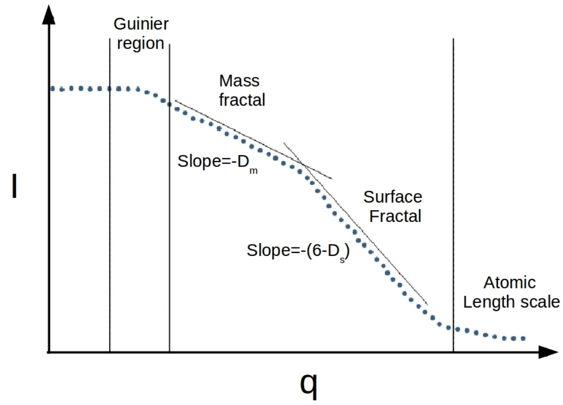

Figure 2.25: Profile of the SAXS curve [46]

Figures 2.22 and 2.23 are limit and ideal cases. When the structure of the sample is more similar to a fractal, a structure that is self-similar at every scale, the SAXS profile is more similar to the schematic representation reported in Figure 2.25 [46]. The graph is divided in different areas (Guinier region, Mass fractal, Surface fractal and Atomic length scattering) and the $LogI(q) - Logq$ plot allows to approximate the curve into right lines. Each slope of the graph can provide different information about the sample [46]. The scattered intensity for a fractal object is

$$I(q) \approx q^{-\alpha} \tag{2.57}$$

The value of α is related to size and shape of the structures:

- Guinier region $\alpha = 4$ dense structure with smooth interface
- mass fractal for $\alpha = D_m$ with $1 < \alpha < 3$
- surface fractal exponents for $3 \leqslant \alpha \leqslant 4$ where $\alpha = 6 - D_s$ D_s is called the surface dimension, with values $2 \leqslant D_S \leqslant 3$

Other two limit case are related to the are of the graph at low and high q-value. Those approximations are called the *Guinier approximation* and the *Porod law* [46].

Guinier approximation

In the case of dilute system ($S(q) = 1$), the part of the curve of the graph at small q-value (Guinier region) can be interpolate by the Guinier approximation. This model is particle shape independent and approximate the intensity

$$I(q) = I(0)exp(-\frac{q^2 R_G^2}{3}) \tag{2.58}$$

R_G is the radius of gyration. However, when the shape of the particles is already known, it can be used to calculate their dimension using different formulas according to the shape of the particle. For example the radius of a homogeneous spherical particle can be calculated by the formula [46]

$$R = \sqrt{\frac{5}{3}} R_G \tag{2.59}$$

The parameter $I(0)$, extrapolated from the curve at $q = 0$ is correlated to the molecular mass M of the scattering object:

$$I(0) = \frac{\overline{\rho} M}{d^2 N_A} (\Delta\rho)^2 V_p^2 \tag{2.60}$$

Porod Law

At high q value (Surface fractal region), when the boundary between the scattering particle and the matrix is sharp and smooth, the intensity function is

$$I(q) = \frac{2\pi(\Delta\rho)^2}{q^2} S_s \tag{2.61}$$

which can be approximate as

$$I(q) \approx q^{-4} \tag{2.62}$$

S_s is the specific surface and it is the ratio between the surface and the volume of the scattering particle [46].

2.7 Theory of Scanning Electron Microscopy

The scanning electron microscopy (SEM) is a technique based on the use of the electrons as light to *illuminate* the sample. The electrons are easily absorbed by the matter and gases. The analysis is performed in a vacuum chamber to allow the electrons to move from the source to the sample, because their mean free path is correlated to the vacuum, the lower the vacuum the longer the path. Thus the SEM requires a good vacuum system without air leakage.

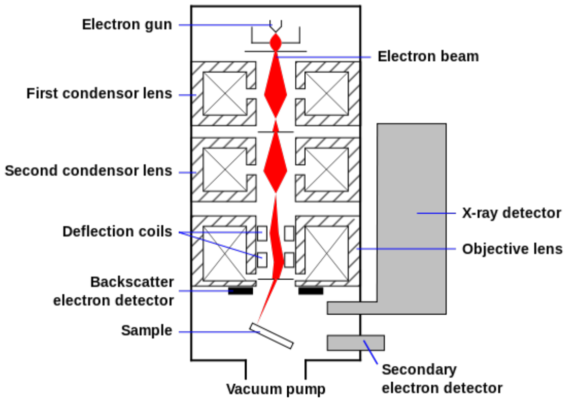

Figure 2.26: A generic scheme of a SEM column. The electron beam (red stripe) is emitted by the electron gun and focused on the sample by the magnetic lens. In this scheme, the column is equipped with three detector for measure X-ray detector, backscattered electron and secondary electron.

In Figure 2.26 the SEM is represented as column, The main component of the microscope are the electron source, so-called *electron gun*, the magnetic lens, different detectors and the vacuum pump. The simplest source of electrons is a tungsten filament heated by the *Joule effect.* When the filament reaches a certain temperature, the surface of the tungsten emits electrons by *thermionic emission* and these electrons are accelerated toward the sample by a bias, forming the electron beam. The thermionic emission J is described by the *Richardson's law*

$$J = AT^2 exp(\frac{-\Phi}{kT}) \tag{2.63}$$

A is the Richradson's constant typical of material, k is the Boltzman constant, Φ is the work function. Tungsten is chosen as source of electron because it is the metal with the highest melting temperature, and also filament of LaB_6 can be used but it is more expensive than tungsten.

The lens are copper coils and they develop a magnetic field proportionally to the current passing inside them. The magnetic field is used to focus the beam on the surface of the sample. The vacuum system usually consists of a rotative pump or membrane pump for the pre-vacuum $10^{-3} mbar$ and a turbo pump to reach the working vacuum condition $10^{-10} mbar$. In the Figure 2.26 three detectors are located in the microscope because the electron-matter interaction provides different signals (Figure 2.27)that can be used for the characterization of the sample. This signal provide morphological and chemical analysis.

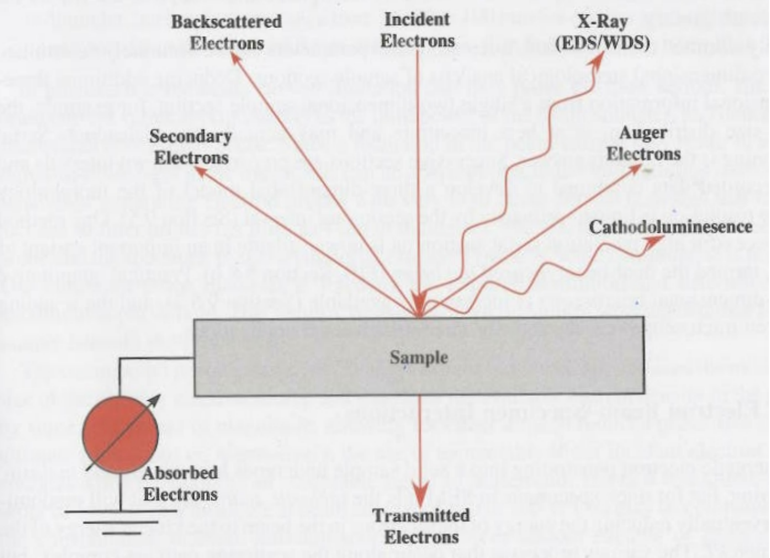

Figure 2.27: Scheme of the electrons and photon emitted by a sample in a SEM when it is irradiated with the electron beam [47].

All the informations collected by a SEM comes from the *interaction volume*, that is the volume under the irradiate surface and it emits [47]

- Backscattered electron (BSE)
- X-ray radiation
- Secondary electron (SE)
- Cathode photoluminescence
- Auger Electron
- Wavelength-dispersive X-ray (WDS)

However, the SEM used for the *ex situ* analysis has the detector for the BSE and the X-ray radiation.

2.7.1 Backscattered Electron

When the electron beam irradiates the sample part of the electrons interact elastically with the surface and they are back-scattered. The elastic back-scattering is more efficient when the surface is composed by a heavy element with a high atomic number. Therefore if the surface is composed by different materials the parts with the heavier element look brighter. This picture gives a preliminary chemical composition of the sample [47].

2.7.2 Analysis of the Emitted X-ray Radiation

When electron is removed from the internal core of an atom due to the electron-electron interaction the atom relocates the electrons in order to fill the hole. During this process an electron moves from the outer shell to the internal core of the electron configuration, emitting an X-ray photon. This phenomenon is similar to the one explained in section 2.4.3 for the X-ray absorption, but in that case X-ray

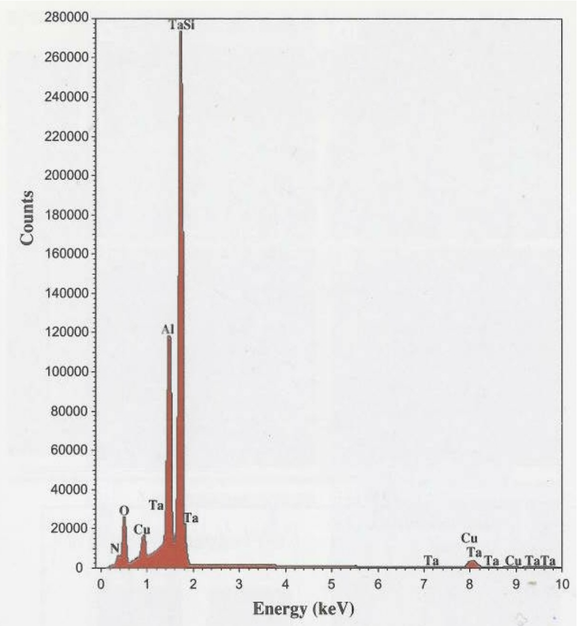

Figure 2.28: EDX measurement of printed circuit board [47]

fluorescence was caused by the X-ray-electron interaction. The electrons of an atom have a specific energy level according to their state. The emission of the X-ray photons is discrete with the specific energy.

The EDX measurement acquisition looks like the Figure 2.28, on the x-axis it is reported the photon energy while on the y-axis it is reported the intensity. Figure 2.28 shows the EDX spectrum of printed circuit board made of silicon, tantalum [47]. In a database the energy values for each chemical element are piled. Therefore, the software for the data analysis can identify. The SEMs can show the picture of the sample with different color that represent the distribution of the element. After the identification of the elements in the sample (elemental analysis), the software can calculate their concentration using algorithm based on the relative intensity of the peak and the interaction cross section between the electrons and the chemical elements [48].

Chapter 3

Experimental Section

3.1 Preparation of Anodes

3.1.1 Ball Milling

Ball milling is a simple technique to grind materials or to make fine powders starting from raw precursors. In the current project a planetary ball mill of the type *Pulveisette 7 Micro Mill* (P7) (Figure 3.1) has been used on the starting material of *a-P/C*.

The machine consists of an engine, two jars and balls. The planetary ball mill has an engine that transmits a horizontal and circular movement to two jars around a central axis meanwhile the jars rotate on their axis. The jars and balls are made of stainless steel. They have to be made of the same material or materials with the same hardness, otherwise the harder material will destroy the softer material during the impact and the powder of the softer one will contaminates the final product. The jars have caps with a rubber o-ring in order to keep the inert atmosphere after closing the jar in a glovebox.

Figure 3.1: Pulveisette 7 Micro Mill (P7)

The balls to powder weight ratio is an important parameter for the energy development during the impacts. This ratio is significantly high, the energy impact increases leading to solid state reactions or reducing the particle size. However, in the P7 it is mandatory to put at least 1g of powder because the impacts of the balls could be energetic enough to damage them and introduce contaminant onto the milled powder. On the contrary, when the powder quantity is large, the powder can slow down the movement of the balls.

3.1.2 Preparation of the Anode Made of *a-P/C*

The raw materials were stored and handled in a glovebox filled with argon (Ar) gas, as well as the jars. The active material for the fabrication of the anode was made by mixing red phosphor purchased by Sigma Aldrich and amorphous carbon SuperP purchased by Timcal Graphite and Carbon in a weight ratio of 7:3. 1g of this mixture was put with five balls of 4g each, with a ball to powder ratio of 20:1.

Ball milling was carried out at $750RPM$ for $24h$. The mill grained the materials up to a nanometer scale,in the following called the *a-P/C*. There were prepared two different slurries one for the characterization of the *in-house* built cell and one for the experiments at the synchrotron.

Anode for the Characterization of the ***In-House*** built cell

A slurry was prepared by mixing $70wt\%$ of *a-P/C* with $10wt\%$ of a conductive material and $20wt\%$ of binder polymer. The conductive material was the same carbon SuperP used for the preparation of the *a-P/C*. The binder was poly acrylic acid (PAA). All the powder were put together in a $2ml$ vial with fifty drops of ethanol and one glass ball. The vial was sealed and put in the vortex at $3000RPM$ for $2h$ to obtain an homogeneous mixture. An aluminium foil was put on a flat glass surface with few drops of water between the foil and the glass tape. The liquid tension pull the aluminium foil toward the glass and rubbing a paper tissue on the aluminium it was possible to obtain a complete flat metal surface. Then the said of the metal foil, that will be in contact with the active material, was also acetone washed. The vial was unsealed and its aperture was put directly in contact with the metal foil. The glass ball limited the leakage of the slurry. The slurry was roughly spread moving the vial along the foil surface.This procedure is similar to write with a ballpoint pen. The slurry was uniformly manually spread on the aluminium foil with a metal blade. Finally, the tape was dried in oven at $60°C$ for $12h$ in air. This anode was prepared for the electrochemical comparison of the coin cell and the *in-house* built cell because it is easy to dilute the PAA in ethanol, therefore the slurry remain easily attached to the foil. However, PAA is potentially carcinogenic.

Anode for the Experiments at the ESRF

A slurry was prepared by mixing $80wt\%$ of *a-P/C*, $10wt\%$ of Carbon SuperP and $10wt\%$ of binder. The binder was a mixture 1:1 in weight of sodium carbomethyl cellulose (CMC) with two different mass average molar mass (Mw). They had $Mw = 250000$ and $Mw = 700000$,respectively, and both were purchased by Sigma Aldrich. All the powders were mixed together in a $2ml$ vial with forty drops of

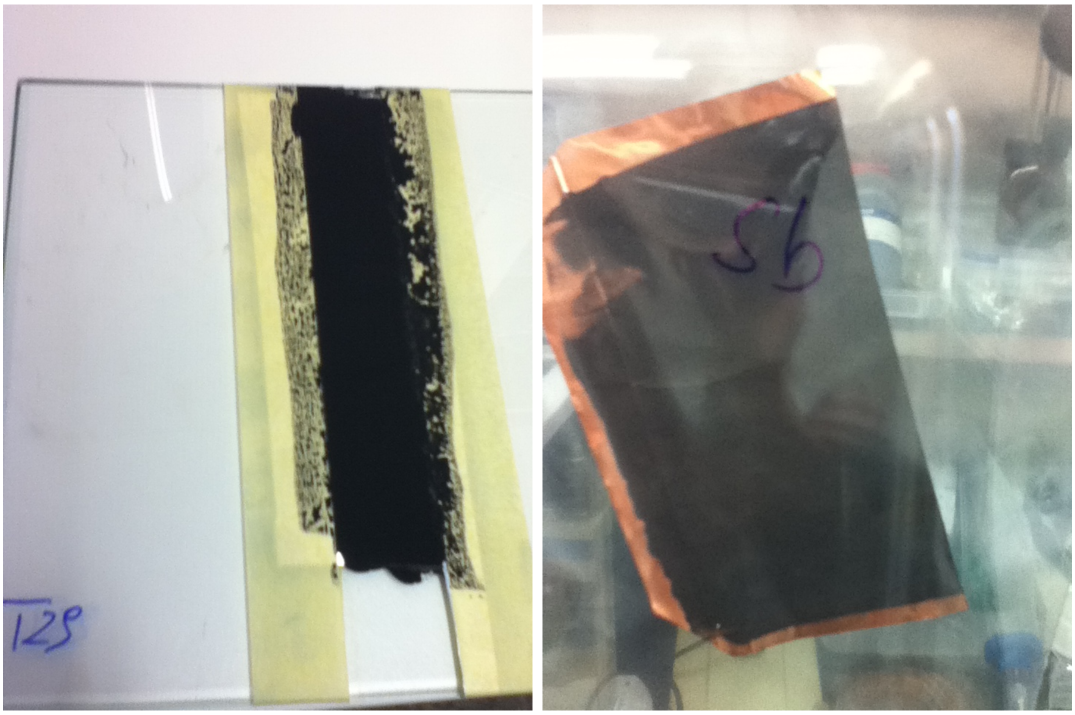

Figure 3.2: Left: Anode made of *a-P/C* tape T29, Right: Anode made of $FeSb_2$

water and one glass ball. The vials was seal and put in the vortex at $3000RPM$ for $2h$. The preparation of the aluminium foil was the same as in the previous case except for the fact that the aluminium was methanol washed. The slurry was spread on the aluminium foil by the same procedure explained before, and than dried in oven at $60°C$ for $12h$ in air. The *in situ* cell for the experiment was assembled using the tape number 29 (T29). Figure 3.2 left it is reported the picture of the tape T29 after the drying process. The dilution of the CMC in water is more difficult compare tot the dilution of the PAA in ethanol. However, we wanted to give our contribution to the study of a more environmental friendly battery, since CMC is non-carcinogenic.

3.1.3 Preparation of the Anode Made of $FeSb_2$

An anode with $FeSb_2$ as active material has also been prepared. The synthesis of the $FeSb_2$ and the preparation of the tape has been done by the group of dr. D. Zitoun [6].

A stoichiometric quantity of iron and antimony 1:2 was placed in a silica tube sealed under vacuum. The tube was heated with a ramp of $2°Cmin^{-1}$ up to $730°C$. The heating process was four days long, at the end of the process the tube was air quenched, and the final product was the $FeSb_2$ with space group $Pnn2$.

The conductive material was a mixture 1:1 weight of carbon black and vapour ground carbon fibre. The binder was CMC with ($Mw = 250000$) purchased from Sigma Aldrich company. The slurry was prepared diluting in water a mixture of $70wt\%$ of active material, $12wt\%$ of binder and $18wt\%$ carbon superP. The slurry was put in a planetary ball mill for $1h$. The slurry was spread on a $20\mu m$ tick copper foil and dried at room temperature for $12h$ and then dried for other $2h$ at $100°C$ in vacuum. The final result can be seen in Figure 3.2 (right)

3.2 Cell Assembly

3.2.1 Anode Cutting

The as-prepared tape was put between paper sheets to avoid contamination, and laid down on a flat piece of plastic and cut with a round cutter. Also a disk of a clean metal foil was cut with the same cutter to be used to estimate the quantity of powder on the anode by weighing the two disks with a four decimal digit analytical balance. The quantity of the active material was calculated by multiplying the value of the powder mass and the weight percentage of the compound in the slurry. $8mm$ and $16mm$ diameter disks were cut for the assembly of the coin cell and the *in-house* built cell, respectively.

3.2.2 Electrolyte Solutions

The electrolyte solutions were made of ethylene carbonate (EC), diethylen carbonile (DEC), fluoro-ethylene carbonate (FEC), as solvents, and $NaPF_6$, as a salt. All chemicals were purchased from Sigma Aldrich. The list and the composition of the electrolytes were:

- Electrolyte 1: $1M$ in $NaPF_6$ EC:DEC ($1:1wt$) + $5wt\%$ of FEC
- Electrolyte 2: $1M$ in $NaPF_6$ EC:DEC ($1:1wt$)

3.2.3 Coin Cells

To test the anodes before being used to our in-house built cell, standard 2032 coin cells, purchased from *Pi-KEM LTD*, were used. The components of the coin cell are showed in Figure 3.3. They consists of two electric contacts also acting as the external case of the cell, one spacer, one spring, the glass fibre layers and the anode. The coin cells were assembled in the glovebox by spreading metallic sodium directly on the stainless steel spacer acting as an electron collector (cathode). Anode and cathode were separated by two layers of glass fibre, soaked with $60\mu l$ of different electrolyte solutions, to avoid internal short circuit. The round spring push the components in the correct position and guarantees electric contact between the cathode and the external parts of the coin cell. The coin cell was sealed by using an *EQ-MT-160D* press of MTI Corporation (Figure 3.4) and then taken out from the glovebox.

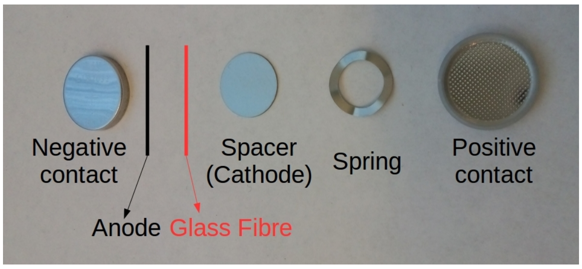

Figure 3.3: Components of a coin cell

Figure 3.4: EQ-MT-160D machine crimping in the glovebox

3.2.4 Assembly of the *In-House* Cell for *In Situ Operando* Measurements

For the *operando* measurement we used an *in-house* cell designed and built at the chemistry department of University of Oslo. Figure 3.5 shows two assembled cells (left, right) observed in different directions and one disassembled cell (middle).

The cell consists of two concentric tubes of the external and internal parts made of brass and teflon, respectively. A small circular piece of teflon covers one of the ending part of the brass tube. The tube is closed by two metallic nuts (A, F). There are three kapton windows on components A, D and E. The teflon is chemically inert and electrically insulate, while the kapton windows are X-ray transparent. When the cell is assembled the components of C and D are positioned inside the teflon tube. Metallic sodium is spread directly on the full area of the kapton window of the small metallic tube (D) until the sodium is in contact with the metal part of the same tube. The clean side of the anode disk is in contact with the kapton polymer window and the metal of the component E, while the other side of the disk with the active material touches the spacer. The anode and cathode are separated by the spacer layers. The two small metallic components (C) push the component D toward the component E and provide the electric contact between the cathode and the small metal ring around the kapton window of the nut A. When the cell is assembled the two poles are the small metal ring on the nut A and the rest of the

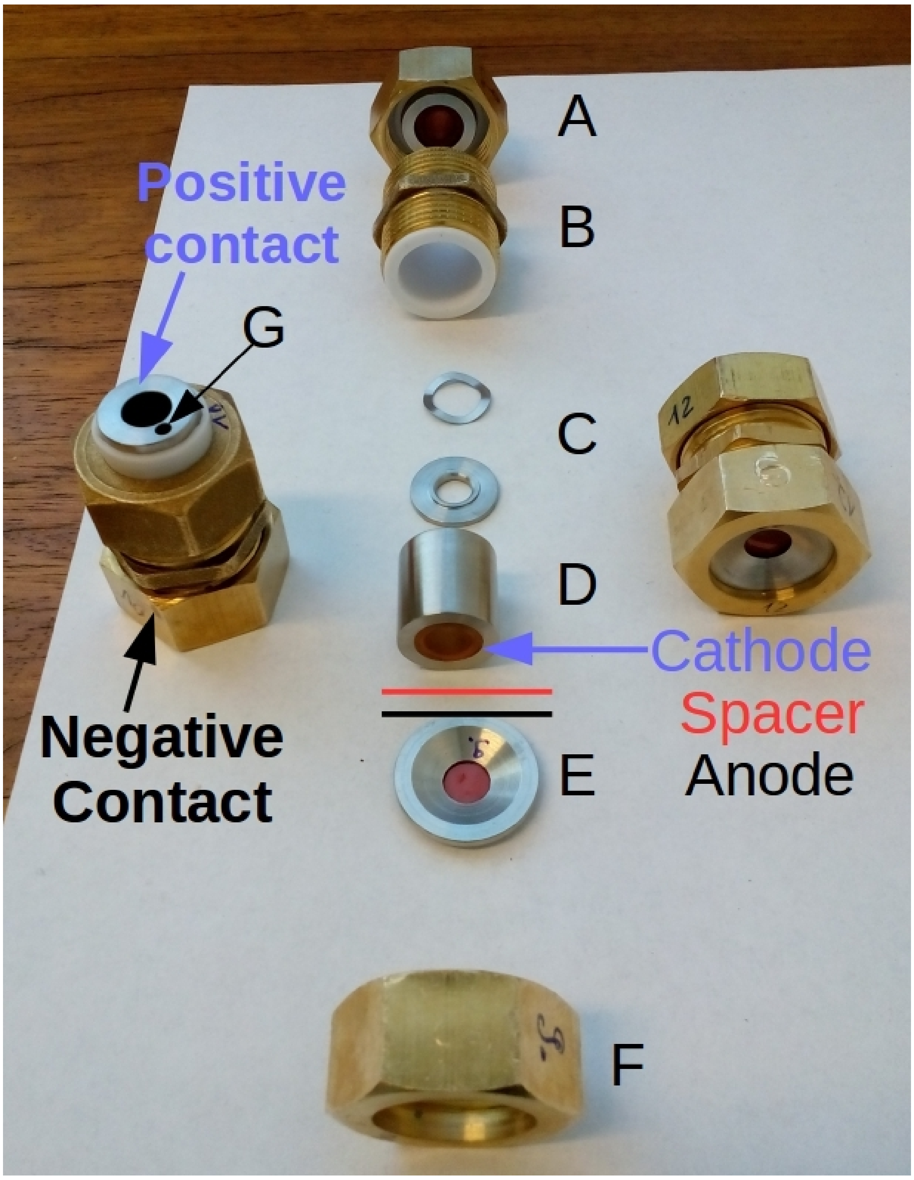

Figure 3.5: Cells for *in situ operando* measurements: (left, right) two assembled cells observed in different directions and (middle) a disassembled cell. A) and F) are the brass nut that close the cell. B) is the two concentric tubes made of brass (external) and teflon (internal). C) is two small metallic components that push the element D) and E) in position. D) is the electron collector of the cathode. The metal sodium is spread directly on the kapton (brown) window. The space between the D) and E) is filled with the spacer layers and the anode. The electrochemical active part of the cell is built between the component E) and C). E) is the electron collector of the anode. When the cell is assembled the brass component are equipotential with the component E)(negative contact). The positive contact is indicated by the blue arrow. G) is the spine hole for the electric connection with the galvanostat.

external metal case that is equipotential with the component E. In this specific case the external part is the negative contact and the small ring is the positive contact. If the cell is used to study cathode materials the polarity is inverted.

The anode of *a-P/C* and the cathode were separated by two layers of glass fibre soaked with $100 \mu l$ of Electrolyte 1.

The anode of $FeSb_2$, and the cathode were separated by two drilled layers of glass fibre and one layer of celgard membrane. Those spacer layers were soaked with $100 \mu l$ of Electrolyte 2.

The spacer layers are different for the two cells because copper adsorbs more X-ray than aluminium does, and furthermore the copper foil was also thicker than the aluminium foil. The glass fibre was drilled to reduce the quantity of the material along the X-ray beam path.

Other two cells without the active materials were similarly prepared as described above. In the position of the anodes there were clean disks of the same copper foil and the same aluminium foil used as electron collector for the preparation of the active anodes. The two cells without active materials were exposed to the synchrotron X-ray beam in order to collect their WAXS and SAXS profile to be used for background extraction for the analysis of the two cells made with the active materials. In the data analysis of the chapter 4 those profile are called *blank*.

3.3 Galvanostat

The BatSMALL galvanostat of Astrol Electronic AG was used to perform the electrochemical characterization of the cells. Table 3.1 summarizes the specification for the measurements with their range and resolution according to the data sheets. All the experiments were carried out in the current and voltage range $\pm 5mA$ and $\pm 10V$.

Specification	Range	Resolution
Current Measurement	$\pm 5mA$	$150nA$
-	$\pm 10mA$	$300nA$
-	$\pm 20mA$	$600nA$
-	$\pm 40mA$	$1200nA$
Current Output	$\pm 17mA$	$8.5\mu A$
Voltage Measurement	$\pm 10V$	$300\mu V$

Table 3.1: Specification of the measurement parameter of the BatSMALL galvanostat

The BattSMALL galvanostat is connected to a computer (left side in Figure 3.6) that controls the machine by the *CCCC.exe* software, while the measurement are programmed by the *CCCCtools.exe* software. The second software needs two inputs: one is the estimated weight of the active material for the calculation of the specific capacity and the other is the potential window ranging the voltages related to the sodiation and the de-sodiation. During the experiments the potential window was $2V - 10mV$, which means that the negative current was applied until the potential reached $U < 10mV$, instead the positive current was applied until the potential reached $U > 2V$.

The cells were connected to the BattSMALL galvanostat by two cables in order to close the circuit. The red cable is connected to the cathode and the black one to the anode as showed in the right side of Figure 3.6. The coin cells were placed in a commercial holder. The holder, for the *operando* measurements, consists of two concentric tubes: an internal one made of metal in contact with the cell and an external one made of plastic (in dark gray in Figure 3.6) for the electrical insulation. The electrical connection between the cell and the BattSMALL is established by two cables: one is inserted inside the spine hole of the nut A (in position G of Figure 3.5), the second is connected to the screw in contact with the internal metal tube of the holder.

Figure 3.6: Left: BattSMAll galvanostat connected to a computer in the laboratory; Right: Our electrochemical cell and a coin cell in a holder for the *operando* measurement

3.4 Experimental Setup at ESRF

The *in situ operando* measurements, using the *in-house* built cell, were performed at beam line $BM26$ Dubble of the ESRF.

The X-ray beam, used for the experiment, had monochromatic wavelength of $0.82666\AA$ (corresponding to $15keV$) and spot size of $1.5x0.3mm$. The calibration of the detector was performed with the standard sample α-$Alumina$. The experimental setup consists of:

- Two X-ray detectors
  - Pilatus 1M (SAXS) 130cm far from the sample [49];
  - Pilatus 300K (WAXS) 27cm far from the sample.
- The vacuum tube
- The cell

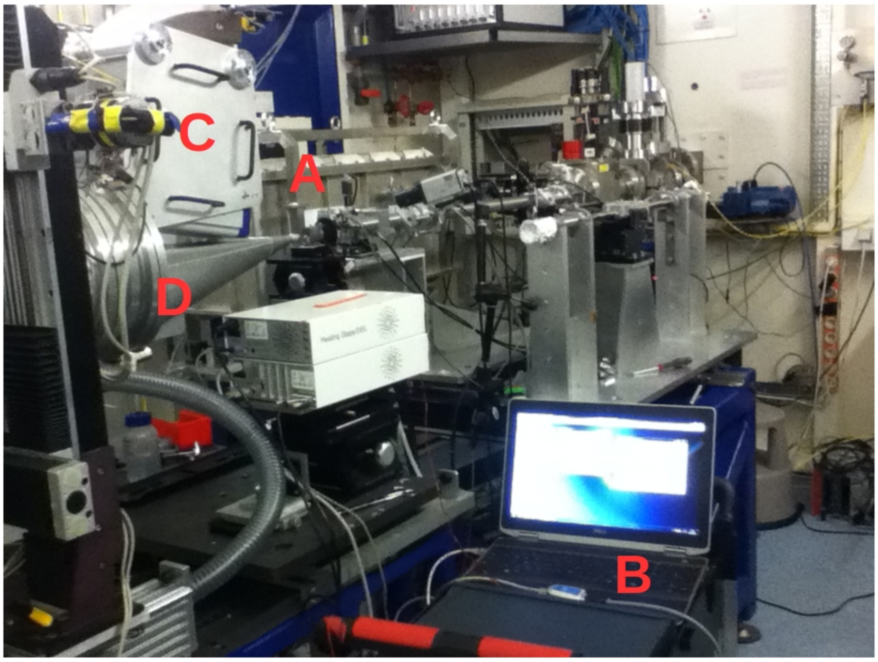

Figure 3.7: Experimental set up at ESRF, Beam Line BM26. A) position of the *in-house* built cell, B) the computer and the galvanostat, C) X-ray detector for WAXS Pilatus 300K, D) vacuum tube in front the SAXS detector Pilatus 1M

- The galvanostat

The experimental setup for *operando* SAXS and WAXS is reported in Figure 3.7. The different letters indicate the main components of the experiment. The cell is on the stage in the position A. Figure 3.8 shows the detail cell located in the holder in front of the X-ray shutter. B represent the position of the computer and the galvanostat. The X-ray detector Pilatus 300K for the WAXS signal is shown on position C. The SAXS apparatus needs a vacuum tube (Figure 3.7 D) that is closed with kapton window. The tube is necessary to avoid X-ray scattering of air molecules and adsorption between the sample and the detector. The detector Pilatus 1M is behind the vacuum tube, $130cm$ far from the sample because the distance improve the angular resolution of the data acquisition.

The standard sample α-*Alumina* was irradiated with X-ray for 30 sec in order to calibrate the detectors of WAXS and SAXS. Figure 3.9 and 3.10 are the measured profiles. Initially the detector reports the intensity as function of the its pixels

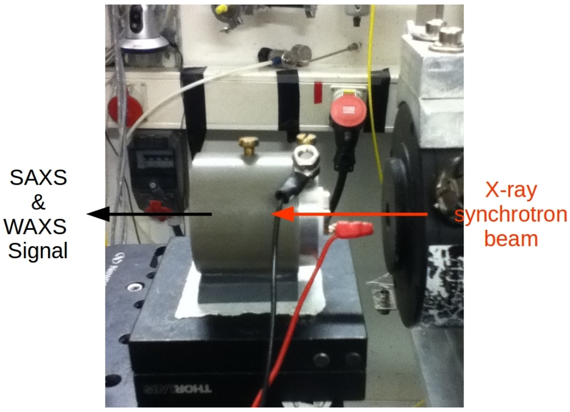

Figure 3.8: Detail of the *in-house* cell in the holder located in front of the X-ray beam shutter. The red arrow indicates the synchrotron X-ray beam entering in the cell. The black arrow indicates the transmitted beam for structural analysis.

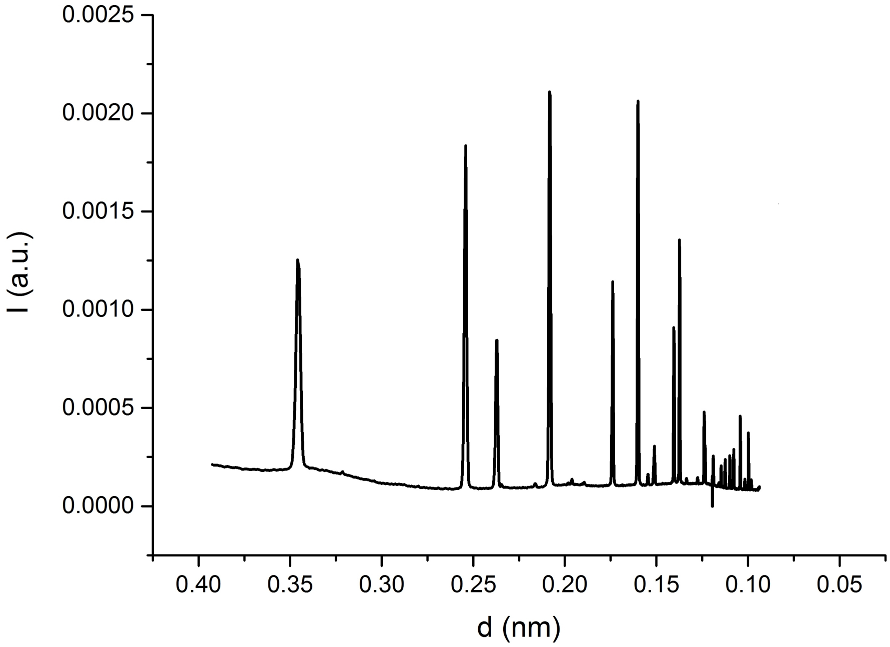

Figure 3.9: WAXS profile of the α-*Alumina*, measured for the calibration of the detector Pilatus 300K. The diffraction profile was used also for the extraction of the instrumental peak broadness

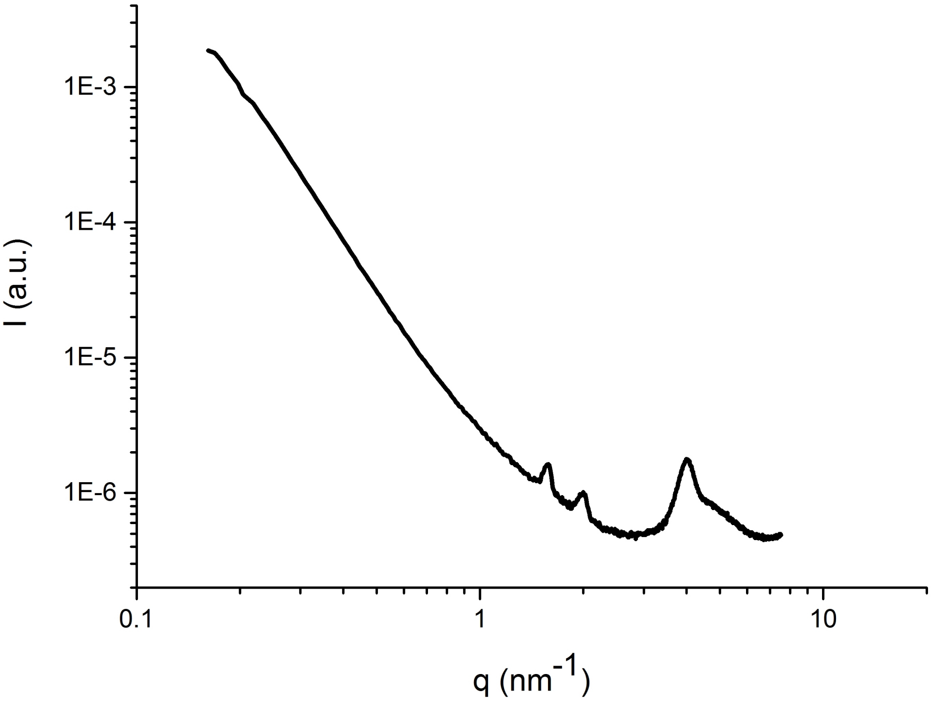

Figure 3.10: SAXS profile of the α-*Alumina* for the calibration of the detector Pilatus 1M

position. The positions of the WAXS and SAXS α-Alumina peaks are known. Using the peaks of the standard sample as reference, the calibration procedure consist of to convert the pixel position in q-value (nm^{-1}). The measurements are 2D-images that are converted in one dimensional information with a mathematical integration. Then the data can be plotted by a spreadsheet software. Using one of those software the q value scale of the WAXS measurements was converted in d-value scale (nm) using the relations eq.(2.50). Furthermore, a $H_s = 9.3\text{x}10^{-4} rad$ instrumental broadness of the WAXS apparatus was measured and then used for the calculation of the average crystalline size distribution by Sherrer formula eq. (2.49)

After such calibration, the blanks cell were exposed to the synchrotron X-ray beam for 15sec.

For the experiments with the active materials, each cell profile was collected every two minutes (60 sec for acquisition, 1.5 sec for saving the data, 58.5 sec for sleeping). It was assumed that during the acquisition time the internal situation of the cell was constant because the cycle, performed at $\frac{C}{10}$ was slow. This means that the applied current should perform the sodiation in $10h$ and the de-sodiation also in $10h$.

3.5 Scanning Electron Microscopy

The SEM analysis was done by a benchtop TM3000 microscope of Hitachi (Figure 3.11), equipped with a tungsten filament, back scattered electrons detector and an EDX detector of Bruker. An as prepared *a-P/C* powder samples were prepared by pressing the powders between two aluminium foils. A jet of compressed air was used to remove the unattached powder to one of the foils to avoid damage into the vacuum system (this procedure was done in a chemical hood to avoid the dispersion of the powder in the laboratory). The aluminium foil was simply fixed to the sample holder by a carbon tape. Usually the powders are directly spread on the carbon tape. However, in this case the aluminium foil is demanded because the quantification of the carbon in the sample will be affected by the X-ray emitted by the carbon tape. For the analysis of the anodes made of $FeSb_2$ and *a-P/C* a piece of tape was stuck directly on the sample holder by a carbon tape (in this case the compressed air was not used because the binder attached the powder to the metal foil).

Figure 3.11: TM3000 microscope of Hitachi

Chapter 4

Results

4.1 SEM Analysis of the *a-P/C* Powder

Figure 4.1 is a SEM picture and elemental map of the powder of *a-P/C* as extracted from the jar of the ball milling. The elemental map acquired by the EDX shows that carbon and phosphorus are homogeneously distributed. However, the quantitative analysis of the EDX spectrum (Figure 4.2) indicates that the concentration of carbon, as reported in Table 4.1, is higher than the phosphorus which suggests that the surface of the sample is mainly composed by carbon while the phosphorus is inside the matrix. Furthermore, the cluster have large size distribution.

Element	Atomic Concentration [%]	Error [%]
Carbon	61.32	5.4
Phosphorus	38.13	2.2
Aluminium	0.55	0.1

Table 4.1: Quantitative analysis by EDX of *a-P/C* as prepared powder

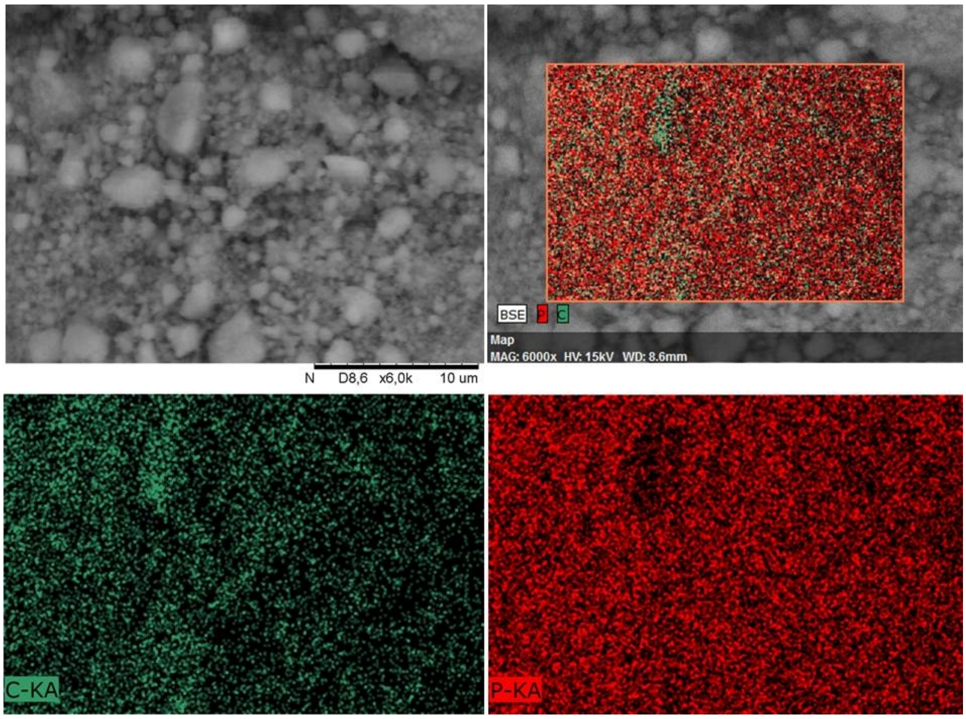

Figure 4.1: SEM image and elemental mapping profiles of a *a-P/C* powder on aluminium substrate

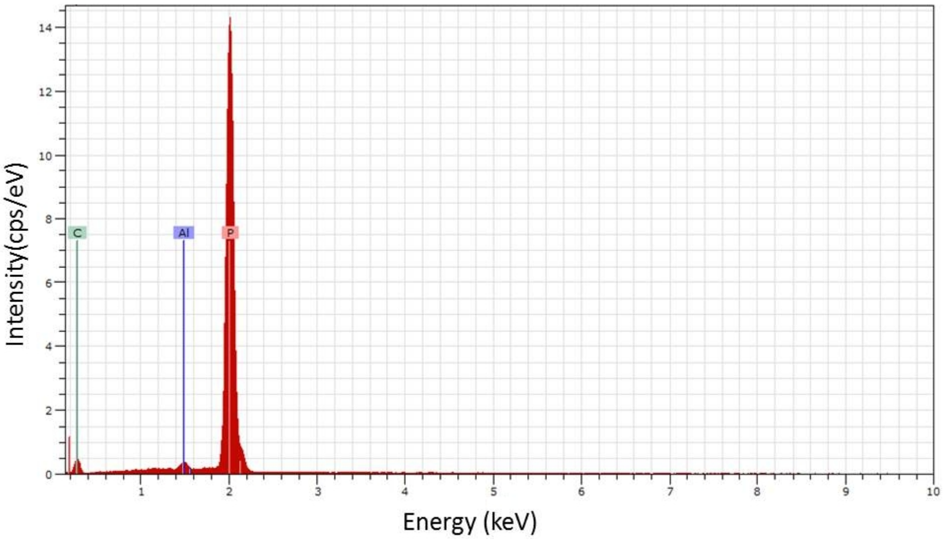

Figure 4.2: EDX spectrum of a *a-P/C*. The spectrum shows also the X-ray emitted by the aluminium substrate.

4.2 Galvanometric Performance of the *In-House* Built Cell

The characterization of the cell was carried out using the anodes as described in the section 3.1.2. The test were prepared both on coin cells and on our *in-house* cell with anodes cut from the same tape and the Electrolyte 1.

The measurements were performed at $\frac{C}{10}$ in both cases. However, the coin cell and the *in-house* built cell needed $9h$ and $8h$, respectively, to perform the first sodiation and $7h$ and $6h$, respectively, for the desodiation. The data are shown in Figures 4.3 and 4.4. The coin cell and the *in-house* built cell were assembled with $8mm$ and $16mm$ diameter anode disks, respectively. Therefore more active material was placed inside the *in-house* built cell than inside the coin cell. Thus, due to the dimension difference, we applied a constant current of $I = 0.15mA$ and $I = 0.6mA$ to the coin cell and the *in-house* built cell, respectively, in order to perform the test at $\frac{C}{10}$ for both cells.

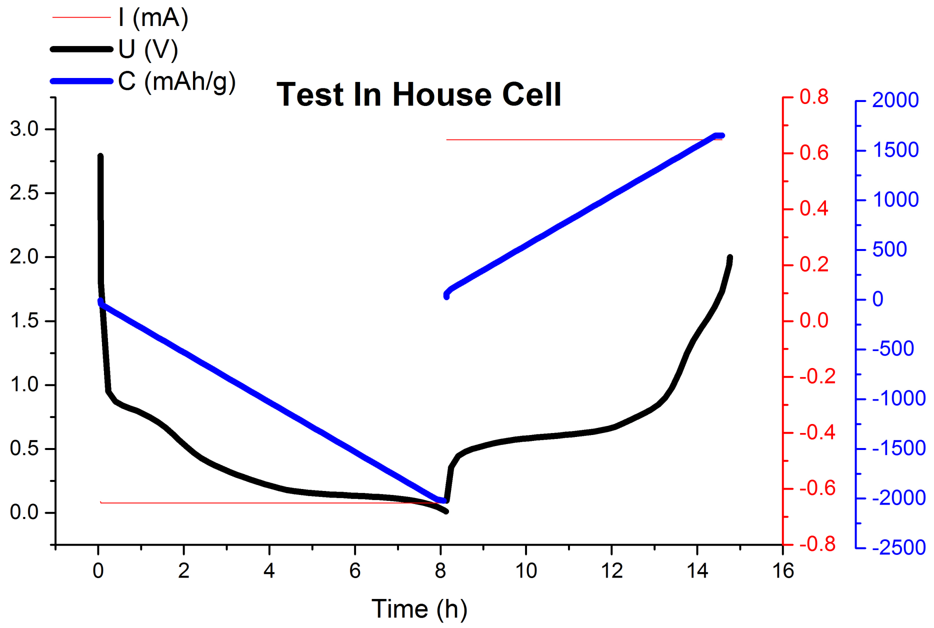

Figure 4.3: Galvanometric characterization of the *in-house* built cell: (blak) potential; (red) applied current; (blue) specific capacity

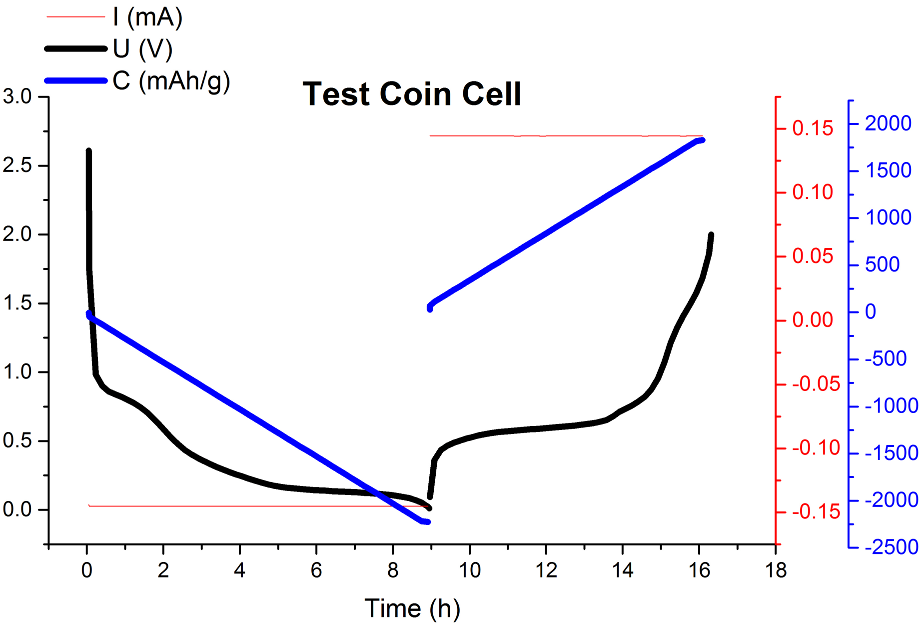

Figure 4.4: Galvanometric characterization of a coin cell: (blak) potential; (red) applied current; (blue) specific capacity

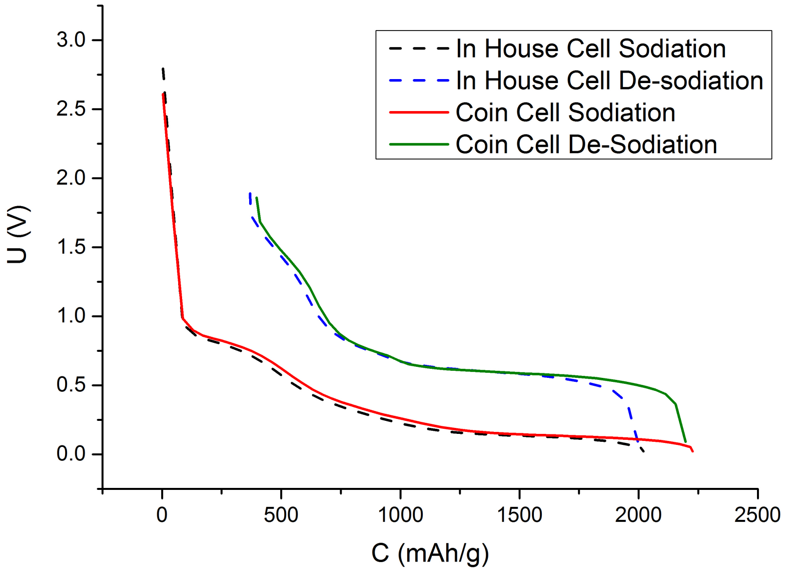

Figure 4.5: Comparison of the data between *in-house* and the coin cell

	in-house cell	Coin cell	IHC vs. CC
Capacity	$2021\frac{mAh}{g}$	$2226\frac{mAh}{g}$	90.79%
Reversible Capacity	$1653\frac{mAh}{g}$	$1829\frac{mAh}{g}$	90.37%
Coulomb efficiency	81.79%	82.16%	99.54%
Reversible C vs. Theoretical C.	66%	73%	90.41%
Time sodiation	$8h$	$9h$	88.9%
Time de-sodiation	$6h$	$7h$	85.71%

Table 4.2: Summary of the property of the *in-house* built cell (IHC), the coin cell (CC) and the comparison of the IHC *vs.* CC

In the Figure 4.5 the profile of the curve of the coin cell and the *in-house* built cell are almost overlapped at the beginning of the sodiation and at the end of the de-sodiation. The difference consist of longer plateaus at $0.14V$ (sodiation) and $0.5V$ (de-sodiation) for the coin cell. These determine an higher capacity for the coin cell: $2226\frac{mAh}{g}$, with a reversible capacity of $1829\frac{mAh}{g}$, and a Coulomb efficiency $\eta_c = 82.16\%$. The reversible capacity measured by the coin cell is 73% of the theoretical capacity of the *a-P/C*. The *in-house* built cell reached a capacity of $2021\frac{mAh}{g}$ reversible capacity of $1653\frac{mAh}{g}$ and a Coulomb efficiency of $\eta_c = 81.79\%$. The reversible capacity measured by the *in-house* cell is the 66% of the theoretical capacity of the active material. Table 4.1 summarize the comparison between the two cells. The electrochemical performance of the *in-house* built cell is the 90% of the coin cell. The comparison is summarized in the Table 4.2

4.3 Characterization of the *a-P/C* Anode

4.3.1 *Ex Situ* SEM Characterization (*a-P/C*)

Figure 4.6 shows the comparison of the surface of the as prepared tape (A) and the anode, extracted from the *in-house* cell, after the experiment at the ESRF (B). The surface of the as prepared tape appears regular without cracks and the chemical composition (Figure 4.6 C and D) show that carbon and phosphorus are homogeneously distributed. Figure 4.7 is the EDX spectra of the tape, while the quantitative analysis is reported in Table 4.3. The surface is composed by carbon and phosphorus with additional oxygen, possibly introduced in the material when was mixed with water. The surfaces of the anode before and after use are very different. The surface of the used anode looks irregular with a lot of big cluster and stripes around all the surface. Those cluster look brighter than the other part of the surface. This suggest that there are chemical elements heavier than carbon. Figure 4.8 is the detailed SEM analysis *ex situ* of the used anode. The elemental maps of the surface reveal the presence of sodium and oxygen, uniformly distributed and cluster with high concentration of fluorine. The fluorine source is the FEC decomposed during the electrochemical cycle [16]. To clarify this point two EDX spectra were collected in the two area delimited with the ring A and B in Figure 4.8. The quantitative analyses are reported in the Table 4.4 and 4.5

Element	Atomic Concentration [%]	Error [%]
Carbon	61.29	6.4
Phosphorus	25.10	1.7
Oxygen	13.61	2.1

Table 4.3: Quantitative analysis by EDX of the anode before used

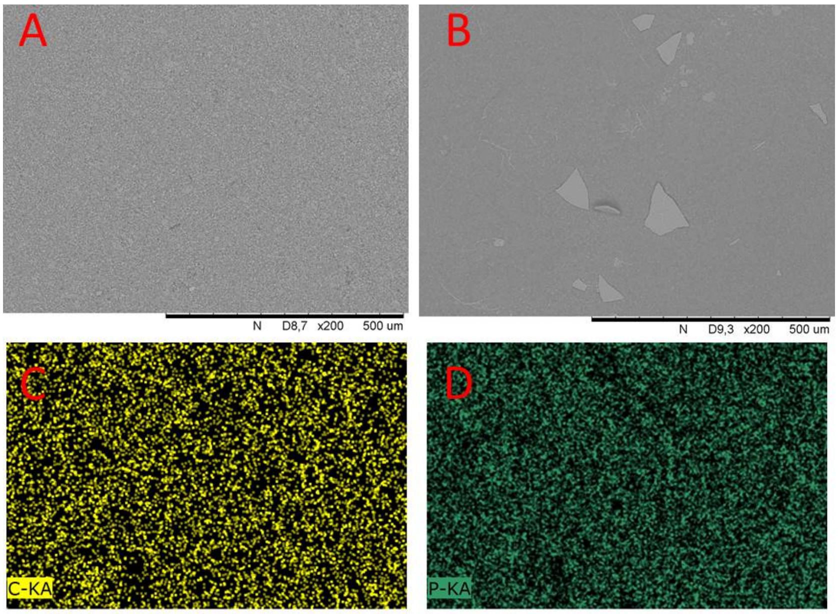

Figure 4.6: SEM images and elemental mapping profiles of a *a-P/C* A) SAM image of is the surface of a piece of the tape used as anode for the experiment; B) SEM image of the surface of the anode extracted from the *in-house* cell after the experiment at the ESRF; C), D) carbon and phosphorus mapping profile of the surface in A).

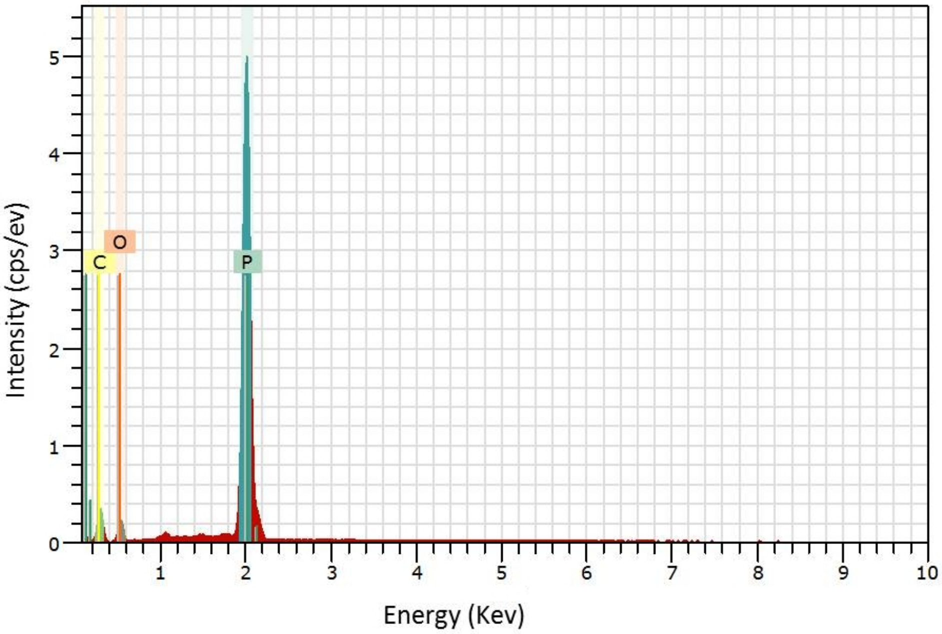

Figure 4.7: EDX spectrum of the sample showed in Figure 4.6 A

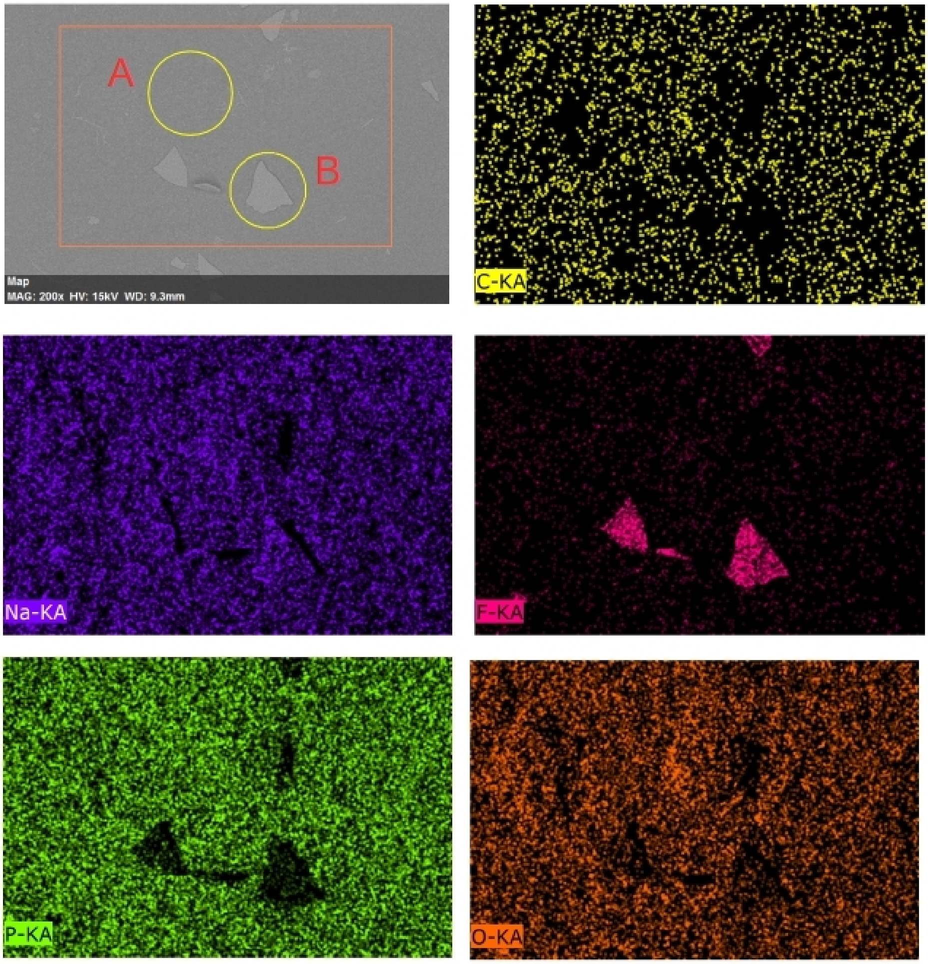

Figure 4.8: SEM analysis of the extracted anode after use. The elemental maps show the presence of sodium, fluorine and oxygen, in addition to carbon and phosphorus.

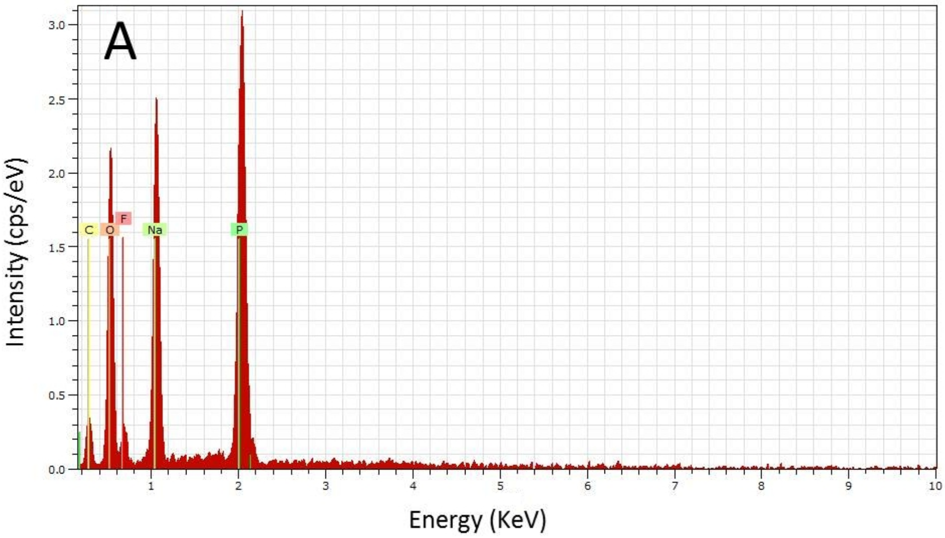

Figure 4.9: EDX spectrum of the area Figure 4.8 A

Element	Atomic Concentration [%]	Error [%]
Oxygen	42.50	5.4
Carbon	26.99	3.9
Sodium	13.56	1.0
Phosphorus	10.56	0.7
Fluorine	6.39	1.5

Table 4.4: Elemental composition of the selected area of Figure 4.8 A

Element	Atomic Concentration [%]	Error [%]
Fluorine	28.15	3.5
Oxygen	25.72	2.9
Carbon	18.96	2.6
Sodium	16.40	1.0
Phosphorus	8.26	0.4
Silicon	2.52	0.1

Table 4.5: Elemental composition of the selected area of Figure 4.8 B

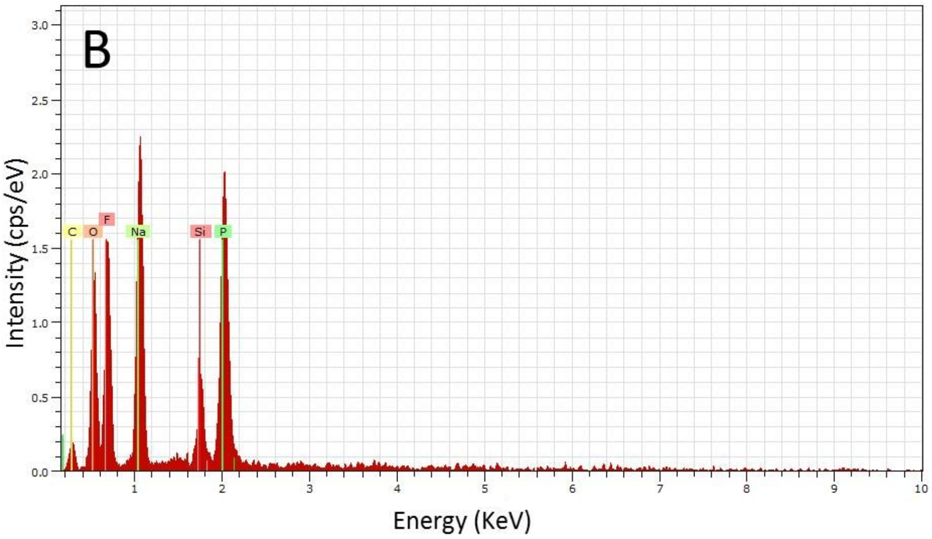

Figure 4.10: EDX spectrum of the area Figure 4.8 B. The silicon peak at $E = 1.7KeV$ is caused by the detector.

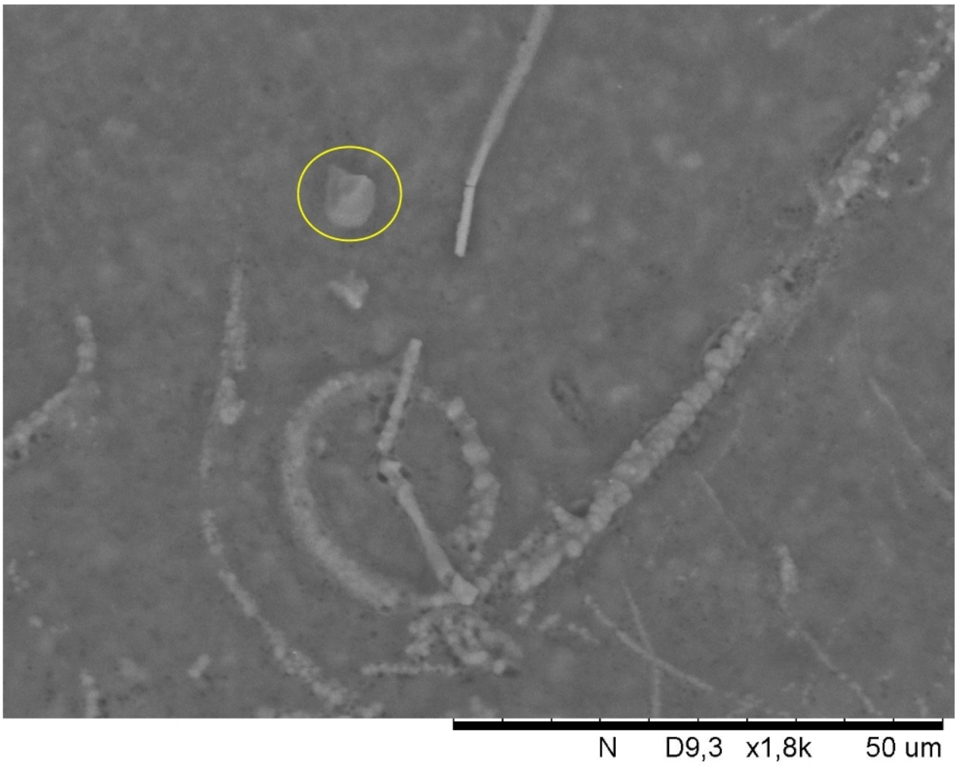

Figure 4.11: SEM image of the stripes and small clusters

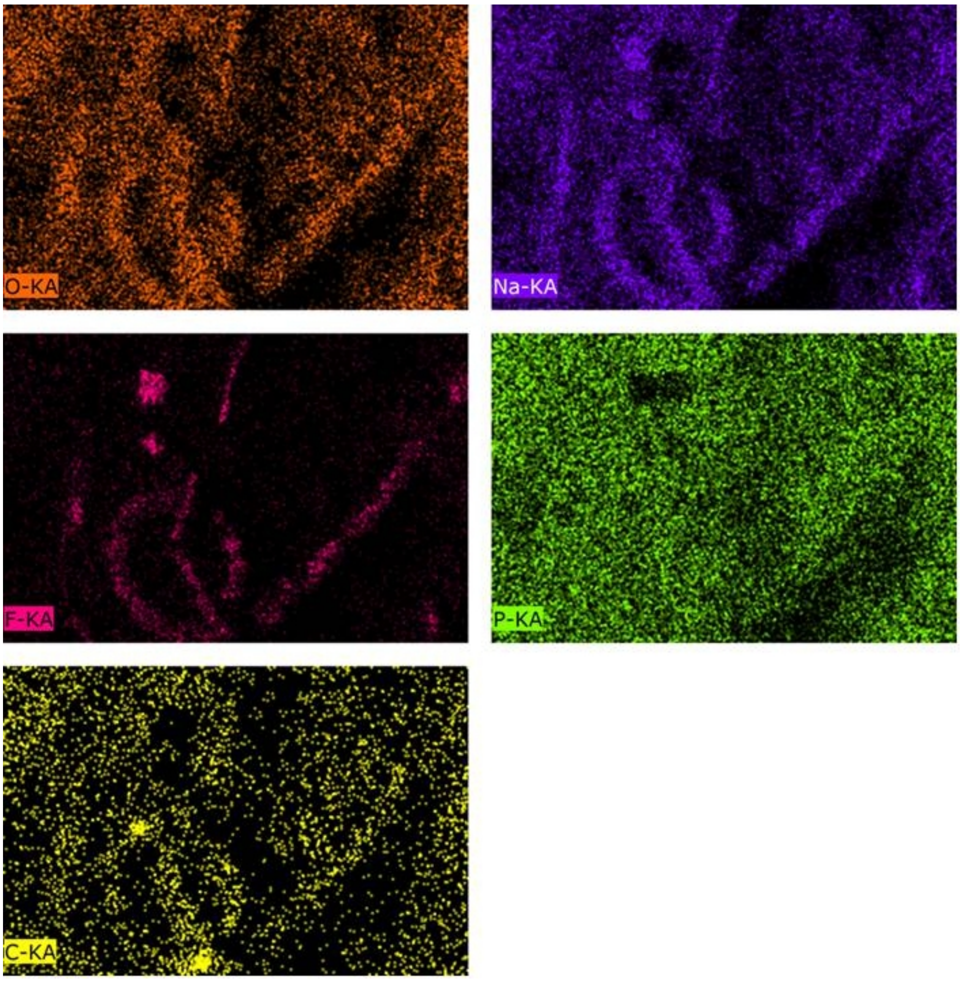

Figure 4.12: Elemental maps of the SEM image in Figure 4.11

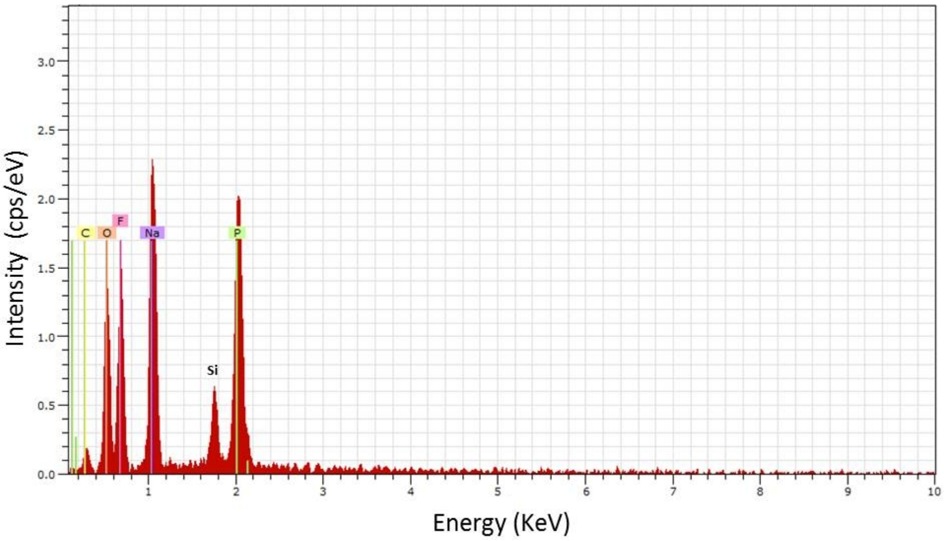

Figure 4.13: EDX spectrum of the are marked area with a yellow circle in Figure 4.8. The silicon peak at $E = 1.7KeV$ is caused by the detector.

A detail of the stripes and small cluster on the surface of the used anode is reported in Figure 4.11. The higher magnification of the image allows to appreciate the structure of this brighter areas: they looks irregular with large size distribution and different shape. The chemical mapping (Figure 4.12) and the quantitative analysis of the EDX spectrum (Figure 4.13) reported in the Table 4.6 indicates again a high concentration of fluorine. The chemical composition measured at higher magnifications and reported in Table 4.6 is similar to the one reported in the Table 4.5 collected at lower magnification. This condition suggest that the big and small cluster and the stripe are made of the same composition.

Element	Atomic Concentration [%]	Error [%]
Oxygen	28.07	3.5
Fluorine	27.48	4.0
Sodium	18.26	1.1
Carbon	17.32	03.0
Phosphorus	8.87	0.5

Table 4.6: Elemental composition of the selected area in Figure 4.8

4.3.2 *In Situ Operando* SAXS and WAXS with Our *In-House* Built Cell (*a-P/C*)

The electrochemical and the *in situ* X-ray characterization started simultaneously. The BattSMALL recorded the potential once every minute while the X-ray detectors acquired data once every two minutes. According to the numeration on the files, the datasets were correlate in time.

The galvanometric measurement (Figure 4.14) was carried out at $\frac{C}{10}$ applying $I = 400\mu A$. The sodiation and the de-sodiation required $8h$ and $7h$ respectively, reaching the first sodiation capacity of $2000\frac{mAh}{g}$ and a reversible capacity of $1763\frac{mAh}{g}$. The results show that the sodiation process is characterized by two slopes $1.4 - 0.4V$ and $0.4 - 0.18V$ and one plateau at $0.16V$. The de-Sodiation profile has one plateau at $0.5V$ and three slopes: $0.6 - 0.8V$, $0.8 - 1.2V$, $1.2 - 1.5V$

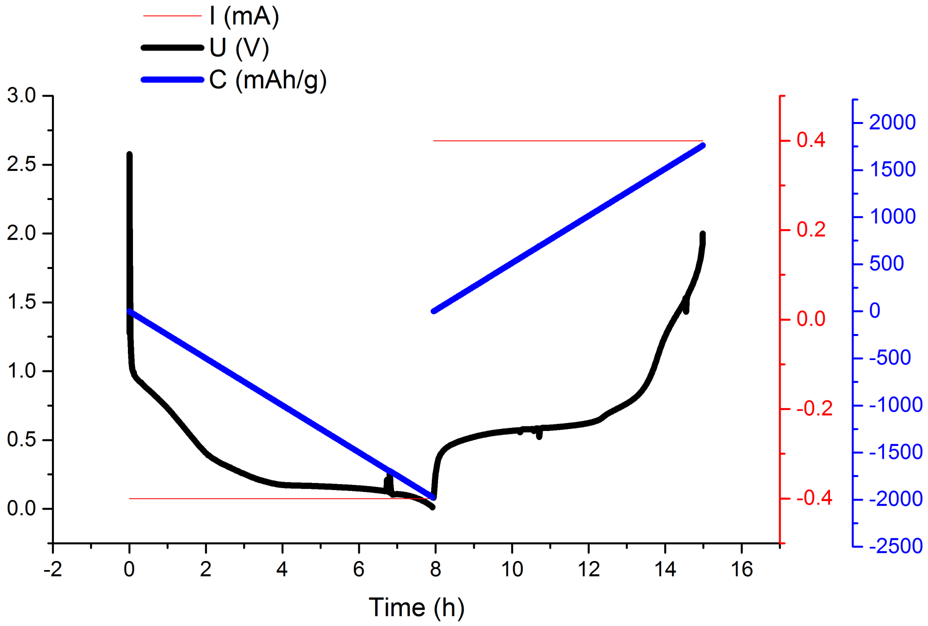

Figure 4.14: Galvanometric measurement of the *in-house* built cell assembled with the *a-P/C* anode

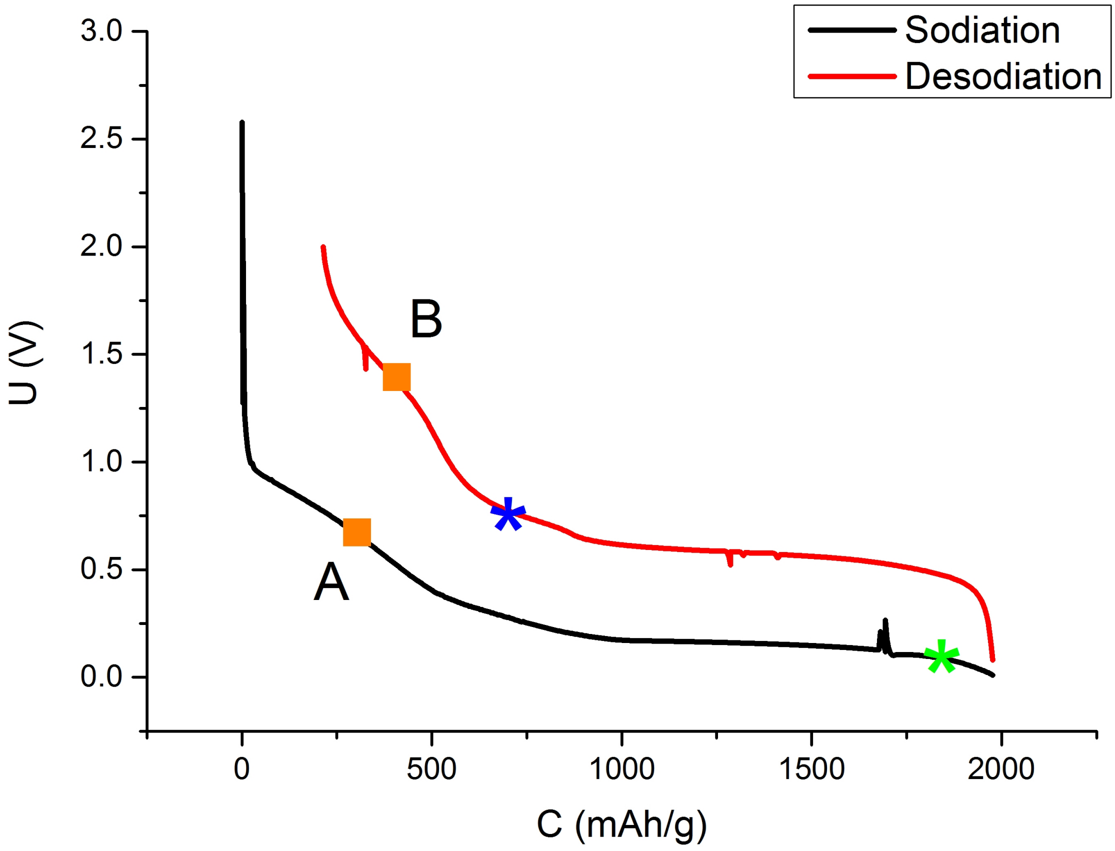

Figure 4.15: Potential *vs.* capacity of the *in hose* built cell with the *a-P/C* anode. The green and the blue asterisks are the point when the crystalline Na_3P appears and disappear in the corresponding WAXS measurements, respectively. The orange squares are the points where peaks arise in the SAXS profile at $q = 4.7nm^{-1}$ and $q = 1.38nm^{-1}$ consistent with Figure 4.22 A and Figure 4.22 B.

In the Figure 4.15 the galvanometric measurement data are plotted as potential *vs.* capacity. The green asterisks is the point where the crystalline powder diffraction pattern of the Na_3P starts appearing on the WAXS profile (No. 210). The point correspond to the potential $0.10V$. The blue asterisk indicate the point where the powder diffraction profile of the Na_3P completely disappears. This happens at the potential of $0.74V$ that correspond to the X-ray measurement No. 390

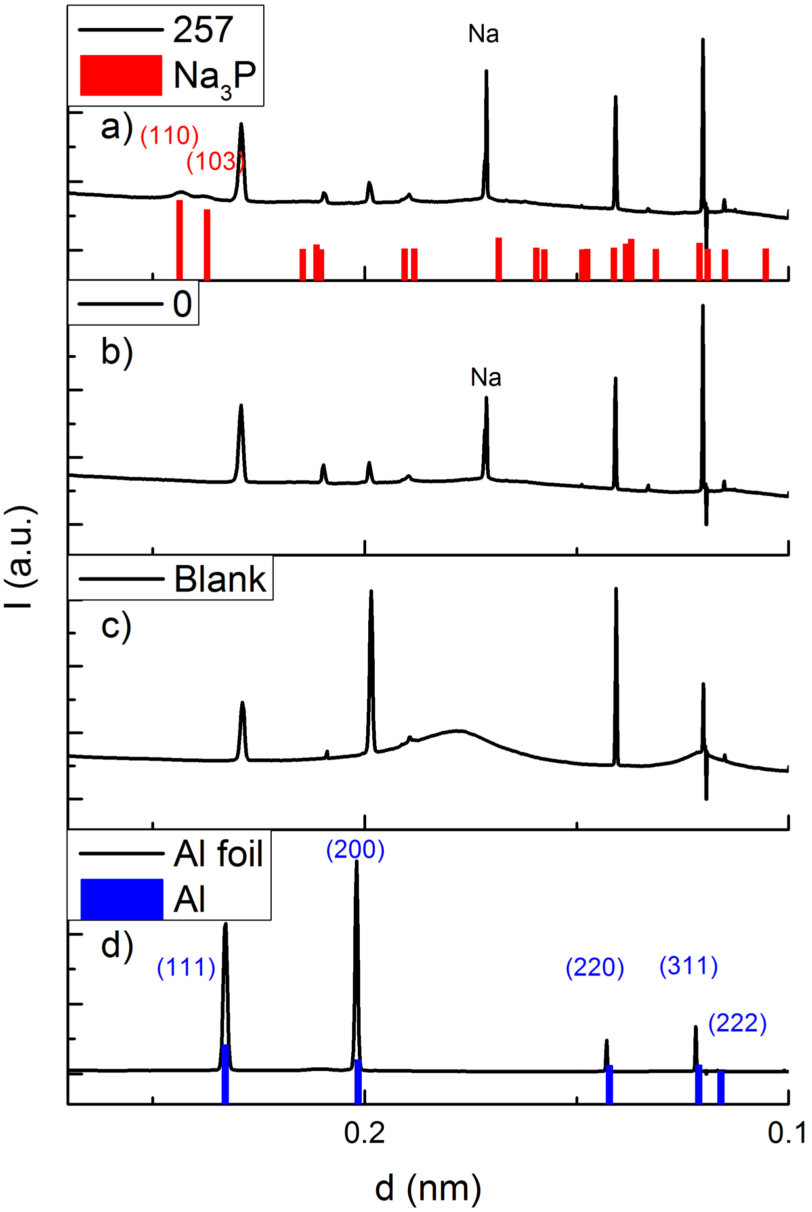

Figure 4.16: Selected WAXS profiles of characterization of the *in-house* built cell assembled with the *a-P/C* and reference of Na_3P and aluminium. a) It is the measurement No. 257 when the sodiation ends and the peaks of the Na_3P reach the maximum intensity. b) It is the measure No. 0 and the first measurement of the experiment. c) It is the WAXS profile of the Blank cell used as reference. d) It is the aluminium foil similar to the one used for the preparation of the tape [50]. The peaks assigned to Na are sodium peaks diffracted by the cathode.

Figure 4.16 a) shows the diffraction pattern of the measurement No. 257. This is the last measurement of the sodiation process, when the peaks (110) and (103) of the crystalline Na_3P reach the maximum intensity. The *in-house* built cell is made of different crystalline materials located along the X-ray beam path. Therefore, the WAXS profile No. 257 presents all the diffraction patterns of those materials. When the sodiation finishes, the highest two peaks of the Na_3P are detected, while the other peaks are negligible. The strong peaks at $d = 0.23nm$, $d = 0.20nm$, $d = 0.17nm$, $d = 0.14$, $d = 0.12nm$ and $d = 0.11$ are due to the aluminium foil used as substrate for the anode fabrication and the peak $d = 0.17$ belongs to the sodium cathode. Those peaks are obviously visible in the measurement No. 0 in Figure 4.16 b) and proved by the profile of pure aluminium foil in Figure 4.16 d). The profile in Figure 4.16 d) was measured putting the an aluminium foil, similar to the one used for the cathode fabrication, on a standing holder. The intensity of the aluminium foil peaks intensity change compared to the blank (Figure 4.16 c)) and the measurement No. 0 and 257. This is due to the orientation of the foil compare to the incident beam. This means that the small crystalline domains in the aluminium foil are oriented and they do not have a random distribution like in a powder. It happen the same for the sodium cathode. In the Figure 4.16 a) and b) sodium is in Bragg condition, while in the blank measurement (Figure 4.16 c)) it is not in Bragg condition. There are also other small peaks in the diffraction patterns of the *in-house* built cell that remain unidentified. Furthermore, in the blank measurement there is a hump centred at d= and its origin is not clear

It has to be noted that the standing holder (used for the measurement reported in Figure 4.16 d)) and the aluminium foil in the cell are not in the same position. In the latter the aluminium is a few centimetres toward the detector. The different positions induced that the diffraction pattern does not have the same origin. Therefore, they looks shifted compare to each other. This is a problem that affect all the diffraction pattern measured within the cell, because all the components of the cell are in different positions. For the crystal phase identification it is necessary to shift the position of the tabulated peaks. In fact the peak positions of the crystalline Na_3P (red bar in the Figure 4.16) are shifted of $\Delta = -0.0053nm$.

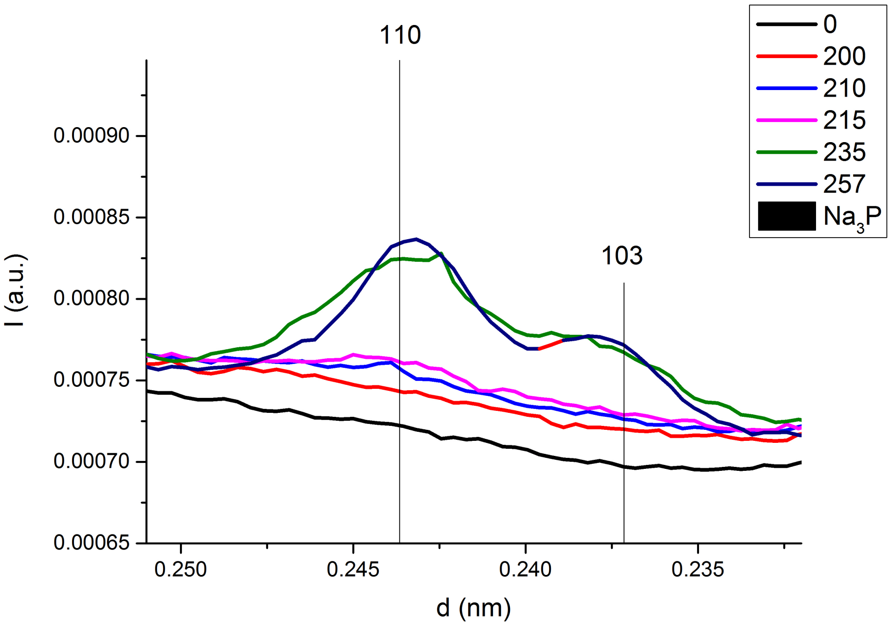

Figure 4.17: WAXS profiles showing the increase of peak intensities of the (110) and (103) reflections of Na_3P during the sodiation

During the sodiation the chemical composition of the active material changes from amorphous phosphorus to crystalline Na_3P passing through different phase transition. The system changes progressively towards the sodium rich phase. However, only the pure phase Na_3P is crystalline. In fact the WAXS profiles of the measurements from No. 0 to the No. 200 do not show additional peaks. Figure 4.17 shows the evolution of the WAXS profiles in the d-range $0.250 - 0.215nm$ during the sodiation. From the measurement No. 0 to No. 200 the base line remains flat in that range. At measurement No. 210 the profile of the peak (110) starts rising. The peaks become progressively more intense and sharp, which means that the quantity and the size of crystalline material increase. At the measurement No. 257 the size of the crystalline domain is $\tau = 25 \pm 0.1nm$ according to the Sherrer formula eq.(2.49). The input values for the formula were:

- FWMH of the Na_3P (110) peak: $H_{(110)} = 3.4\text{x}10^{-3}rad$
- FWMH of the Na_3P (103) peak: $H_{(103)} = 3.1\text{x}10^{-3}rad$

- FWMH of the α-alumina peaks: $H_s = 9.3\text{x}10^{-4} rad$

We calculated the average size distribution for each of the two Na_3P peaks and then we calculated the mean value. Figure 4.18 shows the opposite process: during the de-sodiation the peak intensities reduce until they disappear complitely at the measurement No. 390. During this process the system pass through the following phase transition Na_3P, Na_2P, NaP, NaP_7 and P. According to the literature the profile of the galvanometric sodiation curve and de-sodiation curve are different because the phase transition are different.

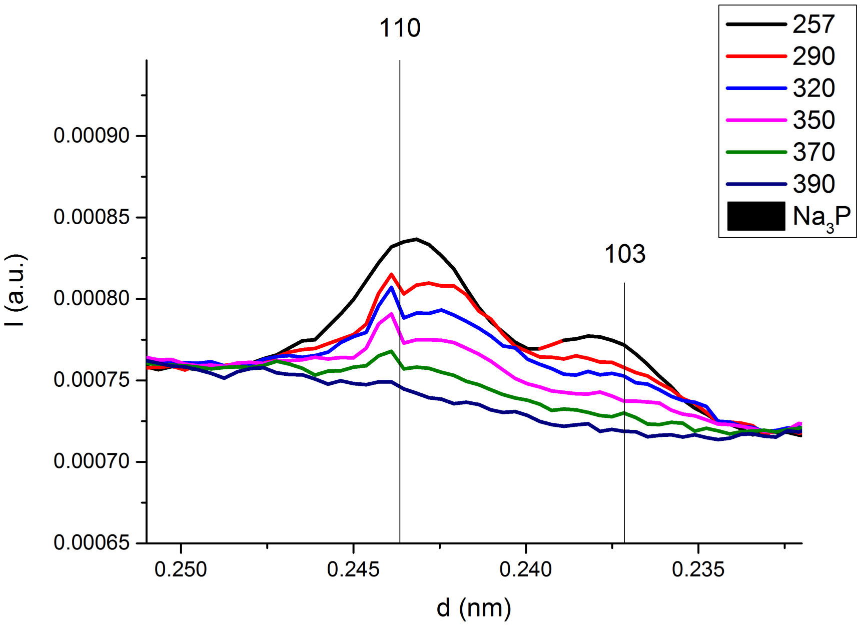

Figure 4.18: WAXS profiles of the Na_3P showing the decrease of peak intensities of the (110) and (103) reflections during the de-sodiation in the d-range $0.250 - 0.230 nm$. The peaks intensity decreases during the de-sodiation. The peak at $d \approx 0.244$ is a detector spike.

Figure 4.19 shows an overview of selected SAXS and WAXS profiles. If one considers only the WAXS measurements No. 0 and No. 449, the system appears reversible considering that the pattern are similar. However, the SAXS profiles change and indicate that the battery the profiles does non come back to the original state. Figure 4.20 and 4.21 show the overlapped SAXS profiles in the q-range $0.1 - 10nm^{-1}$ during the sodiation and de-sodiation, respectively. However, the difference is more significant with the overlap of the profile during the de-sodiation (Figure 4.21). The difference between the beginning of the sodiation and the end of the de-sodiation is well visible in Figure 4.22 where are plotted the first (No 0) and the last (No. 449) measurement. The two curves can not be overlap ad except for the kapton profile that remain constant. Furthermore, two extra peaks appear. The peak A appears at measurement No.40 after $1h20min$ from the start of the experiment, when the potential of the cell is $0.63V$. The peak intensity reaches the maximum at measurement No. 257 and, during the de-sodiation, its intensity remains constant. Although, the peak became broader. The peak B appears at the measurement No. 423, during the de-sodiation, when the potential of the cell is $1.4V$ and its intensity fluctuate during the process.

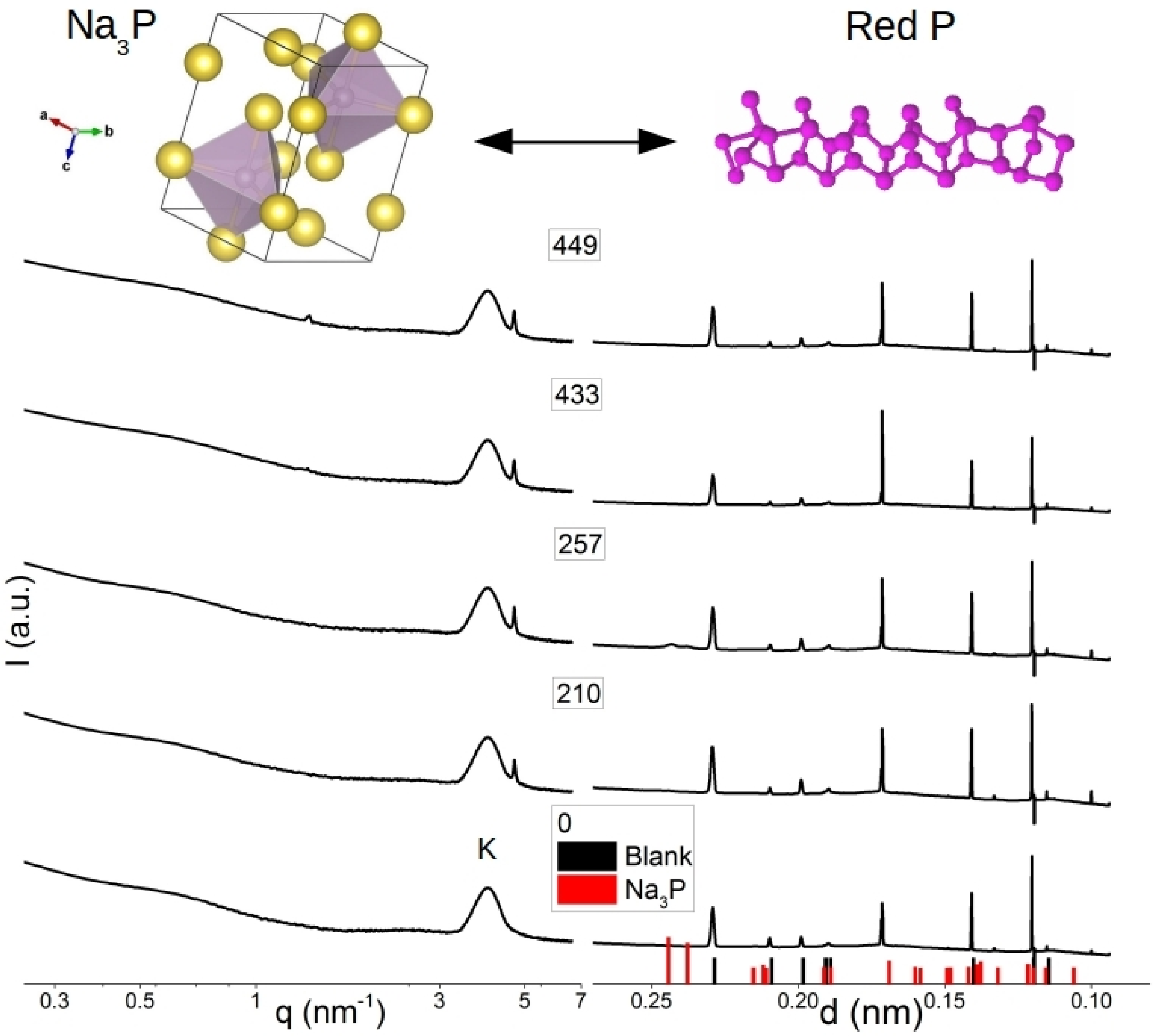

Figure 4.19: Overview of the (left) SAXS and (right) WAXS profiles with standard reference of Na_3P(red bars) and reference of the *in-house* built cell (blank: black bars). The broad peak marked with K in the SAXS profiles is due to the kapton windows of the cell. The illustration on the top depicts the phase transition between crystalline Na_3P and amorphous phosphorus.

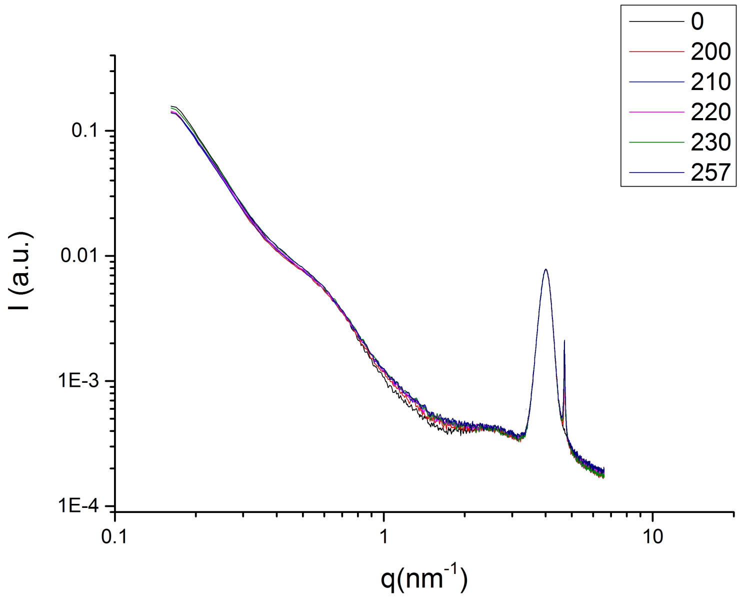

nn

Figure 4.20: Selected SAXS profiles during the sodiation. The profiles are almost overlapped in the q-range $0.16 - 3.2nm^{-1}$. The broad kapton peak remains unchanged. A peak arises at $q = 4.7nm^{-1}$.

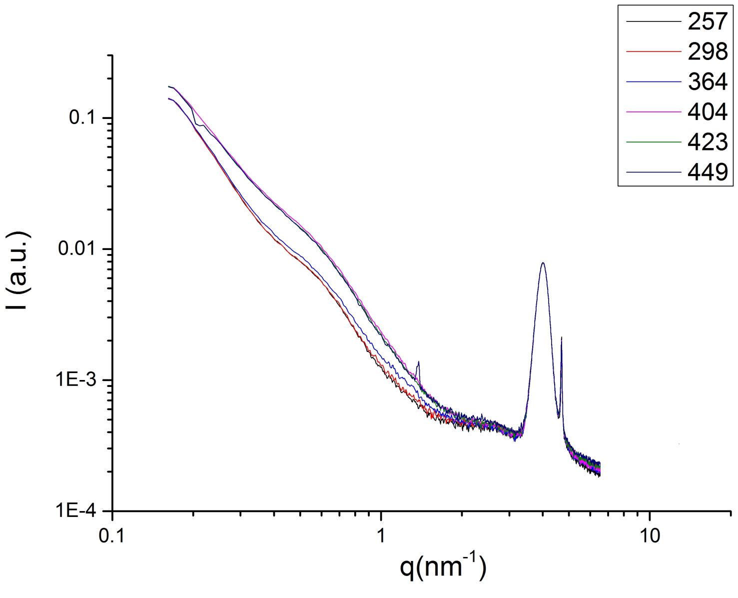

Figure 4.21: Selected SAXS profiles during the de-sodiation. The profiles change drastically in the q-range $0.16 - 3.2nm^{-1}$. A second peak arises.

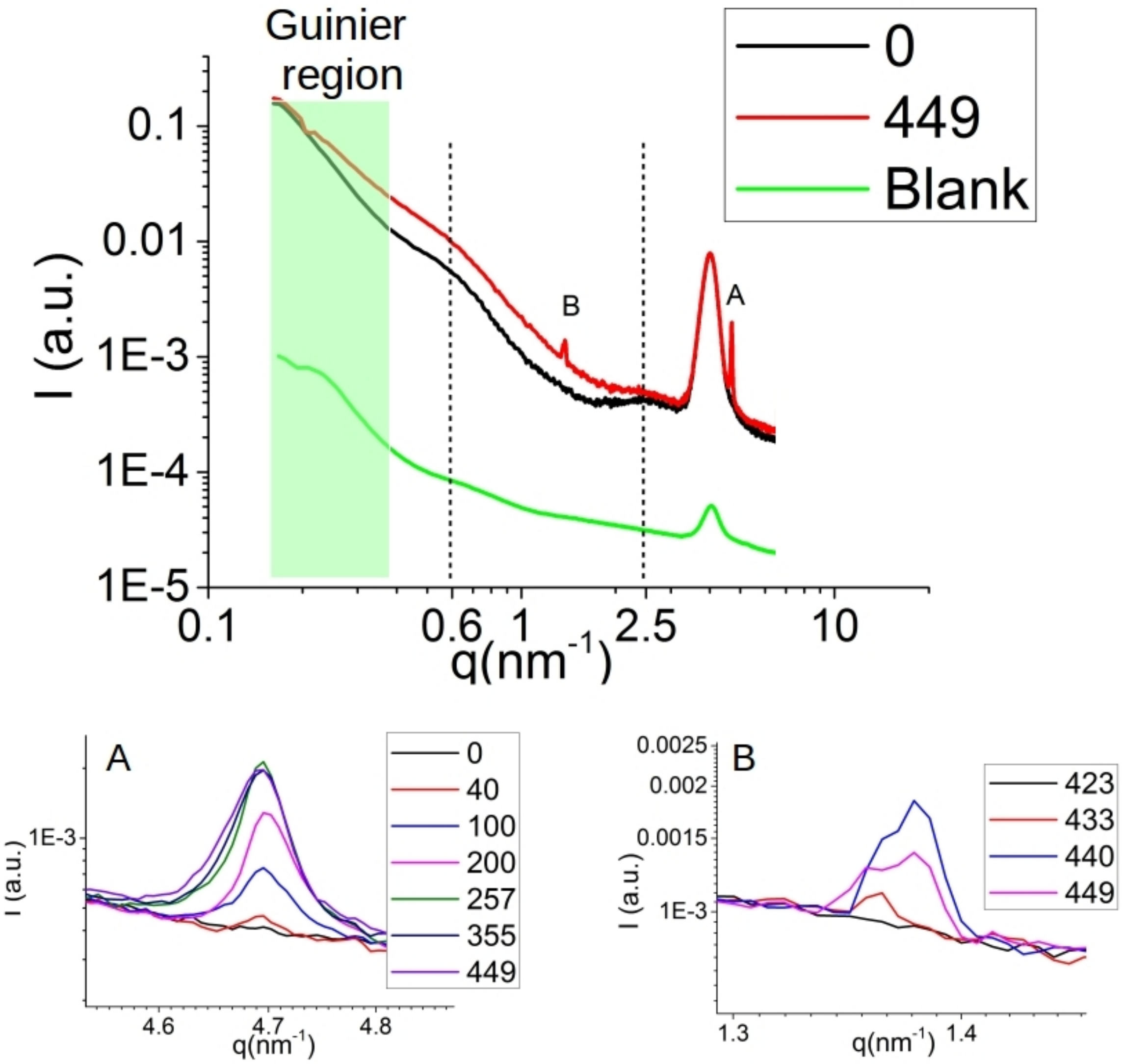

Figure 4.22: (Top) Full scale of the SAXS profiles and (bottom) (A, B) selected SAXS profiles for the details about marked area in the full-scaled SAXS profiles. The light green area is the Guinier region in the q-range $0.16 - 0.4nm^{-1}$. The dash lines indicate the characteristic features around $q \approx 0.6nm^{-1}$ and $q \approx 2.5nm^{-1}$. Upon cycling the batteries is consistent with a non total conversion of the system.

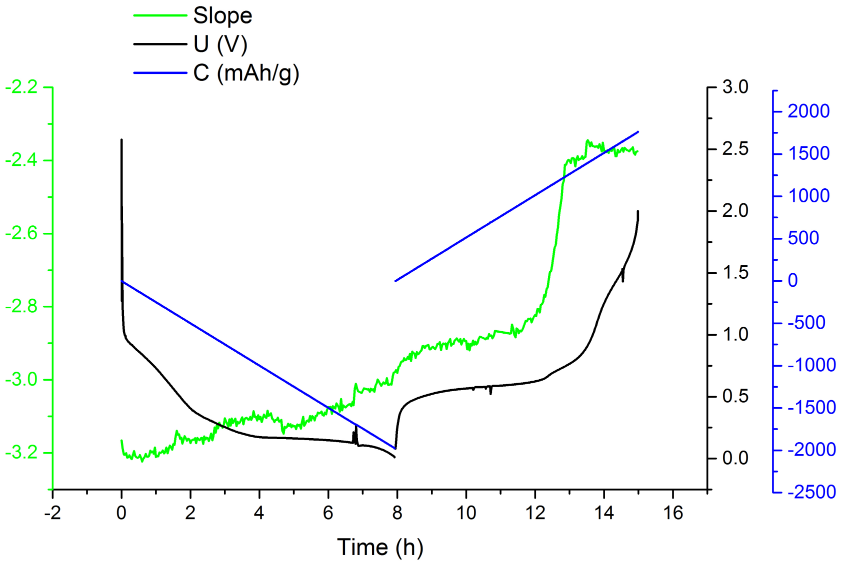

Figure 4.23: The variation of the slope of the SAXS curve, measured in the Guinier region (q-range $0.16 - 0.4nm^{-1}$), overlapped with the electrochemical characterization of the cell

The value of the slope of the right lines that approximate the SAXS curve in Guinier region q-range $0.16-0.4nm^{-1}$ changes during the entire cycle (green curve in Figure 4.23). The value of the different slope is reported in function of the time and overlapped to the electrochemical characterization. At the beginning of the sodiation the slope value is -3.2 and than progressively change to -2.9 corresponding to the end of the plateau. A huge variation of the SAXS slope value happens in correspondence to the potential range $0.6-0.8V$. In the last part of the de-sodiation (from patterns No. 390 to No. 449) the SAXS slope value oscillates around the value of -2.4. From the analysis of the SAXS curve (Figure 4.20) it is possible to notice two characteristic features centred around $q \approx 0.6nm^{-1}$ and $q \approx 2.5nm^{-1}$ (Figure 4.22). The slope of the curve around these values suggest the presence of spherical aggregation. The formation of the peak at $q \approx 4.5nm^{-1}$ suggest that during the sodiation large crystal structures of a lamellar phase are forming. During the de-sodiation (Figure 4.21) the patterns tend to lose their global feature in particular around $q \approx 0.6nm^{-1}$ and $q \approx 2.5nm^{-1}$ while a peak at $q \approx 1nm^{-1}$ appears. This could be explained by a particular ordering of building blocks with a lamellar structure. The formation of this phases could be related to the partial reversibility of the reaction.

4.4 Characterization of the $FeSb_2$ Anode

4.4.1 *Ex Situ* SEM Characterization of the $FeSb_2$ Anode

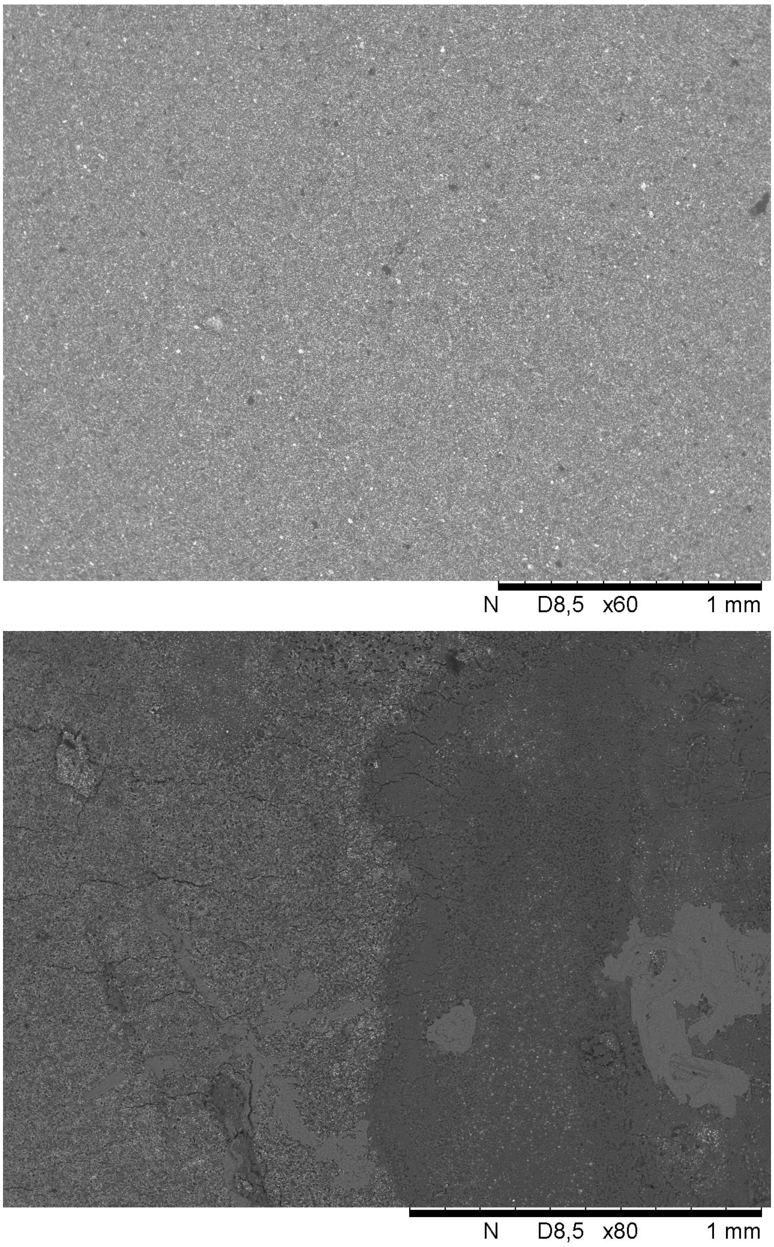

Figure 4.24: SEM images of the surface of the $FeSb_2$ tape (top) before and (bottom) after used

The SEM images shown in Figure 4.24 illustrate a drastic variation in the morphology of the tape surface before and after the use. The surface of the unused tape looks uniform and the elemental mapping profiles (Figure 4.25) shows an homogeneous distribution of iron and antimony with relative ratio close to 1:2. The sample has large quantity of carbon as seen in Table 4.7. After the surface morphology of the sample looks irregular with several cracks and domains with different contrast (Figure 4.25). However, the elemental mapping profile of the antimony, sodium, carbon and iron are homogeneous (Figure 4.27). The quantitative analysis (Table 4.7) of the EDX spectrum (Figure 4.28) suggests that a new layer having a different elemental composition from the original electrode is formed on the electrode. The relative concentration of iron and antimony is modified with an increase in iron percentage. After the use in the battery the chemical composition consist mainly of sodium, oxygen, and carbon (Table 4.8). However, the source and the state of oxygen is unclear. the chemical composition of the surface is mainly composed of sodium, oxygen and carbon. The oxidation of the tape could take place during the galvanometric cycle or during the exposition to the air before the SEM analysis.

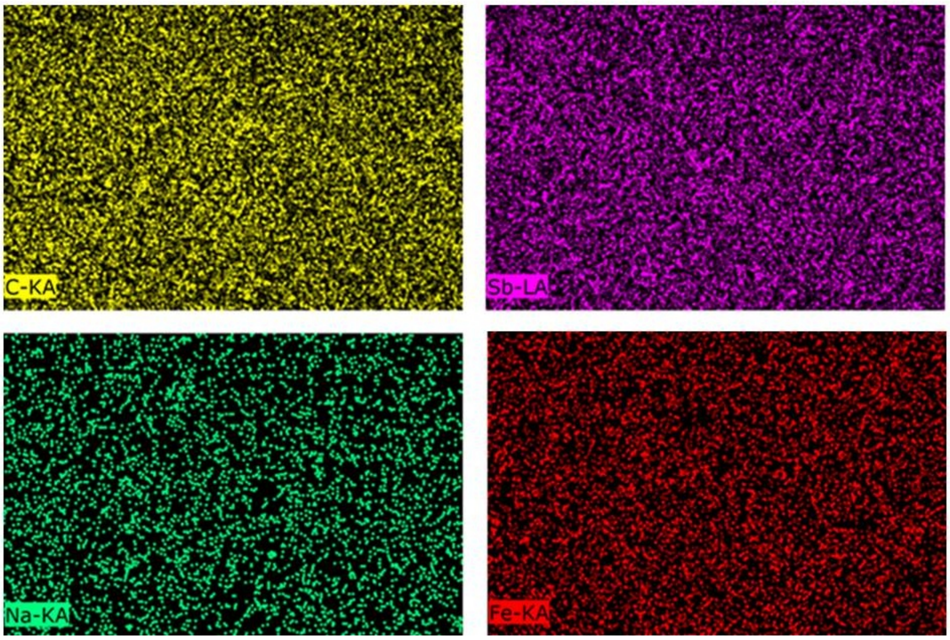

Figure 4.25: Elemental mapping profiles of the tape made of $FeSb_2$ before used

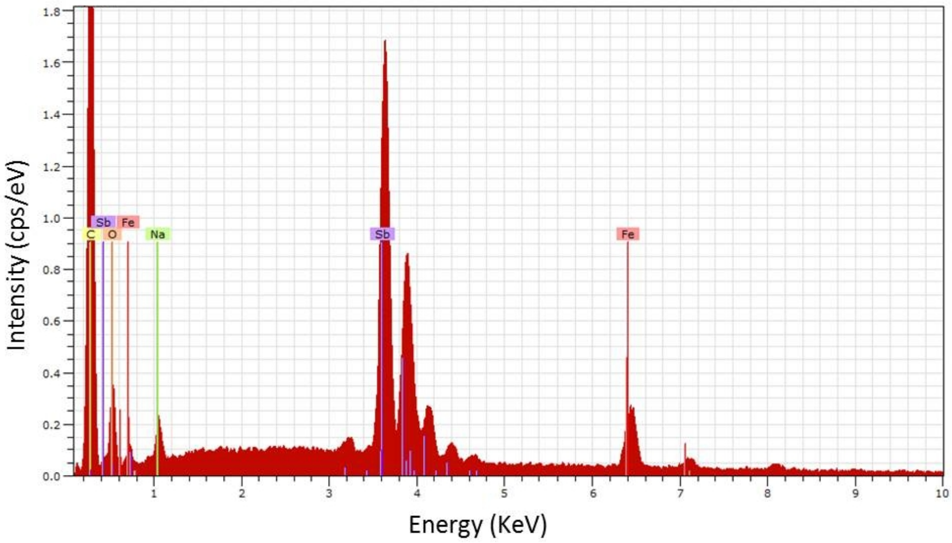

Figure 4.26: EXD spectrum of the tape made of $FeSb_2$ before used

Element	Atomic Concentration [%]	Error [%]
Carbon	72.16	3.3
Antimony	11.73	1.4
Oxygen	7.45	0.6
Iron	5.11	0.3
Sodium	3.55	0.2

Table 4.7: Elemental composition of the $FeSb_2$ tape shown in Figure 4.26

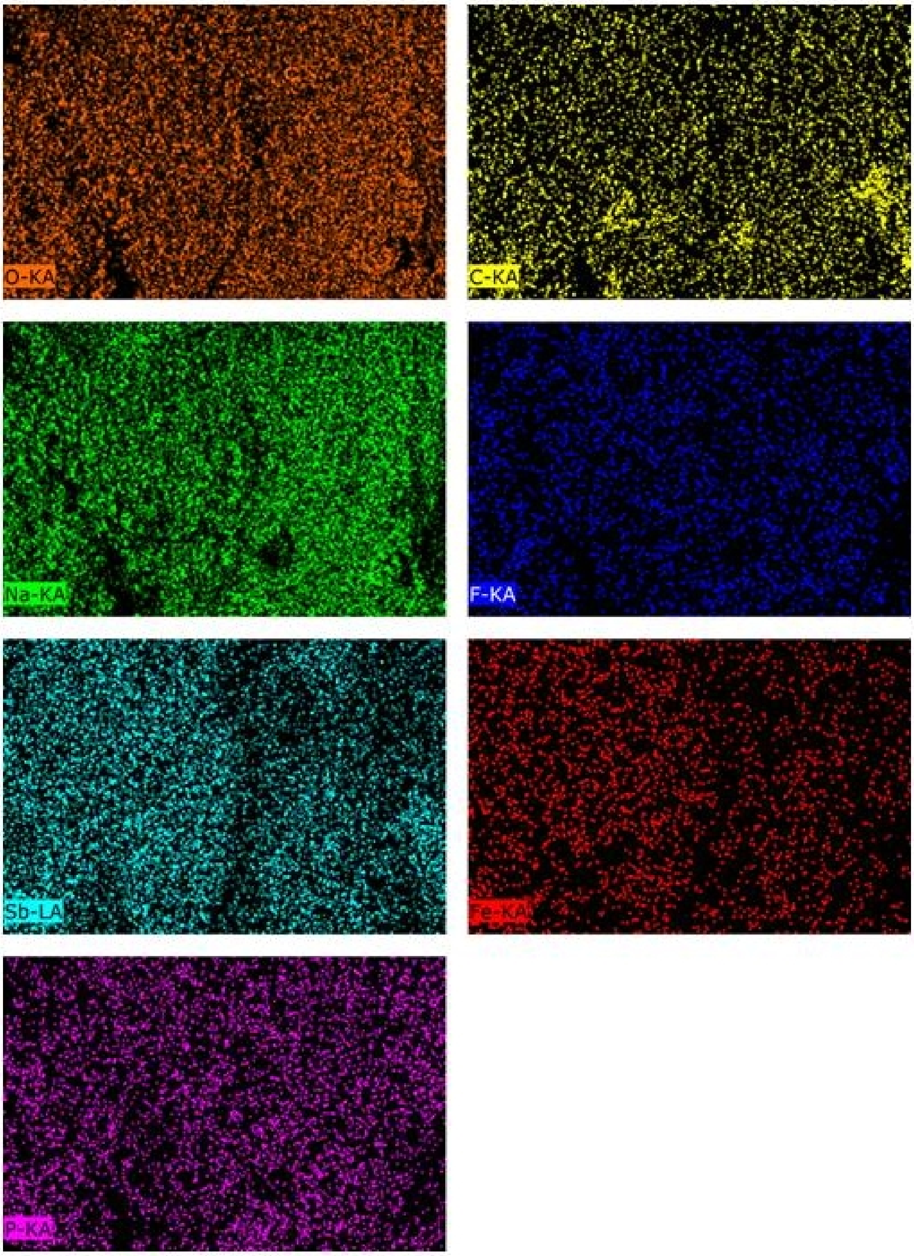

Figure 4.27: Elemental mapping profiles of the $FeSb_2$ anode extracted from the *in-house* built cell after the experiment at ESRF

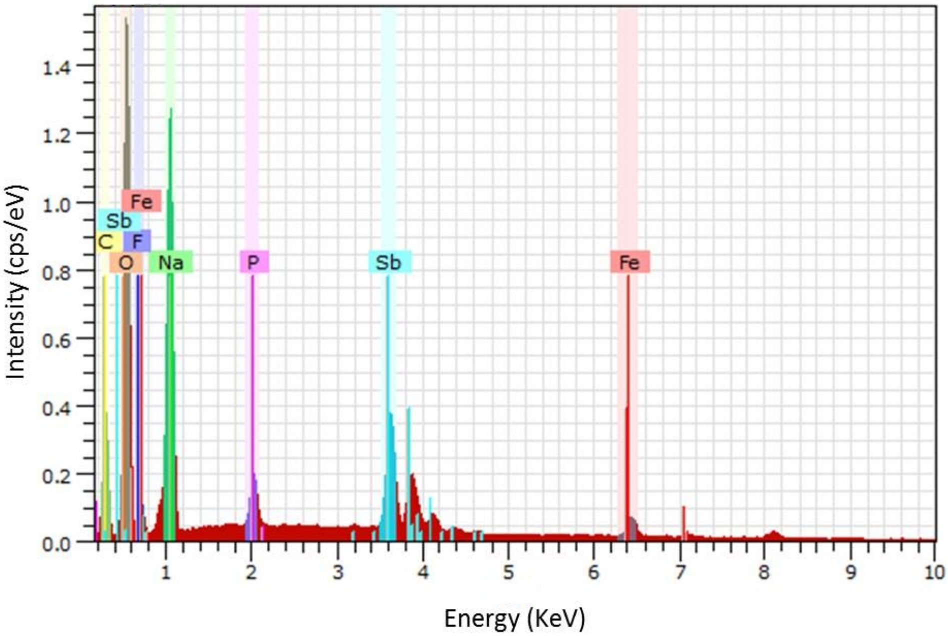

Figure 4.28: EDX spectrum of the $FeSb_2$ anode after used

Element	Atomic Concentration [%]	Error [%]
Oxygen	43.38	3.3
Sodium	25.27	1.1
Carbon	24.51	2.0
Antimony	3.10	0.4
Iron	2.25	0.1
Phosphorus	1.49	0.1

Table 4.8: Elemental composition of the $FeSb_2$ anode after used

4.4.2 *In Situ Operando* SAXS and WAXS with Our *In-House* Built Cell ($FeSb_2$)

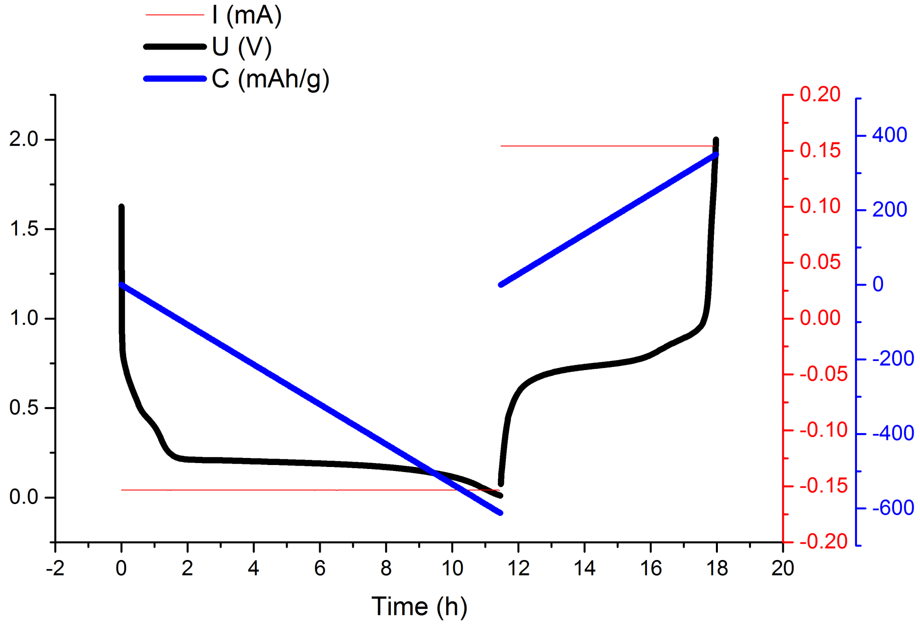

Figure 4.29: Galvanometric characterization of the *in-house* built cell with the anode made of $FeSb_2$

The galvanometric characterization on the cell with $FeSb_2$ was performed at $\frac{C}{10}$ applying $154\mu A$. Figure 4.29 shows the that the sodiation required 11 h 45 min, reaching a specific capacity of $612\frac{mAh}{g}$, while the de-sodiation required 6h reaching a specific reversible capacity of $350\frac{mAh}{g}$. The galvanometric data are consistent with the literature [17].

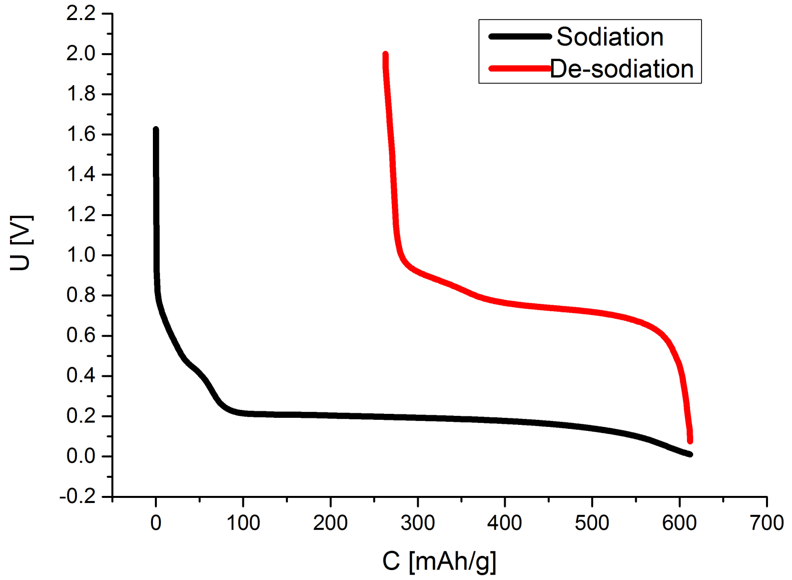

Figure 4.30: Galvanometric cycle potential *vs.* capacity of the *in-house* built cell with the $FeSb_2$ anode

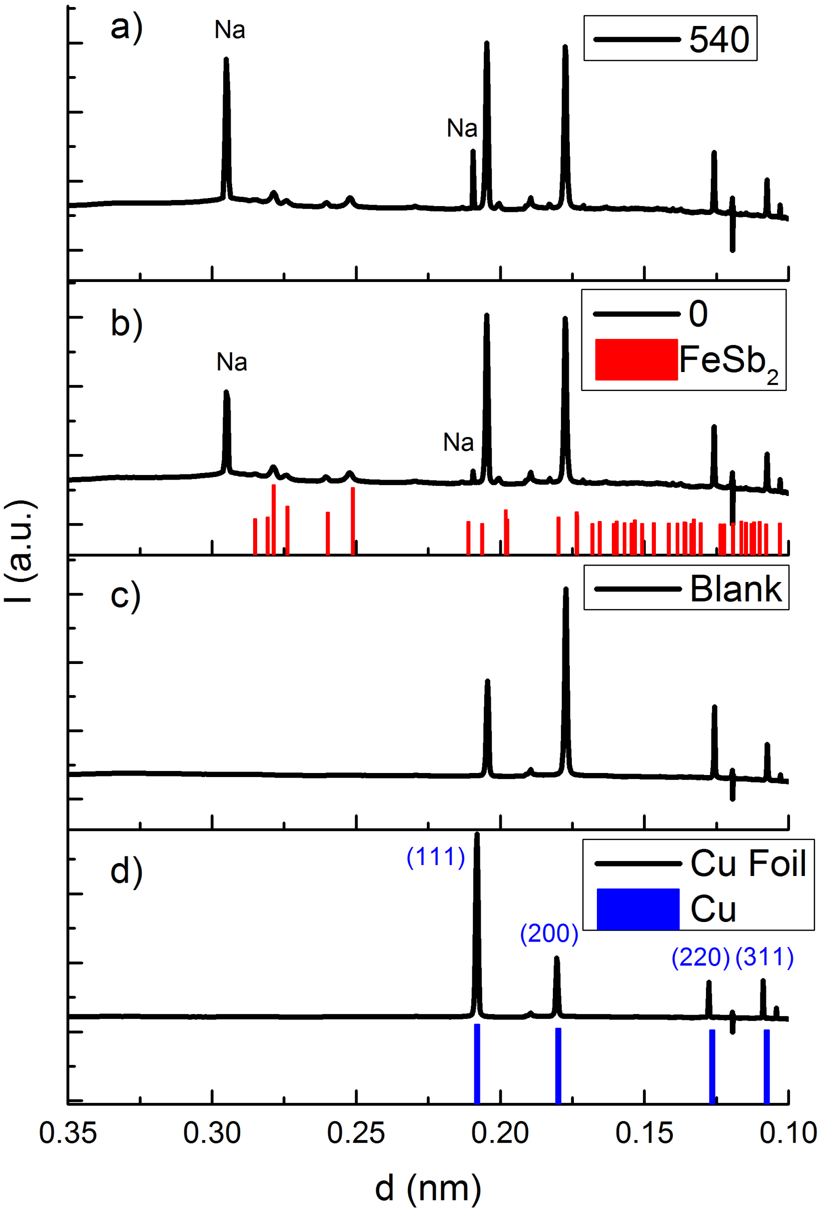

Figure 4.31: WAXS profiles of the $FeSb_2$ of a) No. 540, b) No. 0, c) blank and d) a copper foil, and standard references of Cu [51] and $FeSb_2$ [29]

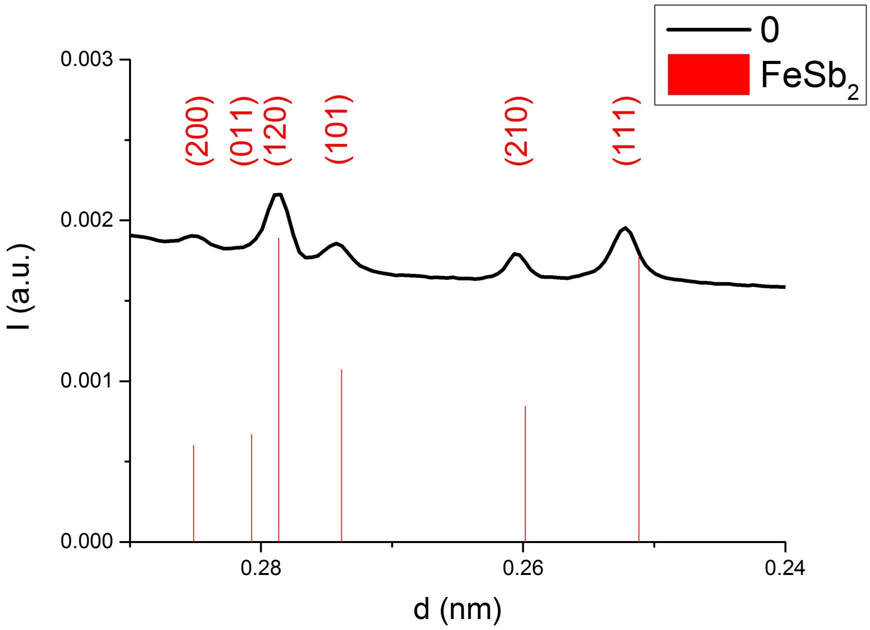

Figure 4.32: Detail of the WAXS measurement No. 0 showing the $FeSb_2$ [29] phase identification

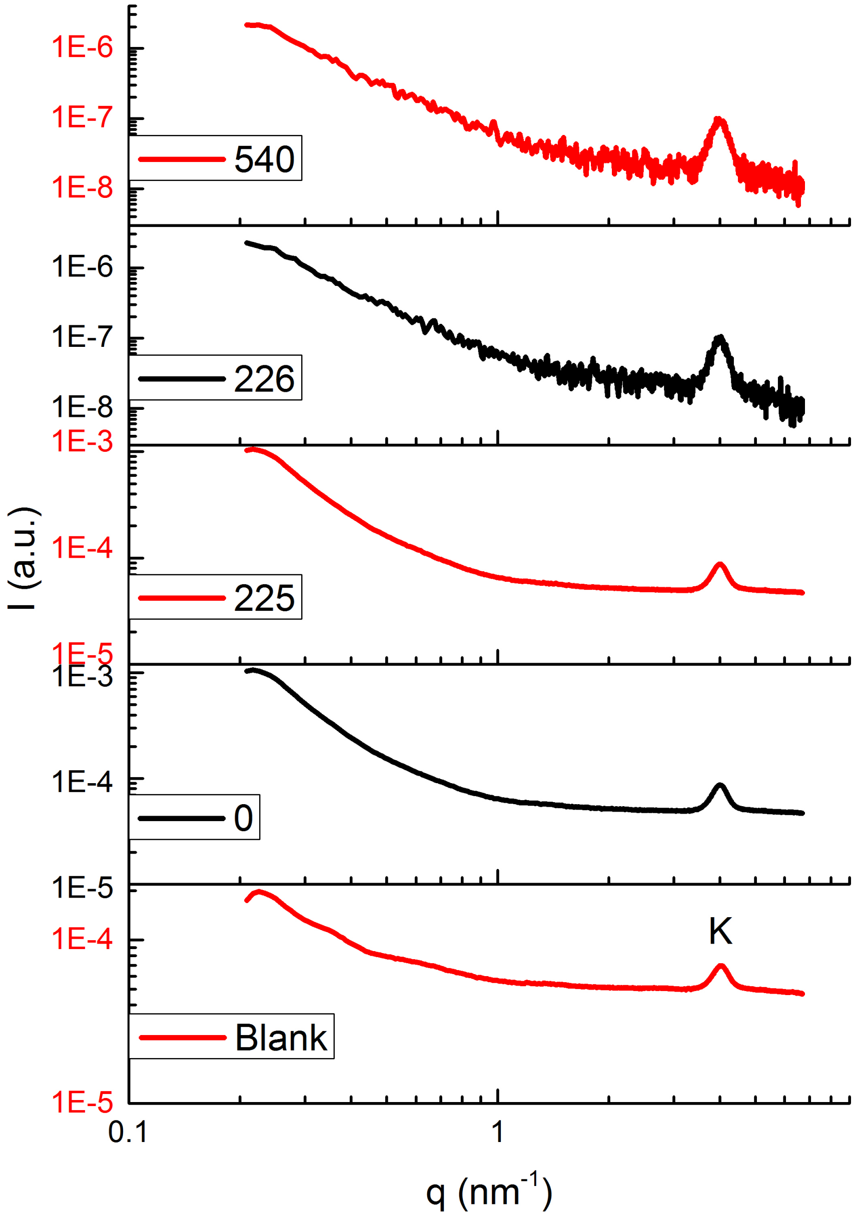

Figure 4.33: SAXS characterization of the *in-house* built cell with the $FeSb_2$ anode. The peak marked K is assigned to the kapton windows of the cell.

The WAXS measurement performed on a clean copper foil (similar to the one used as substrate for the anode preparation), on the blank cell and on the *in-house* cell (Figure 4.31). As can be seen from the figure the initial diffraction pattern profile of the *in-house* cell shows the peaks of the orthorhombic $FeSb_2$ (the indexing is reported in Figure 4.32) and of the metal substrate of the anode. However, the WAXS profile remained unchanged during the cycle. Noteworthly, the first (No. 0) and the last (No. 540) measurement can be fully overlapped, suggesting that during the sodiation/de-sodiation cycle the part of the anode irradiated by the X-ray did not participate to the electrochemical reaction.

Figure 4.33 shows the SAXS profiles of the anode. The first measurement (No. 0) is different from the blank measurement. Instead all the SAXS measurement from the fist to No. 225 are equal. However, the following measurements where affected by a high level of noise due to some unforeseen technical problems on the beamline. For this reason at this stage the measurement where inconclusive and further investigation will be necessary.

Chapter 5

Discussion

The SEM characterization and the elemental mapping profile of as prepared *a-P/C* powder showed that phosphorus and carbon are homogeneously mixed in the clusters with large size distribution. The powder production is easily reproducible and thus the characterization result are similar to the one reported by J. Kim *et al.* [15].

The comparable test between the *in-house* built cell and a standard coin, utilizing the same anode and electrolyte solution, proves that the electrochemical data collected with our new cell are reliable. Furthermore the *in-house* built cell achieved the 90% of the electrochemical performance of a coin cell. Probably the small gap between the too cell is owing to the presence of kapton windows placed on the electron collector components (Figure 3.5 E D). The anode and the cathode are partially in contact with the kapton window and with the metallic components of the electrons collector. This configuration might affect the electron flux. However, the 90% of the performance is promising especially for test on. the materials for large scale storage system because now we are able to use the *in-house* built cell for examination of amorphous materials having high theoretical capacity.

In the last decades several techniques were developed for the *in situ* XRD analysis of the battery materials [13][14]. S. Tepavcevic *et al.* have reported a *in situ non operando* SAXS and WAXS measurements on crystalline bi-layers vanadium oxide for cathode application [18]. This means the X-ray structural characterization of the material was performed after the charge or discharge of the cell. Herein, we have presented for first time, to the best of our knowledge, the simultaneus performance of SAXS, WAXS and galvanometric characterization.

As reported in the first chapter we chose *a-P/C* and $FeSb_3$ anode materials because of the urgent demanded of the development of high capacity anode [1]. In the past the scientific research was mainly focused on the improvement of the cathode and electrolyte performance [1]. Furthermore, *a-P/C* and $FeSb_3$ have the theoretical specific capacity of $2500\frac{mAh}{g}$ and $540\frac{mAh}{g}$, respectively. Those values make them a good candidate for the large scale application in order to store an excess of energy produced by renewable energy sources.

By coordinating time with the characterization result of galvanometric, WAXS and SAXS measurements during the battery cycle on the *a-P/C* anode, we observed the critical moment of the phase transition from amorphous phosphorus to the crystalline Na_3P when the cell was in the potential value of $U = 0.10V$. While the reversible phase transition happened at the potential value of $U = 0.74V$ during the de-sodiation. By applying the Sherrer formula eq.(2.49) we calculated the average crystal size of $25 \pm 0.1nm$. In addition we found out that the first and the last SAXS measurement results are very different except for the overlap of the kapton profile. The appearance of the SAXS peak at $q = 4.7nm^{-1}$ during the sodiation implied the formation of particles with lamellar structure. Furthermore the second peak araised at $q = 1.38nm^{-1}$. By the analysis of the evolution of the SAXS profile in the the Guinire region $(0.16 - 0.4nm^{-1})$ we identified that the aggregation state of the particles in the anode became progressively less compact.

The WAXS data of the *in-house* built cell can be analysed by classical XRD analysis methods such as the phase identification and size calculation by the Sherrer formula eq(2.49), but Rietveld refinement of the Na_3P was not tried out because only two peaks appeared with low intensity. The WAXS profiles of the *in-house* built cell composes all information of crystalline components along the X-ray beam path inside the cell. Since those components are not in the same position the diffraction of each component in the *in-house* built cell is shifted compared with the diffraction of single component. Therefore, we have to calibrate the tabulated peak positions in order to identify them. The sodium cathode and the aluminium foil, used as substrate for anode preparation, behave like a powders with preferential orientation. Thus, the peak intensity of sodium and aluminium change according to the orientation of the metals compare to the incident beam. In fact in the WAXS profile of the blank reported in Figure 4.16 c) we could not see the sodium peak because it was not in Bragg condition.

In the WAXS analysis of the *a-P/C* and $FeSb_2$ the peak intensities of the active materials were weaker than those of aluminium and copper substrates. This means that,choosing an appropriate substrate is important to avoid overlapping peaks position of the interesting material and substrate. Otherwise the metals substrate peaks could completely overlap the active material peaks.

The SAXS characterization of the *a-P/C* has shown that the aggregation state of the anode materials was changed. The cluster become progressively less aggregate. During the sodiation the clusters increase their volume by 300% [15] and become progressively less agglomerate. Interestingly, we have not observed that the system come back to the original agglomerate state having a small volume during the de-sodiation. When clusters lose the contact with the conductive material, they not exchange electrons for the redox reaction any more. Consequently, the electrode lose its original capacity. It is supposed that a lot of clusters remained isolated when the active materials were less agglomerated, causing the reduced of the performance.

During the experimental work we tested two different *a-P/C* anodes. The first anode, prepared by mixing *a-P/C* $70wt\%$, PAA binder $20wt\%$ (know as a carcinogenic material) and carbon superP $10wt\%$, was used for the comparative test between the *in-house* built cell and a coin cell. The second anode, made of *a-P/C* $80wt\%$, CMC $Mw = 250000$ $5wt\%$ binder, CMC $Mw = 700000$ $5wt\%$ binder and carbon superP $10wt\%$, was used for the experiment at the ESRF. The anode composition used at ESRF was not only environmental friendly but also more electrochemically efficient than the other. In fact, the anode used at ESRF reached the reversible capacity of $1753\frac{mAh}{g}$ while the other reached the reversible capacity of $1653\frac{mAh}{g}$.

With the galvanometric measurement of the $FeSb_2$ anode with the *in-house* built cell we obtained a specific capacity of $612\frac{mAh}{g}$ and the reversible specific capacity of $350\frac{mAh}{g}$. The galvanometric curve of the anode was consistent as the literature

[17]. However, we obtained those specific capacity value with a faster galvanometric measurement performed at $\frac{C}{10}$ while L. Baggetto *et al.* [17] reported about measurement performed at $\frac{C}{20}$. We believe that the better performance is owing to the better cell preparetion. In fact L. Baggetto *et al.* reported that the $FeSb_2$ was produced by solid state reaction in Ar/H_2 mixture gas at $700°C$. After the resulting product was ball milled and annealed, the active material was mixed with PVdF polimer binder, diluted in 1-methyl-2-pyrrolidone, and carbon superP. The active material, the binder and the conductive material were mixed in weight percentage of 75%, 10% and 15%. The slurry was cast onto the aluminium or copper foil with a blade and dried under vacuum at $90°C$ overnight. The $FeSb_2$ anode, we tested, was made by a solid state reaction in vacuum. The slurry was prepared by diluting in water a mixture of active material $70wt\%$, of CMC binder $12wt\%$ and of carbon superP $18wt\%$. The slurry was ball mill for $1h$ and then spread on a copper foil, dried before at room temperature for $12h$ and than for $2h$ at $100°C$.

Unfortunately, for technical problem we could not follow the evolution of the SAXS and WAXS profile during the electrochemical reaction. The SAXS and WAXS profile remained unchanged. We believe that the reaction did not happen in the area irradiated by the synchrotron X-ray beam, because the drilled separator layers, used in the *in-house* built cell, adsorbed the electrolyte solution. Thus, the Na^+ ions flux could not interact with the area under analysis.

Chapter 6

Conclusion and Future Work

6.1 Conclusion

Stationary large scale electric storage system is becoming extremely important for the realization of smart grid integration with the renewable energy source. The battery technology development has to follow the rapid progress of the clean energy production market. This thesis is our contribution to the development of future room-temperature rechargeable sodium ion batteries.

The aim of this thesis is to investigate an innovative setup for a new *in-house* built cell for *in situ operando* SAXS, WAXS and galvanometric characterization of the crystalline and amorphous materials for batteries.

The novelty of the experimental work performed in this thesis is the simultaneous acquisition of the electrochemical, SAXS and WAXS characterization of the cell. This work a prodigious progress as compared to the work of S. Tepavcevic *et al.*, because that was an *in situ NON operando* SAXS and WAXS characterization.

The new setup was tested using two anodes: one made of $a\text{-}P/C$ and another made of $FeSb_2$. We produced completely the former while the latter was produced by the group of dr. David Zitoun at Bar Ilan Institute of Nanotechnology and Advanced Materials (BINA).

The comparison among the *in-house* built cell performance, a standard coin cell performance and literature data indicates the reliability of our experimental setup. In addition the result shows that the performance of the *in-house* built cell reached to 90% of the coin cell.

By using the *in-house* built cell it was possible to follow the electrochemical performance of the *a-P/C* completely, obtaining a specific capacity of $2000\frac{mAh}{g}$ and a reversible capacity of $1763\frac{mAh}{g}$. By coordinating the three measurements with time we obtained precise data about the phase transition from amorphous to crystalline and its reversibility, following the evolution of the WAXS peaks. The phase transition from amorphous to crystalline happened at the measure No. 210 when the potential of the cell was $U = 0.10V$. In the contrast the phase transition from crystalline to amorphous occurred at the measurement No. 390 when the potential of the cell was $U = 0.74V$. We calculated an mean crystal size of $25 \pm 0.1nm$ by the Sherrer foruma eq.(2.49) at the end of the sodiation. However, the contribution of SAXS was fundamental to study the partial irreversibility of the cell.

In fact, by SAXS, we observed the formation of an irreversible phase due to the drastic change of the measurement profiles. The first and the last SAXS measurement were completely different except for the kapton profile that remain unchanged. On contrary the first and the last WAXS measurement were fully similar. This dissimilarity between SAXS and WAXS measurements indicates that the first is more sensible than the second to the detection of irreversible process happening during the battery cycle. After 1h 20min from the beginning of the sodiation one peak appeared at $q = 4.7nm^{-1}$. The peak reached the maximum intensity at the end of the sodiation and then its intensity remained stable during the de-sodiation. The precence of this peak suggest the formation of big lamellar structure. Furthermore we detected the formation of a second peak in the SAXS profile at $q = 1.38nm^{-1}$. Noteworthly, we calculated the slopes value of the straight line that approximate the SAXS curve in the Guinier region (q-range $0.16 - 0.4nm^{-1}$) and we observed that the initial slope value was -3.2 and it progressively change to -2.9. A huge variation of the slope value happens during the de-sodiation when the *in-house* built cell was in the range potential $0.6 - 0.74V$, and the slope value oscillates around the value -2.4. Such slope value variation implies that the system becomes progressively less agglomerate during the sodiation because the phosphorus clusters are getting bigger. Although, the phosphorus cluster reduce their volume during the de-sodiation, they do not recover the compactness as the initial state. The huge variation in the aggregations state happen exactly when the crystalline amorphous phase transition arises.

The sodiation/de-sodiation cycle of the *in-house* built cell assembled with the $FeSb_2$ reached a specific capacity of $612\frac{mAh}{g}$ and a reversible specific capacity of $350\frac{mAh}{g}$. The profile of our galvanometric curve was consistent with the result in the literature [17]. Noteworthily we obtained the same specific capacity value performing a faster cycle at $\frac{C}{10}$ whereas L. Baggetto *et al.* performed their experiment at $\frac{C}{20}$ [17]. Therefore, we believe that the $FeSb_2$ anode, we tested, has a better preparation procedure [6] than the one reported by L. Baggetto *et al.*.

The separators, used for the assembly of the two cells, were different. Since the substrate of the $FeSb_2$ was made of copper we drilled the glass fibre layers in order to reduce the material along the X-ray beam path. Because copper absorbs X-ray more than the aluminium does. Probably the glass fibre absorbed most of the electrolyte solution. Therefore in the area of the hole there was not flux of cation Na^+ to induce the reaction. Maybe for this reason we could not observe any change in the crystal structure during the charge/discharge cycle.

In summary, the experimental work of this thesis demonstrated the validity of the *in situ operando* characterization of materials for sodium ion batteries. The electrochemical data are reliable and the WAXS analysis was performed applying classical XRD methods such us the crystal phase identification and the Sherrer formula. In particular the use of the SAXS was important due to the amorphous characteristic of the chosen anode. Using our new *in-house* built cell we observe the formation of the irreversible phase, and the variation of the aggregation state of the particle in the anode. The *in-house* built cell is a promising tool for the electrochemical and X-ray structural characterization of battery materials.

We respond to the demand of the high-capacity anode development. The two anodes materials are good candidates for the large scale storage application due to their good electrochemical performance and also because they are cheap and easy to produce.

6.2 Future Work

In the second chapter we have written about some examples (Figure 2.23) of theoretical and ideal limit cases of SAXS profiles. However, during the experimental work we obtained a profile similar to the curve reported in Figure 2.25. Therefore, a possible future work could be the realization of a theoretical and mathematical model for better data interpretation. We suggest that the realization of the theoretical model should be proved by *ex situ* X-ray Photoemission Spectroscopy (XPS) characterization of the used anode. Because, by the XPS measurement, we are able to understand the nature of the chemical bondings between the different elements detected by the SEM elemental mapping apparatus. Once the theoretical model is developed, further *ex situ* analysis will not be required for the elemental identification.

The *in house* built cell can be used for the analysis of other amorphous materials such as amorphous iron oxide [8], $FePO_4$ [9] and TiO_2 [10] for NIBs application.

We have used the *in house* built cell as an half cell for anode material analyses. However, for the future we want to study both cathode and anode. We belive that, after several experiment, it will be possible assembly a full cell where both cathode and anode are active materials.

Appendix A

Mathematical Background

A.1 Vector Notation

The symbol of vector is represented using the bold letter, while the module is represented by normal letter.

A.2 Dirac Delta Function

In 1930 P. Dirac introduced the delta function as part of his notation. The function is a generalized distribution whose value is zero everywhere except in specific point where it is infinite. Using the notation introduce in the section 2.5.1 for element of crystallography, in three dimensions the delta function can be represented as an infinite line placed in $\mathbf{r}_0$.

$$\delta(\mathbf{r}-\mathbf{r}_0) = \begin{cases} 0, & \text{if } \mathbf{r} \neq \mathbf{r}_0 \\ \infty, & \text{if } \mathbf{r} = \mathbf{r}_0 \end{cases} \tag{A.1}$$

S is the space where the vector $\mathbf{r}$ is defined, the integral of the Dirac delta function is

$$\int_S \delta(\mathbf{r} - \mathbf{r}_0) \mathrm{d}\mathbf{r} = 1 \tag{A.2}$$

A three dimensional Dirac delta function can be rewritten as product of three one dimensional delta function

$$\delta(\mathbf{r} - \mathbf{r}_0) = \delta(x - x_0)\delta(y - y_0)\delta(z - z_0) \tag{A.3}$$

A Gaussian distribution centred in x_0 and FWMH $H \rightarrow 0$ can approximate the Delta function.

$$N(H, x_0) = \frac{1}{H\sqrt{2\pi}} exp(-\frac{(x - x_0)^2}{2H^2}) \tag{A.4}$$

A.3 Fourier Transform

In the section 2.5.2 the structure factor $F_\infty(\mathbf{r}^*)$ was calculated as the Fourier transform of the function $\rho(\mathbf{r})$. The Fourier transform is the frequency domain representation of a function. In the case of the sound signals time dependent the frequency is the inverse of the time and its measure unit is the Hertz. In case of the analysis of the X-ray scattered by a crystals, it is calculated the spatial frequency. In fact the vector $\mathbf{r}$ is defined in the direct space and measured in $\mathring{A}$, instead the vector $\mathbf{r}^*$ is defined in the Fourier transform space and measured in $\mathring{A}^{-1}$. If the eq.(2.40) is the definition of the Fourier transform, the anti Fourier transform is

$$F(\mathbf{r}^*) = \int_{S^*} \rho(\mathbf{r}) exp(-2\pi i \mathbf{r}^* \mathbf{r}) \mathrm{d}\mathbf{r}^* \tag{A.5}$$

The symbol T and T^{-1} are a short way to represent respectively the Fourier transform and its inverse

$$F(\mathbf{r}^*) = T[\rho(\mathbf{r})] \tag{A.6}$$

$$\rho(\mathbf{r}) = T^{-1}[F(\mathbf{r}^*)] \tag{A.7}$$

The Fourier transform and the inverse can be performed consequently on a function with the following results

$$F(\mathbf{r}^*) = TT^{-1}[F(\mathbf{r}^*)] \tag{A.8}$$

$$TT[\rho(\mathbf{r})] = T[F(\mathbf{r}^*)] = \rho(-\mathbf{r}) \tag{A.9}$$

$F(\mathbf{r}^*)$ is a complex number so it can be separated in real part $A(\mathbf{r}^*)$ and the imaginary part $B(\mathbf{r}^*)$

$$F(\mathbf{r}^*) = A(\mathbf{r}^*) + iB(\mathbf{r}^*) \tag{A.10}$$

$$A(\mathbf{r}^*) = \int_S \rho(\mathbf{r}) \cos(2\pi \mathbf{r}^* \mathbf{r}) \mathrm{d}\mathbf{r} \tag{A.11}$$

$$B(\mathbf{r}^*) = \int_S \rho(\mathbf{r}) \sin(2\pi \mathbf{r}^* \mathbf{r}) \mathrm{d}\mathbf{r} \tag{A.12}$$

A.4 Convolution of Functions

The convolution of two functions $\rho(\mathbf{r})$ and $g(\mathbf{r})$ is a mathematical operation that gives the overlap between the two functions. The result of the calculation is a third function defined by the integral

$$C(\mathbf{u}) = \rho(\mathbf{r}) * g(\mathbf{r}) = \int_S \rho(\mathbf{r}) g(\mathbf{u} - \mathbf{r}) \mathrm{d}\mathbf{r} \tag{A.13}$$

where the asterisk is the symbol of convolution between the two function, $\mathbf{u}$ is an of set vector. S is the integration space where $\mathbf{u}$ and $\mathbf{r}$ are defined. The convolution has the following property

$$\rho(\mathbf{r}) * g(\mathbf{r}) = g(\mathbf{r}) * \rho(\mathbf{r}) \tag{A.14}$$

The convolution between a function $\rho(\mathbf{r})$ and a Dirac delta function translate and centred the first in the r_0

$$\delta(\mathbf{r} - \mathbf{r}_0) * \rho(\mathbf{r}) = \rho(\mathbf{u} - \mathbf{r}_0) \tag{A.15}$$

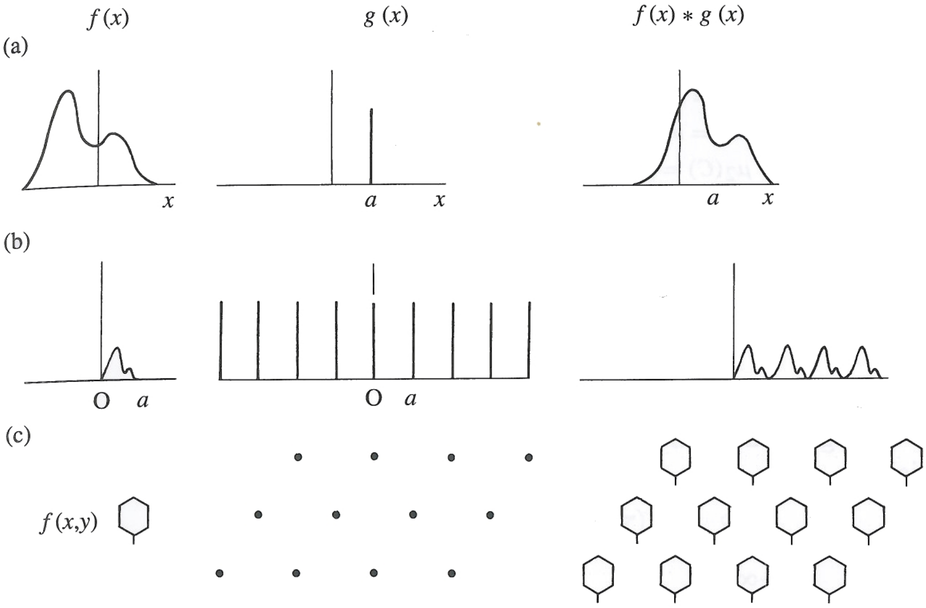

Figure A.1: Convolution of the function f with: a) the Dirac $\delta(x-a)$ delta function; b) a one-dimensional lattice. In c) the convolution of the function $f(x, y)$ with a two-dimensional lattice is shown [39].

Appendix B

List of Symbols

$\mathbf{a}$, $\mathbf{b}$, $\mathbf{c}$: *Lattice vectors*
$\mathbf{a}^*$, $\mathbf{b}^*$, $\mathbf{c}^*$: *Reciprocal lattice vectors*
c : *Speed of light*
C : *Capacity*
C_A : *Anode capacity*
C_B : *Battery Capacity*
C_C : *Cathode*
C_L : *Capacity lost*
d_{hkl} : *Interplanar distance*
e : *Electron charge*
E : *Energy of the electron*
f : *Diffusion factor*
F : *Faraday constant*
$F_\infty(\mathbf{r}^*)$: *Structure factor*
$F_M(\mathbf{r}^*)$: *Structure factor of elementarycell*
$F(\mathbf{r}^*)$: *Structure factor of a real crystal*
$\Delta_r G^\ominus$: *Standard Gibbs free energy*

H : Full width at half maximum (FWHM)

I : Intensity of current

I_{eTh} : Thomsonscatteredintensity

k : Boltzman constant

K : Reaction equilibrium constant

$L(\mathbf{r})$: Direct lattice function

m : Mass

M : Molar mass

m_e : Electron mass

$P(q)$: Form factor

$\mathbf{q}$: Scattering vector

Q_c : Quantity of electricity

R : Perfect gas constant

R_o : Bending radius of the synchrotron orbit

$\mathbf{r}$: Lattice vector

$\mathbf{r}^*$: Reciprocal lattice vector

$\mathbf{s}_0$: X − ray incident vector

$\mathbf{s}$: X − ray scattered vector

$S(q)$: Structure factor

t : Time

T : Temperature

U : Potential

$U^{\ominus}$: Redox standard potential

α, β, γ : Lattice angles

$\Delta\lambda$: Compton wavelength variation

η_c : Coulomb efficiency

θ_B : Bragg's angle

λ : Wavelength

$\rho(\mathbf{r})$: Electron density function of infinite perfect crystal

$\rho_M(\mathbf{r})$: Electron density function of the elementary cell

τ : *Crystal size domain*

φ : *Angle between incident vector andobservation point*

Φ : *Work function*

Bibliography

[1] H. Pan, Y.S. Hu and L. Chen "Room-temperature Stationary Sodium-ion Batteries for large-scale Electric Energy Storage" Energy & Environmental Science. 8, 2338-2360,(2013)

[2] J. B. Goodenough and K.S. Park "Li-Ion Rechargiable Battery: A Perspective" J. Am. Chem. Soc. 135, 1167-1176 (2013)

[3] J. E. Halls, A. Hawthornthwaite, R. J. Hepworth, N. A. Roberts, K. J. Wright, Y. Zhou, S. J. Haswell, S. K. Haywood, S. M. Kelly, N. S. Lawrencec and J. D. Wadhawan "Empowering the Smart grid: can Redox Batteries be Matched to Renewable Energy Systems for Eergy Storage?" Energy & Environmental Science. ,6, 1026-1041 (2013)

[4] https://www.ngk.co.jp/nas/case_studies/rokkasho/

[5] G. Gershinsky, E. Bar, L. Monconduit and D. Zitoun "Operando electron magnetic measurements of Li-ion batteries" Energy & Environmental Science. 6, 2012-2016 (2014)

[6] C. Villevielle, B. Fraisse, M. Womes, J-C. Jumas, L. Monconduit "A new Ternary Li_4FeSb_2 Structure Formed Upon Discharge of the $FeSb_2/Li$" Journal of Power Source 189, 324-330 (2009)

[7] S. Afyon, F. Krumeich, C. Mensing, A. B. and R. Nesper "New High Ca-

pacity Cathode Materials for Rechargeable Li-ion Batteries: Vanadate-Borate Glasses" Nature 4, Article number:7113

[8] W. Wang, S. Wang, H. Jiao, P. Zhan and S. Jiao "A sodium ion intercalation material: a comparative study of amorphous and crystalline $FePO_4$" Phys.Chem.Chem.Phys. 17, 4551-4557(2015)

[9] H. Xiong, M. D. Slater, M. Balasubramanian, C. S. Johnson and T. Rajh " Amorphous TiO_2 Nanotube Anode for Rechargeable Sodium Ion Batteries" J.Phys.Chem.Lett. 2, 2560–2565 (2011)

[10] B. Koo, H. Xiong, M. D. Slater, V. B. Prakapenka, M. Balasubramanian, P. Podsiadlo, C. S. Johnson, T. Rajh and E. V. Shevchenko "Hollow Iron Oxide Nanoparticles for Application in Lithium Ion Batteries" Nano Lett. 12, 2429–2435 (2012)

[11] Y. Liu, Y. Xu, X. Han, C. Pellegrinelli, Y. Zhu, H. Zhu, J. Wan, A. C. Chung, O. Vaaland, C. Wang and L. Hu " Porous Amorphous $FePO_4$ Nanoparticles Connected by Single-Wall Carbon Nanotubes for Sodium Ion Battery Cathodes" Nano Lett. 12, 5664-5668 (2012)

[12] L. Wang, X. He, J. Li, W. Sun, J. Gao, J. Guo, and C. Jiang. Nano-Structured Phosphorus Composite as High-Capacity Anode Materials for Lithium Batteries. Angew. Chem. 2012, 124, 9168

[13] M. Balasubramanian, X. Sun, X.Q Yang, J. McBreen "In situ X-ray diffraction and X-ray absorption studies of high-rate lithium-ion batteries" Journal of Power Sources 92, 1–8 (2001)

[14] I. A. Courtney and J. R. Dahn "Electrochemical and In Situ X-Ray Diffraction Studies of the Reaction of Lithium with Tin Oxide Composites" J. Electrochem. Soc.144, 2045-2052 (1997)

[15] Y. Kim, Y. Park, A. Choi, N. S. Choi, J. Kim. J. Lee, J. H. Ryu S. M. Oh and K. T. Lee "An Amorphous Red Phosphorus/Carbon Composite as a

Promising Anode Material for Sodium Ion Batteries" Advanced Materials, 22, 1521-4095,(2013)

[16] J. Qian, X. Wu, Y. Cao, X. Ai and H. Yang " High Capacity and Rate Capability of Amorphous Phosphorus for Sodium Ion Batteries" Angew. Chem. 52, 4633-4636 (2013)

[17] L. Baggetto, H.Y. Han, C. E. Johnson, C. A. Bridges, J. A. Johnson and G. M. Veith " The Reaction Mechanism of $FeSb_2$ as Anode for Sodium-Ion Batteries" Phys. Chem. Chem Phys. 16, 9538-9545 (2014)

[18] S. Tepavcevic, H. Xiong, V. R. Stamenkovic, X. Zuo, M. Balasubramanian, V. B. Prakapenka, C. S. Johnson, T. Rajhd "Nanostructured Bilayered Vanadium Oxide Electrodes for Rechargeable". ACS NANO, 2012, 6, 530

[19] K. Kordesch and W. Taucher-Mautner "Histrory | Priamry Battery" Enciclopedia of Electrochemical Power Sources 555-564 (2009)

[20] K. E. Aifantis, S. A. Hackney and R. V. Kumar "High Energy Density Lithium Batteries" Wiley Chapter 1 (2010)

[21] D.F. Shriver and P. W. Atkins "Inorganic Chemistry" Oxford University Press Chapter 6 (2002)

[22] P. Silvestroni "Fondamenti di Chimica" Libreria Eredi Virgilio Veschi. Chapter 14

[23] S.-I. Pyun et al., Electrochemistry of Insertion Materials for Hydrogen and Lithium, Monographs in Electrochemistry" Springer Chapter 1 (2012)

[24] J. Jang, Y. Kim, O. B. Chae, T. Yoon, S.M. Kim, H. S Kim, H. Park, J. H. Ryu and S. M. Oh "A First-Cycle Coulombic Efficiency Higher than 100% Observed for a Li_2MO_3 (M = Mo or Ru) Electrode" Angew. Chem. Int. Ed. 53, 10654–10657 (2014)

[25] V. S. Bagotsky "Fundamantals of Electrochemistry" Wiley Chapter 19 (2006)

[26] P. G. Bruce, B. Scrosati and J. Tarascon "Nanomaterilas for Rechargeable Lithium Batteries" Angew. Chem. Int. Ed. 47, 2939-2946 (2008)

[27] Y. Dong and F. J. DiSalvo "Reinvestigation of Na_3P based on Single-Crystal data" Acta Cryst, E61 i223-i224 (2005)

[28] G. Brauer and E. Zintl "Konstitution von Phosphiden, Arseniden, Antimoniden und Wismutiden des Lithiums, Natriums und Kaliums" Zeitschrift fur Physikalische Chemie B37 323-352 (1937).

[29] H. Holseth and A. Kjekshus "Compounds with the marcasite type crystal structure IV. The crystal structure of $FeSb_2$" Acta Chemica Scandinavica 23, 3043-3050 (1969)

[30] M. Wakihara and O. Yamamoto "Lithium Ion Batteries: Fundamentals and Performance" Wiley Chapter 5 (2008)

[31] H. Gabrisch, R. Yazami and B. Fultz "Hexagonal to Cubic Spinel Transformation in Lithiated Cobalt Oxide" Journal of The Electrochemical Society, 6, A891-A897 (2004)

[32] M.M. Thackeray, J.T. Vaughey, C.S. Johnson, A.J. Kropf, R. Benedek, L.M.L. Fransson, K. Edstrom "Structural considerations of intermetallic electrodes for lithium batteries" Journal of Power Sources 113 124–130 (2003)

[33] D. Wu, X. Li, B. Xu, N. Twu, L. Liu and G. Ceder "$NaTiO_2$: a layered anode material for sodium-ion batteries" Energy Environ. Sci. 8, 195-202 (2015)

[34] M. Gu, A. Kushima, Y. Shao, J. G. Zhang, J. Liu, N. D. Browning, J. Li and C. Wang "Probing the Failure Mechanism of SnO_2 Nanowires for Sodium-Ion Batteries" Nano Letters. 13, 5203-5211 (2013)

[35] A. K. Mondal, D. Su, S. Chen, X. Xie, and G. Wang. "Highly Porous $NiCo_2O_4$ Nanoflakes and Nanobelts as Anode Materials for Lithium-Ion Batteries with Excellent Rate Capability" ACS Appl. Mater. Interfaces, 6, 14827-14835 (2014)

[36] P. R. Kumar, Y. H. Jung, K. K. Bharathi, C. H. Lim, D. K. Kim. "High capacity and low cost spinel Fe_3O_4 for the Na-ion battery negative electrode materials". Electrochimica Acta, 146, 503-510 (2014)

[37] C.Giacovazzo, H. L. Monaco, G. Artioli, D. Viterbo, M. Milanesio, G. Ferraris, G Gilli, P. Gilli, G. Zanotti, M. Catti "Fundamentals of Crystallography" Oxford University Press (2011) Chapter 5

[38] http://www.esrf.eu/about/synchrotron-science/synchrotron

[39] C.Giacovazzo, H. L. Monaco, G. Artioli, D. Viterbo, M. Milanesio, G. Ferraris, G Gilli, P. Gilli, G. Zanotti, M. Catti "Fundamentals of Crystallography" Oxford University Press (2011) Chapter 3

[40] H. Schnablegger and Y. Singh "The SAXS Guide Getting Acquainted with the Principles" Anton Paar (2011)

[41] C.Giacovazzo, H. L. Monaco, G. Artioli, D. Viterbo, M. Milanesio, G. Ferraris, G Gilli, P. Gilli, G. Zanotti, M. Catti "Fundamentals of Crystallography" Oxford University Press (2011) Chapter 1

[42] V. K. Pecharsky and P. Y. Zavalij " Fundamentals of Powder Diffraction and Structural Characterization of Materials" Springer Chapter 1 (2005)

[43] A. R. West "Solid State Chemistry and its Application" Wiley Chapter 5 (1985)

[44] R. T. Downs and M. Hall-Wallace "The American Mineralogist crystal structure database" American Mineralogist, 88, 247–250 (2003)

[45] C. Lamberti and G. Agostini "Characterization of Semiconductor Heterostructures and Nanostructures" Elsevier Chapter 5 (2013)

[46] S. Sartori and K.D. Knudsen "Small Angle Neutron Scattering for Hydrides" Book Chapter, Springer “Nuclear Characterisation Techniques for the Investigation of Hydrogen in Materials”, in press.

[47] D. Brandon and W. D. Kaplan "Microstructural Characterization of Materials" Wily Chapter 5 (2008)

[48] D. Williams and C. Barry Carter "Transmission Electron Microscopy" Springer Chapter 35 (2009)

[49] Ch. Broennimann et al. The PILATUS 1M detector. Journal of Synchrotron Radiation **13** 120–130 (2006)

[50] R. W. G. Wyckoff "Crystal Structure" Interscience Publishers, 1 (1963)

[51] I. K. Suh, H. Ohta and Y. Waseda "High-temperature thermal expansion of six metallic elements measured by dilatation method and X-ray diffraction" Journal of Materials Science 23, 757-760 (1988)